RICE UNIVERSITY

Instabilities in a Crystal Growth Melt Subjected to Alternating Magnetic Fields

by

Kenneth E. Davis

A Thesis Submitted
in Partial Fulfillment of the
Requirements for the Degree

Doctor of Philosophy

Approved, Thesis Committee:

Brent C. Houchens, Chair
Assistant Professor of Mechanical
Engineering and Materials Science

John E. Akin
Professor of Mechanical Engineering and
Materials Science

Timothy C. Warburton
Associate Professor of Computational and
Applied Mathematics

Houston, Texas

April, 2013

ABSTRACT

Instabilities in a Crystal Growth Melt Subjected to Alternating Magnetic Fields

by

Kenneth E. Davis

In confined bulk crystal growth techniques such as the traveling heater method, base materials in an ampoule are melted and resolidified as a single crystal. During this process, flow control is desired so that the resulting alloy semiconductors are uniform in composition and have minimal defects. Such control allows for tuned lattice parameters and bandgap energy, properties necessary to produce custom materials for specific electro-optical applications. For ternary alloys, bulk crystal growth methods suffer from slow diffusion rates between elements, severely limiting growth rates and reducing uniformity. Exposing the electrically conducting melt to an external alternating magnetic field can accelerate the mixing. A rotating magnetic field (RMF) can be used to stir the melt in the azimuthal direction, which reduces temperature variations and controls the shape at the solidification front. A traveling magnetic field (TMF) imposes large body forces in the radial and axial directions, which helps reduce the settling of denser components and return them to the growth front. In either case, mixing is desired, but turbulence is not. At large magnetic Taylor numbers the flow becomes unstable to first laminar and then turbulent transitions. It is imperative that crystal growers know when these transitions will occur and how the flow physics is affected. Here, the melt driven by electromagnetic forces is analyzed through the use of 3D numerical simulations of the flow field up to and beyond the

point of laminar instability. The analysis aims to emulate laboratory conditions for generating electromagnetic forces for both types of alternating magnetic fields and highlights the differences between laboratory forces and the analytical approximations that are often assumed. Comparisons are made between the resulting forces, flow fields, and points of instability as the frequency of the alternating field varies. Critical Taylor numbers and the resulting unstable flow fields are compared to the results from linear stability theory.

Acknowledgments

I would like to express my sincere gratitude to my advisor and thesis committee chair, Dr. Brent C. Houchens, for his guidance in this work and his many suggestions that improved the quality of this work. I would also like to thank Dr. Ed Akin and Dr. Timothy Warburton for serving on my thesis defense committee.

I am grateful to Yue (Jacky) Huang for his assistance with the numerical analyses and for the many discussions that have aided the research process, and Jennifer Small for contributing to much of the numerical analysis found within this thesis.

This work was supported by the National Science Foundation.

Contents

Illustrations

Tables

Chapter 1

Introduction

Semiconductor crystals are ubiquitous in the world of modern technology, but mostly go unnoticed. They are essential components in many areas including electronics, electrooptics, magnetic devices, optics, oscillators, polarizers, transducers, radiation detectors, lasers, and more. For the crystal to be useful for these technological applications, it must have high quality, purity, and low density of defects.

Crystal growth is the process by which the microscopic structure of a material is altered such that it has an orderly arrangement in all directions. This gives the material unique physical and chemical properties targeted by crystal growers for specific applications. Crystals are prone to imperfections such as dislocations, a localized irregularity in structure, which the crystal grower attempts to eliminate by controlling the growth through various methods.

Crystal growth methods are most generally categorized by the phase transition involved. There are solid-solid, liquid-solid, and gas-solid transitions, with the latter two being most common. The particular liquid-solid transition known as crystal growth from a melt is of primary interest in this work. Crystals grown from a melt account for half of all technological crystals currently in use because of how quickly they can be produced [3]. One particular method is known as the Traveling Heater Method and it is the method of primary concern throughout this work.

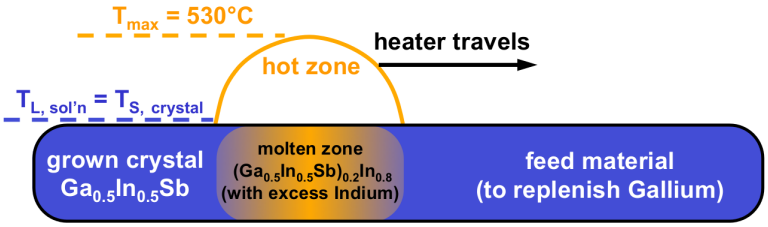

Figure 1.1 : Schematic diagram of a horizontal traveling heater method to grow a GaInSb crystal with excess In as a solvent [1].

1.1 Traveling Heater Method

The Traveling Heater Method (THM) is just one of many methods for growing semiconductor crystals. Triboulet [4] has given a detailed review of the THM process. He explains that the THM circumvents the problems seen in other growth methods, which arise from some particular difficulties associated with the phase diagram for a specific composition, required high pressures, or complex implementations. He concluded that the THM allows for lower temperatures, lower pressures, reduced defect levels, and reduced contamination.

The THM can be arranged horizontally or vertically. A diagram of the horizontal THM can be seen in Figure 1.1. In this method, a polycrystalline material is contained within an ampoule and a heater is gradually moved from one end of the ampoule to the other. As the heater travels along the ampoule, it melts a small portion of the material which, with proper control, resolidifies in single-crystalline form once the heater has moved along. The molten region allows for the mixing of elements for binary and ternary materials through convection and diffusion before crystallization and for the replenishment of favorably solidified constituents from the feed material. Here, we consider the growth of a ternary GaInSb crystal, which has the composition $(Ga_{1-x}In_x)_{1-y}Sb_y$. However, the ternary GaInSb behaves as two binaries, GaSb and

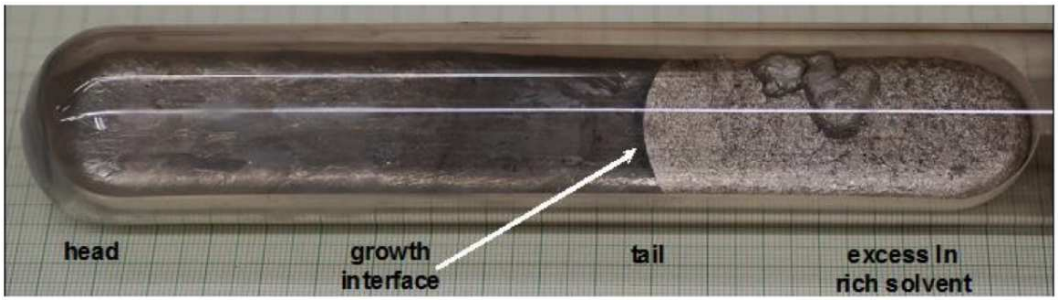

Figure 1.2 : $Ga_{1-x}In_xSb$ crystal grown using the horizontal traveling heater method, inside a boat contained within a quartz ampule [2]; reprinted with permission. The composition of the crystal region is given in Figure 1.4(b).

InSb, which has the form $Ga_{1-x}In_xSb$ where subscript y has been dropped as it is given the value $y = 0.5$ to match experiments carried out at the Hanscom Air Force Base [2]. A photograph of one of the horizontal THM grown crystals is shown in Figure 1.2.

Figure 1.3 shows the pseudo-binary phase diagram for GaSb and InSb when $y = 0.5$. Because GaSb has a higher solidification temperature, the GaSb solidifies while the InSb is rejected back into the melt. This causes the head to be rich in GaSb while the tail is rich in InSb. This is major issue with another growth technique known as the Bridgman method. In this method, the polycrystalline material is contained in an ampoule but the entire charge is melted and allowed to mix before being directionally solidified from one end to the other. The composition for a Bridgman grown GaInSb crystal is shown in Figure 1.4(a). This sample suffers from strong compositional variation along the length of the crystal.

In comparison, the advantage of the THM is that since only a portion of the charge is melted at a given time, the composition of that charge can be altered from one end to the other in an effort to increase uniformity. This can be accomplished by redistributing the indium such that it is initially much richer near the head and

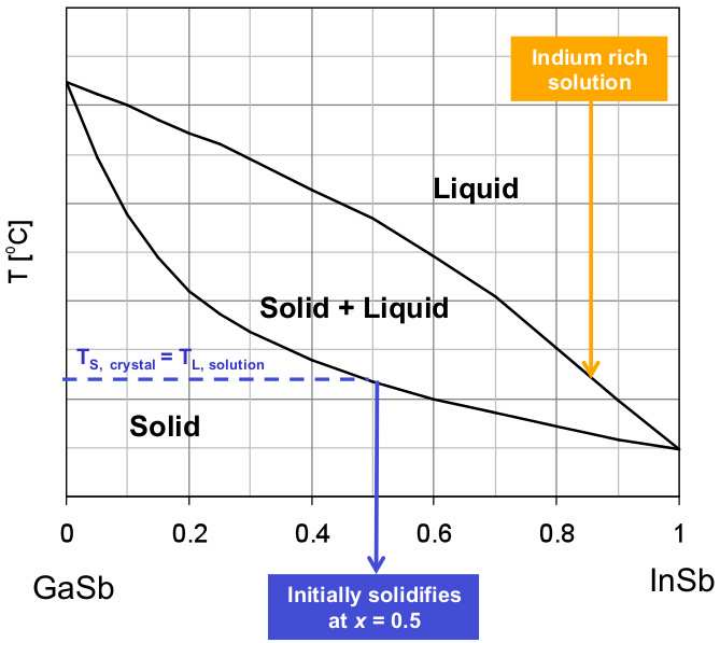

Figure 1.3 : $Ga_{1-x}In_xSb$ phase diagram [1].

drops off toward the tail. Or, as in the ternary alloy grown in Figure 1.2, excess indium can be used as a solvent to shift the intersection with the liquidus line on the phase diagram, subsequently shifting the intersection with the solidus line, as demonstrated in Figure 1.3. The increased amount of indium places the mixture further along the phase diagram, toward the indium-rich regime where the solidus temperatures vary less with composition. This initial indium-rich melt allows for a more favorable mixture at the growth front and works to counteract the preferential solidification of GaSb so that the crystal is close to uniform from head to tail, as shown in Figure 1.4(b). Note that the excess indium remains beyond the tail of the grown crystal, as shown in Figure 1.2.

Figure 1.4 compares the composition of $Ga_{0.5}In_{0.5}Sb$ crystals grown using the horizontal Bridgman method and the horizontal THM. The crystal grown using the Bridg-

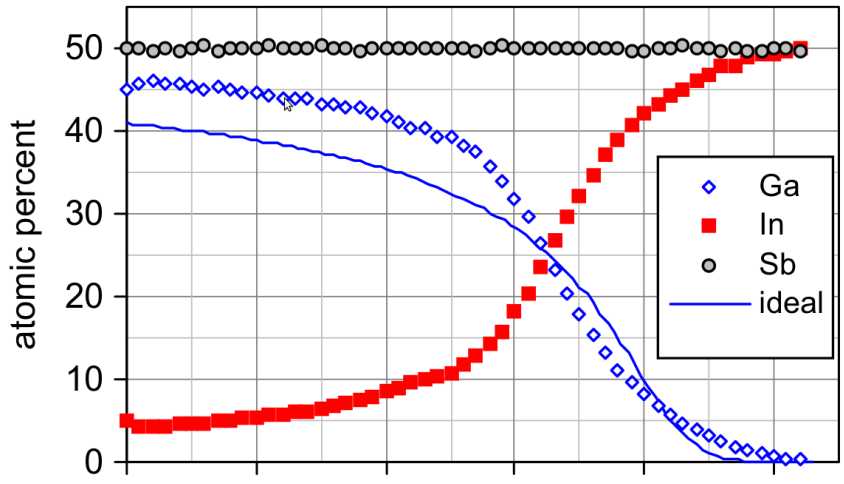

(a)

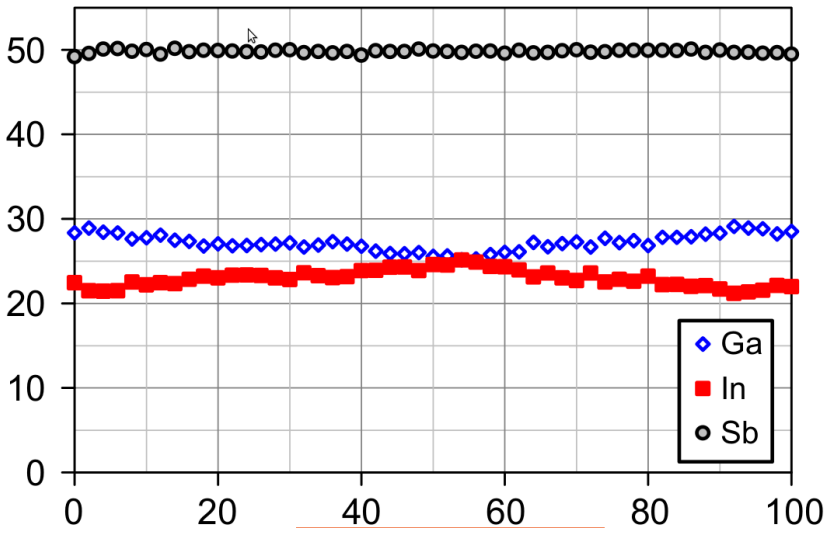

(b)

Figure 1.4 : Electron Microprobe analysis of $Ga_{1-x}In_xSb$ crystals grown by a) horizontal Bridgman at stoichiometric conditions and b) the horizontal traveling heater method with excess indium as a solvent [2]; reprinted with permission.

man method suffers from non-uniformity as expected, with a gallium-rich (indium-depleted) head and a gallium-depleted (indium-rich) tail whereas the crystal grown using the THM has more uniformity throughout.

1.2 Crystal Growth with Magnetic Stirring

The confined crystal growth problem with magnetic stirring is analyzed here numerically through three-dimensional simulations and comparisons to linear stability theory. Numerical investigations for the RMF case have been extensive in the last decade using both linear stability analyses and simulations. Nearly all of these studies use an approximate analytic solution for the applied body force. Numerical solutions of the flow driven by this analytic solution have been compared to the results of the many experimental investigations.

The TMF case has been studied less than the RMF, but significant work has still been done over the last decade through linear stability analyses, numerical simulations, and experiments. As in the case of the RMF, TMF simulations typically use an analytic expression to approximate the forcing term in the momentum equations.

The present work considers the analytic body forces typically used, but also continues the work started by Huang [5] and Huang *et al.* [6] and finds numerical solutions for the electromagnetic fields and subsequent body forces that more reasonably approximate experiments over a wider parameter space. This is an effort to understand the differences between experiment and theory, and demonstrate when the analytic approximation is valid or invalid.

1.2.1 RMF Stirring

The idea of stirring liquid metals during the solidification process using a rotating magnetic field has been around for nearly a century, introduced by Kürth in 1917 [7]. Since then, there have been numerous experimental and numerical studies. Dold and Benz give a thorough discussion of the use of RMF in crystal growth in their 1999 paper [8]. Their discussion demonstrated the usefulness of RMF in several ways. Melts with periodic instabilities, resulting from thermocapillary convection in processes with free surfaces or from buoyant convection, can be suppressed using a RMF. This subsequently reduces dopant inhomogeneities. Instability suppression can also be achieved with steady fields [9] [10], but Dold and Benz point out that an alternating field requires potentially orders of magnitude less power than a steady field. Additionally, applying a RMF has been shown to decrease the concavity in the interface shape at the growth front, which helps to avoid the propagation of stress defects into the crystal. Finally, some solution growth experiments showed a reduction in inclusion densities.

Volz *et al.* experimented with applying a RMF to the Bridgman process for various aspect ratios [11]. They grew single crystals of Ga-doped Ge and analyzed the stability with respect to the aspect ratio and magnetic Taylor number. They found that a value of $Ta_m = 5.0 \times 10^4$ is necessary to reduce the interface deflection by 50%, but that the flow is unstable for $A > 2$. They concluded that it would be difficult to use the RMF to control the interface shape and maintain time-independent melt flow with the Bridgman technique. They instead suggested the THM as a suitable method to achieve a small aspect ratio while maintaining control of the interface shape via RMF.

Senchenkov *et al.* [12] grew ternary CdHgTe in single crystal form using the THM

within a RMF with various magnetic field strengths in microgravity and measured the composition of the resulting crystals by energy dispersive X-ray microanalysis. They found that in addition to creating a less concave interface, the application of a RMF greatly increased the radial homogeneity of the crystal, which leads to more uniform properties.

Ghaddar *et al.* [13] studied the effects of gravity on the effectiveness of the RMF for the THM. They found through numerical simulations that in low gravity environments the RMF is quite effective at controlling the compositional uniformity of the solution at the growth interface with little change to the shape of the interface. However, they also showed that in high gravity environments (such as on the surface of the earth), the RMF increases the convexity of the growth interface, which is desired to a certain degree, but decreases the compositional uniformity at the solidification front. Many have also applied a RMF to floating-zone crystal growth techniques, which are driven by thermocapillary forces at the free surface. Walker *et al.* [14] performed a linear stability analysis for magnetic Taylor numbers less than $Ta_m = 8000$ and found that for $Ta_m > 1000$, the flow became more stable than it is without the RMF. Dold *et al.* [15] performed experiments for much larger Taylor numbers ($9400 < Ta_m < 85,000$) and Reynolds numbers, but were unable to find a stable flow regime, suggesting that the RMF may force the flow to become unstable due to high flow velocities. However, they did find that the RMF reduced the deviation from axisymmetry in the flow. The experiments also found that as the magnetic field strength was increased, there was a dramatic decrease in the difference between the minimum and maximum dopant concentrations in the striations as well as the average distance between adjacent dopant maxima.

The first stability analysis on an electrically conducting cylindrical melt driven by

an RMF was done in 1974, but for an infinitely long cylinder [16]. He found a Taylor-like instability for this case. Gelfgat *et al.* [17] then showed that using a finite cylinder has a stabilizing effect on the flow. Other numerical analyses, like those by Marty *et al.* [18] and Kaiser and Benz [19] for instance, showed that as the aspect ratio is lowered the flow becomes more stable. In 2001, Grants and Gerbeth [20] published a linear stability analysis for flow confined to a cylinder with finite length and driven by a RMF, but restricted the study to axisymmetric flows. They found that the flow becomes linearly unstable at $Ta_m^{cr} = 1.635 \times 10^5$ with an angular frequency of oscillations $\lambda^{cr} = 1659$. This case is also studied here via axisymmetric simulations. Grants and Gerbeth [21] followed the 2001 paper a year later with a paper on fully three-dimensional instabilities for the same problem with aspect ratios between 0.5 and 2.0. The results showed that non-axisymmetric instabilities always occur sooner than the axisymmetric instabilities found previously. They show neutral stability curves for the aforementioned aspect ratios that indicate $m = 1$, $m = 2$, and $m = 3$ instabilities dominate for $A \leq 0.81$, $0.81 < A < 1.53$, and $A > 1.53$, respectively. The $m = 1$ and $m = 2$ instabilities are axially symmetric for the values of A when they are dominant. The dominant $m = 3$ is symmetric except for a small window just after $A = 1.53$ where the antisymmetric mode is dominant. All initial instabilities were oscillatory. In the work presented here, the aspect ratio will be held at unity so the expected instability is oscillatory, symmetric, with $m = 2$.

Koal *et. al* [22] used Semtex [23], the code also used for the present study, to simulate the flow in a confined cylinder with an aspect ratio of unity with the analytic body forces resulting from a rotating magnetic field. Their study found that perturbations to the base flow result in a single subcritical burst, a series of supercritical bursts, or a sustained unsteady regime at higher Taylor numbers ($Ta_m = 1.6 \times 10^5$

in this case). The use of "subcritical" and "supercritical" here correspond to values of the Taylor number that are below and above the critical point from *linear stability theory* rather than one found in three-dimensional simulations. In all cases the instability manifests as Taylor-Görtler vortices.

The present study confirms much of the results of Koal *et al.* using the analytic force, but also adds to it the existence of a flow regime with a supercritical burst followed by nonlinear saturation just beyond the expected point of instability. We also add the results from using a "laboratory" force that is found through numerical simulations that approximate the electromagnetic laboratory set up. The differences between base flows, critical points, and unstable flow regimes using the analytic and laboratory forces are analyzed through the use of 3D fluid flow simulations. Comparisons are also made to linear stability theory, which also uses the analytic body force.

1.2.2 TMF Mixing

One of the benefits to using a TMF is to offset the effects of gravity, which causes denser components to settle to the bottom of the melt. Mazuruk [24] did numerical calculations to test the feasibility of offsetting gravity by the application of an axisymmetric TMF. He found that the TMF does dramatically reduce the buoyant effects for small aspect ratios, but is less effective for large aspect ratios.

Dropka *et al.* [25] studied through numerical simulations the ability to control the growth interface shape with a TMF for several different materials. For all materials used in the study, the desired slightly convex interface shape was achieved for TMFs with the right combination of AC frequency, electric current, and phase shift. Lyubimova *et al.* [26] also found that the interface flattens when growing GaAs crystals via

the Vertical Gradient Freeze (VGF) method. In addition, radial dopant segregation was reduced by the application of the TMF.

Grants and Gerbeth first considered a linear stability analysis of the TMF in their 2004 paper [27]. They assumed an analytic form for the magnetic vector potential from which a magnetic field is found. By letting the wavelength of the traveling wave be much greater than the cylinder radius, making a low frequency approximation, and assuming the electric field term dominates in Ohm's Law, they were able to compute current densities and forces. After time-averaging, only an axial force component remains, which was then used in the Navier-Stokes equations to drive an axisymmetric base flow, which was then studied with linear stability analysis. The stability analysis was performed for aspect ratios $0.5 \leq b \leq 2.0$. For unit aspect ratio a periodic $m = 3$ mode is critical.

The experiments of Ramachandran *et al.* found critical values several times lower than those of Grants and Gerbeth. Discussion of this discrepancy brought up the small wavenumber approximation, experimental uncertainties, and the use of one free surface in the experiments. Later experiments by Lantzsch *et al.* [28] and Galindo *et al.* [29] found good agreement with theory presented by Grants and Gerbeth.

Gelfgat and Kit [30] extended the analysis of Grants and Gerbeth by including the skin effect in their linear stability analysis. Gelfgat followed this with a more thorough presentation of a linear stability analysis that allowed for both the wavenumber and the circular frequency to take on larger values [31]. The same magnetic vector potential was used, but the expressions for the forces were not restricted to the small wavenumber, small AC frequency approximation. The study showed that increases in both the wavenumber and the AC frequency can lead to a sharp drop in the critical value of the magnetic Taylor number for the TMF Ta_{TMF}.

Here, we study the TMF forced flow numerically using the simple forces for both the low wavenumber, low frequency case and for real, time-averaged force fields computed for the laboratory setup. These results are compared to the linear stability analysis and the differences between laboratory forces and analytic forces are investigated.

1.2.3 Combining the RMF and TMF

While we do not consider the superposition of the RMF and TMF in the present work, the discussion of each field separately naturally leads to a curiosity of how applying both affect the fluid flow. Cramer *et al.* [32] conducted experiments using both fields and obtained velocity profiles via a UDV setup for many combinations of the RMF and TMF together in turbulent flows. Their results suggests that the RMF influences dominate the flow field unless the TMF forces exceed the RMF forces by at least one order of magnitude. Stiller and Koal investigated the idea through numerical simulations [33]. Their results also show that the RMF forces dominate when the force fields are of comparable strength. When superimposing the fields with identical frequencies, a fully three-dimensional turbulent flow can appear even for weak fields. The flow has a swirling motion about a twisted axis that extends diagonally from the bottom to the top of the cylinder, which could be useful for mixing. Additionally, Stiller *et al* recently published a summary of the most recent numerical and experimental work for both applied RMFs and TMFs and also for the combination of the two fields [34].

Chapter 2

Model and Governing Equations

The crystal growth melt is confined to an insulating container at its radial boundary and bounded axially by the solid semiconductor crystal and feed rod. The melt takes on the shape of the container and is assumed to be flat at both the melting front and the resolidification front, giving a cylindrical shape. The radius of the cylinder is R^* and the total length is $2bR^*$, where b is the aspect ratio. In this work the aspect ratio will always be $b = 1$. All boundaries of the melt are assumed to be electrically insulating, no-slip and no-penetration boundaries. To investigate only flow driven by alternating fields, the flow is assumed to be isothermal and buoyancy effects are ignored.

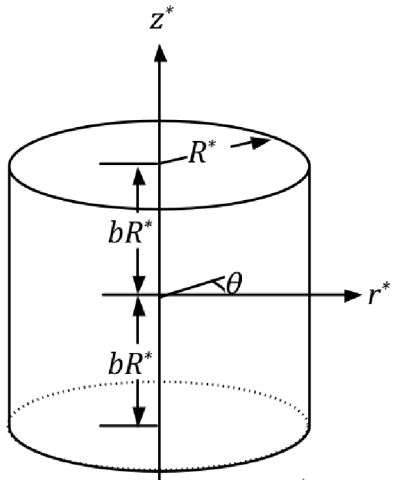

Figure 2.1 : The cylindrical melt domain of the vertical traveling heater method.

The equations of magnetohydrodynamics (MHD) govern the flow in the melt, subjected to an alternating magnetic field. These equations couple Maxwell's electromagnetic equations and charge conservation to the equations of fluid flow, the Navier-Stokes equations for fluid momentum and the mass continuity equation. The following sections explain the governing equations and show how they can be simplified for the case of semiconductor crystal growth at the laboratory scale. The notational convention used throughout is such that dimensional quantities are denoted by the use of an asterisk superscript and dimensionless quantities have no asterisk.

2.1 Electromagnetic Equations

The four equations of electromagnetics (EM) are collectively known as Maxwell's equations. These are Gauss's law, the solenoidal constraint on the magnetic flux density, Faraday's law and Ampère's law, which can be written in differential form, respectively, as

$$\nabla^* \cdot \mathbf{E}^* = \frac{\rho_e^*}{\epsilon_0^*}, \tag{2.1}$$

$$\nabla^* \cdot \mathbf{B}^* = 0, \tag{2.2}$$

$$\nabla^* \times \mathbf{E}^* = -\frac{\partial \mathbf{B}^*}{\partial t^*}, \tag{2.3}$$

$$\nabla^* \times \mathbf{B}^* = \mu_p^* \mathbf{j}^*, \tag{2.4}$$

where $\mathbf{E}^*$ is the electric field, $\mathbf{B}^*$ is the magnetic flux density, ρ_e^* is the electric charge density, $\mathbf{j}^*$ is the electric current density, t^* is time, μ_p^* is the magnetic permeability, and $\epsilon_0^* = 8.85 \times 10^{-12}$ C^2/Nm^2 is the permitivity of free space. Displacement electric currents have been neglected so that Maxwell's correction to Ampère's law does not appear, an appropriate assumption for molten semiconductors.

Gauss's law (Equation 2.1) relates the electric charge ρ_e^* to the electric field $\mathbf{E}^*$

produced and, in its integral form, states that the electric flux through any closed surface is proportional to the enclosed electric charge ρ_e^*. Equation 2.2 simply states that $\mathbf{B}^*$ is solenoidal and, unlike for electric charges, there are no magnetic "charges" and therefore magnetic flux lines either form closed loops or extend to infinity. Faraday's law (Equation 2.3) indicates that temporal variations in magnetic flux density $\mathbf{B}^*$ impact the electric field $\mathbf{E}^*$ and Ampère's law (Equation 2.4) relates the magnetic field $\mathbf{B}^*$ to the electric current density $\mathbf{j}^*$ that produces it.

In addition to Maxwell's equations, Ohm's law

$$\mathbf{j}^* = \sigma^*(\mathbf{E}^* + \mathbf{v}^* \times \mathbf{B}^*) \tag{2.5}$$

states that the electric current density $\mathbf{j}^*$ can be also generated by an electric field $\mathbf{E}^*$ and by flow motion $\mathbf{v}^*$ of a conductor crossing magnetic flux lines $\mathbf{B}^*$. Furthermore, the most general form of conservation of charge requires

$$\nabla^* \cdot \mathbf{j}^* = -\frac{\partial \rho_e^*}{\partial t^*}. \tag{2.6}$$

For non-relativistic flows the charge relaxation time is incredibly short and the non-zero charge density is very small, so the time derivative of the electric charge density is negligible [35] and conservation of charge (Equation 2.6) simplifies to

$$\nabla^* \cdot \mathbf{j}^* = 0. \tag{2.7}$$

In general, the total volumetric force is given by the combination of the electrostatic and Lorentz forces

$$\mathbf{F}_{\mathrm{EM}}^* = \rho_e^* \mathbf{E}^* + \mathbf{j}^* \times \mathbf{B}^*, \tag{2.8}$$

with the latter generated whenever electric current density $\mathbf{j}^*$ crosses magnetic flux lines. However, for non-relativistic flows, the electrostatic component is again negli-

gible compared to the Lorentz force [35] and the total volumetric body force (Equation 2.8) simplifies to just the Lorentz contribution

$$\mathbf{F}^*_{\mathrm{EM}} = \mathbf{j}^* \times \mathbf{B}^*. \tag{2.9}$$

Since ρ_e^* no longer appears in the problem of interest, Gauss's law need not be solved.

Equations 2.2 – 2.4 plus the simplified version of conservation of charge (Equation 2.7) govern the EM problem and, in general, couple to the fluid flow problem through Ohm's law (Equation 2.5) and contribute $\mathbf{F}^*_{\mathrm{EM}}$ via the simplified Lorentz force (Equation 2.9) to the momentum equations.

The electrical conductivity of the solidified crystal and feed rod is typically 2 to 3 orders of magnitude smaller than that of the melt. Thus, electrically insulating boundary conditions are applied on the top and bottom boundaries. The ampoule is typically quartz, which is also electrically insulating. For the crystal growth applications of interest here, the magnetic permeability μ_p^* and electrical conductivity σ^* will be assumed to be constant throughout the melt.

2.2 Flow Field Equations

The flow in the melt is governed by the incompressible, constant density continuity equation

$$\nabla^* \cdot \mathbf{v}^* = 0 \tag{2.10}$$

with velocity field $\mathbf{v}^*$, which guarantees conservation of mass. Momentum is conserved via the constant property Navier-Stokes equations

$$\rho^* \frac{\partial \mathbf{v}^*}{\partial t^*} + \rho^* (\mathbf{v}^* \cdot \nabla^*) \mathbf{v}^* = -\nabla^* P^* + \mu^* \nabla^{*2} \mathbf{v}^* + \mathbf{F}^* \tag{2.11}$$

with density ρ^*, viscosity μ^*, pressure P^* and generalized volumetric body force $\mathbf{F}^*$. The melting and solidification fronts are treated as no-slip, no-penetration boundaries,

as is the ampoule wall.

2.3 Nondimensionalization of Maxwell's Equations

Significant simplifications can be made to Maxwell's equations for constant density, incompressible magnetohydrodynamics at typical laboratory scales. The results of this manipulation and scaling include the derivation of a transport equation for $\mathbf{B}^*$, and partial (one-way) decoupling of the electromagnetic equations from the hydrodynamic equations.

2.3.1 Transport Equation for $\mathbf{B}^*$

Using a subset of Equations 2.2 – 2.10, a transport equation for $\mathbf{B}^*$ in the melt can be derived. First, Ohm's law (Equation 2.5) is used to eliminate the electric current density in Ampère's law (Equation 2.4). Then, taking the curl of the resulting equation with σ^* and μ_p^* constant gives

$$\nabla^* \times (\nabla^* \times \frac{\mathbf{B}^*}{\mu_p^*}) = \sigma^* \nabla^* \times (\mathbf{E}^* + \mathbf{v}^* \times \mathbf{B}^*). \tag{2.12}$$

Using cross-product vector identities to expand Equation 2.12 and using Faraday's law (Equation 2.3) to replace $\nabla^* \times \mathbf{E}^*$ gives

$$\nabla^* \underbrace{(\nabla^* \cdot \frac{\mathbf{B}^*}{\mu_p^*})}_{\substack{=0 \\ \text{Equation 2.2}}} - \nabla^{*2} \frac{\mathbf{B}^*}{\mu_p^*} = \sigma^* \underbrace{(\nabla^* \times \mathbf{E}^*)}_{\substack{=-\partial \mathbf{B}^*/\partial t^* \\ \text{Faraday's law} \\ \text{Equation 2.3}}} +$$
$$+\sigma^* [(\mathbf{B}^* \cdot \nabla^*)\mathbf{v}^* - (\mathbf{v}^* \cdot \nabla^*)\mathbf{B}^* + \mathbf{v}^* \underbrace{(\nabla^* \cdot \mathbf{B}^*)}_{\substack{=0 \\ \text{Equation 2.2}}} - \mathbf{B}^* \underbrace{(\nabla^* \cdot \mathbf{v}^*)}_{\substack{=0 \\ \text{continuity} \\ \text{Equation 2.10}}}]. \tag{2.13}$$

Rearranging the remaining terms yields the *transport equation for* $\mathbf{B}^*$

$$\underbrace{\frac{\partial \mathbf{B}^*}{\partial t^*}}_{\substack{\text{variation} \\ \text{in time}}} + \underbrace{(\mathbf{v}^* \cdot \nabla^*)\mathbf{B}^*}_{\text{advection}} = \underbrace{\frac{1}{\mu_p^* \sigma^*} \nabla^{*2} \mathbf{B}^*}_{\text{diffusion}} + \underbrace{\mathbf{B}^* \cdot (\nabla^* \mathbf{v}^*)}_{\substack{\mathbf{B}^* \text{ field production} \\ \text{by stretching of} \\ \text{magnetic flux lines}}} . \tag{2.14}$$

The terms on the left hand side of Equation 2.14 make up the material derivative of $\mathbf{B}^*$ and the Laplacian term on the right hand side indicates the diffusivity of $\mathbf{B}^*$. The final term $\mathbf{B}^* \cdot (\nabla^* \mathbf{v}^*)$ is the stretching of magnetic flux lines $\mathbf{B}^*$ by the velocity gradient $\nabla^* \mathbf{v}^*$. This serves to increase the magnetic flux density in the direction of stretching.

The transport equation for $\mathbf{B}^*$ (Equation 2.14), Ohm's law (Equation 2.5) and the Lorentz force (Equation 2.9), the latter of which enters the fluid momentum equations (Equation 2.11) as a body force, demonstrate the coupled nature of the magnetic flux density $\mathbf{B}^*$ and the flow field $\mathbf{v}^*$ for incompressible MHD problems. Flow of an electrically conducting fluid exposed to an external magnetic field generates electric current via Ohm's law, which induces its own magnetic flux density via Ampère's law that adds to the original external magnetic field. Simultaneously, the electric current density crossing magnetic flux lines produces a Lorentz force that is applied to the fluid.

Equation 2.14 can be nondimensionalized by defining a characteristic magnetic flux density B_0^*, characteristic velocity magnitude V_0^*, characteristic length L_0^*, and characteristic time $t_{0_{\mathrm{EM}}}^*$. This gives

$$\frac{B_0^*}{t_{0_{\mathrm{EM}}}^*}\frac{\partial \mathbf{B}}{\partial t} + \frac{B_0^* V_0^*}{L_0^*}(\mathbf{v}\cdot\nabla)\mathbf{B} = \frac{1}{\mu_p^*\sigma^*}\frac{B_0^*}{L_0^{*2}}\nabla^2\mathbf{B} + \frac{B_0^* V_0^*}{L_0^*}\mathbf{B}\cdot(\nabla\mathbf{v}). \tag{2.15}$$

Multiplying by $\mu_p^*\sigma^* L_0^{*2}/B_0^*$ gives

$$\underbrace{\frac{\mu_p^*\sigma^* L_0^{*2}}{t_{0_{\mathrm{EM}}}^*}\frac{\partial \mathbf{B}}{\partial t}}_{\text{variation in time}} + \underbrace{\overbrace{\mu_p^*\sigma^* V_0^* L_0^*}^{R_m}(\mathbf{v}\cdot\nabla)\mathbf{B}}_{\text{advection}} = \underbrace{\nabla^2\mathbf{B}}_{\text{diffusion}} + \underbrace{\overbrace{\mu_p^*\sigma^* V_0^* L_0^*}^{R_m}\mathbf{B}\cdot(\nabla\mathbf{v})}_{\substack{\mathbf{B}\text{ field production}\\ \text{by stretching of}\\ \text{magnetic flux lines}}}, \tag{2.16}$$

the *nondimensional transport equation for* $\mathbf{B}$. Here the *magnetic Reynolds number*, defined as

$$R_m = \mu_p^*\sigma^* V_0^* L_0^*, \tag{2.17}$$

represents the ratio of advection to diffusion of $\mathbf{B}$. The transport equation for $\mathbf{B}^*$ with the magnetic Reynolds number R_m as a parameter is

$$\frac{\mu_p^* \sigma^* L_0^{*2}}{t_{0_{\mathrm{EM}}}^*} \frac{\partial \mathbf{B}}{\partial t} + R_m (\mathbf{v} \cdot \nabla)\mathbf{B} = \nabla^2 \mathbf{B} + R_m \mathbf{B} \cdot (\nabla \mathbf{v}). \tag{2.18}$$

The *magnetic diffusivity* η^* is defined as $\eta^* = 1/(\mu_p^* \sigma^*)$, which gives $R_m = V_0^* L_0^* / \eta^*$. This is analogous to the classic viscous Reynolds number $Re_{classic} = V_0^* L_0^* / \nu^*$ where $\nu^* = \mu^*/\rho^*$ is the kinematic viscosity. Note that Equation 2.18 indicates that the nonlinear terms that couple $\mathbf{B}$ and $\mathbf{v}$, namely the advection and stretching, are on the same order.

2.3.2 Decoupling Due To Small Magnetic Reynolds Number

For crystal growth applications, typical values in the laboratory scale are $\mu_p^* \sigma^* \sim 1$ s/m^2, $V_0^* \sim 10^{-2}$ to 10^{-1} m/s and $L_0^* \sim 10^{-2}$ to 10^{-1} m, yielding a relatively small magnetic Reynolds number R_m ($\sim 10^{-4}$ to 10^{-2}). Thus, the advection and stretching terms can be neglected in Equation 2.18, leaving diffusion as the primary $\mathbf{B}$ distribution mechanism in the melt. In the $R_m \ll 1$ limit Equation 2.18 simplifies to

$$\frac{\mu_p^* \sigma^* L_0^{*2}}{t_{0_{\mathrm{EM}}}^*} \frac{\partial \mathbf{B}}{\partial t} = \nabla^2 \mathbf{B}. \tag{2.19}$$

Thus, for typical crystal growth applications there is only one-way coupling. That is, the magnetic field affects the the flow field, but the flow field does not affect the magnetic field. The magnetic field is completely determined by Equation 2.19 with proper initial and boundary conditions. Then the electric field is determined by Faraday's and Ampère's laws (Equation 2.3– 2.4) in conjunction with charge conservation (Equation 2.7). Finally the Lorentz body force (Equation 2.9) is applied to the Navier-Stokes equations.

2.3.3 Shielding Parameter and Skin Depth for Alternating Magnetic Fields

For crystal growth applications with $R_m \ll 1$, Equation 2.18 indicates that diffusion balances the rate of change of $\mathbf{B}$. In typical crystal growth applications the magnetic field is applied by an external source, $\mathbf{B}^*_{\text{ext}}$, driven in consideration of, but independently from the properties of the melt. Thus the time rate of change of $\mathbf{B}^*_{\text{ext}}$ may not be on the same time scale as the response in the melt. If the frequency of the the externally applied magnetic field is sufficiently high, then the time scale of the alternating period of $\mathbf{B}^*_{\text{ext}}$ may be comparable or even shorter than the diffusion time in the melt. Thus, when the frequency is high, the field is unable to completely penetrate the conducting media. The depth at which the magnetic field has mostly penetrated is known as the *skin depth*. The core region beyond the skin depth is largely unaffected by the external magnetic field. This tendency of the magnetic field to be mostly restricted to the skin depth at high alternating frequencies is known as the *shielding effect*.

The shielding effect can be quantified by another dimensionless parameter based on the alternating-current (AC) frequency of the external magnetic field, given by $f^*_{\text{ext}} = \omega^*_{\text{ext}}/(2\pi)$. Taking the characteristic time to be $t^*_{0_{\text{EM}}} = 1/\omega^*_{\text{ext}}$, Equation 2.19 becomes

$$\underbrace{\frac{\mu^*_p \sigma^* L^{*2}_0}{1/\omega^*_{\text{ext}}}}_{R_\omega} \frac{\partial \mathbf{B}}{\partial t} = \nabla^2 \mathbf{B}, \tag{2.20}$$

where the *shielding parameter* R_ω is defined as

$$R_\omega = \mu^*_p \sigma^* \omega^*_{\text{ext}} L^{*2}_0. \tag{2.21}$$

Alternatively, Equation 2.20 can be rewritten as

$$\underbrace{\frac{1}{1/\omega^*_{\text{ext}}}}_{\substack{\text{alternating rate}\\ \text{of } \mathbf{B}^*_{\text{ext}}}} \frac{\partial \mathbf{B}}{\partial t} = \underbrace{\frac{1}{\mu^*_p \sigma^* L^{*2}_0}}_{\substack{\text{diffusion rate}\\ \text{of } \mathbf{B}^*}} \nabla^2 \mathbf{B}. \tag{2.22}$$

The alternating rate of $\mathbf{B}^*_{\text{ext}}$ is $1/(1/\omega^*_{\text{ext}}) = \omega^*_{\text{ext}}$, which implies that the alternating period of $\mathbf{B}^*_{\text{ext}}$ is then $1/\omega^*_{\text{ext}}$. The diffusion rate of $\mathbf{B}^*$ in the conducting media is $1/(\mu^*_p \sigma^* L^{*2}_0) = \eta^*/L^{*2}_0$ and the diffusion time is $\mu^*_p \sigma^* L^{*2}_0 = L^{*2}_0/\eta^*$. Physically the shielding parameter R_ω can therefore be interpreted as the ratios:

$$R_\omega = \frac{\text{alternating rate of } \mathbf{B}^*_{\text{ext}}}{\text{diffusion rate of } \mathbf{B}^*} = \frac{\text{diffusion time of } \mathbf{B}^*}{\text{alternating period of } \mathbf{B}^*_{\text{ext}}}.$$

For sufficiently large AC frequencies f^*_{ext}, the shielding parameter will also be large and the magnetic field will not entirely diffuse into the melt. In the limit of $\omega^*_{\text{ext}} \to \infty$, the shielding parameter $R_\omega \to \infty$ and the magnetic field does not penetrate the melt at all. For small AC frequencies, the magnetic field is able to diffuse deep into the conducting media because $\mathbf{B}^*$ responds completely before $\mathbf{B}^*_{\text{ext}}$ changes. In the limit of $R_\omega \to 0$, either $\omega^*_{\text{ext}} = 0$ and $\mathbf{B}^*_{\text{ext}}$ is steady or $\sigma^* \to \infty$ (the media is a perfect conductor) and $\mathbf{B}^*$ responds instantaneously to changes in $\mathbf{B}^*_{\text{ext}}$.

A generalized solution to Equation 2.20 for a simple sinusoidal forcing of $\mathbf{B}^*_{\text{ext}}$ also suggests the proper scaling for the magnetic skin depth. Assume that at the boundary of the conducting media there is an alternating field traveling tangential to the surface with nondimensional form $B_{y,\text{ext}} = \cos(\omega^*_{\text{ext}} t^*) = \cos(t)$ where y is the nondimensional coordinate tangential to the surface and x is the nondimensional coordinate normal into the melt. If the magnetic Reynolds number is small, then Equation 2.20 applies. If it is assumed that B_y is only a function of x, then a solution found through separation of variables has the form $B_y = \exp(-x/\delta_m)\cos(t - x/\delta_m)$. Here $\delta_m = \sqrt{2/R_\omega}$ is the dimensionless magnetic skin depth. Thus the field decays

exponentially as it moves inside the melt while also experiencing a phase lag when compared to the external field applied at the boundary. This is due to the induced currents in the melt, which shield the interior of the conductor from the applied field [35]. For small δ_m the decay and phase lag are significant. In the limit of $\delta_m \to 0$, the exponential term goes to zero and the external field does not penetrate the melt at all. Conversely, for large δ_m, the exponential term approaches unity and there is no decay, while the phase shift approaches zero so that the magnetic field within the melt approaches that of the applied external field. Based on this analytical solution, the dimensional *magnetic skin depth* is conventionally taken to be

$$\delta_m^* = \sqrt{\frac{2}{\mu_p^* \sigma^* \omega_{\text{ext}}^*}}. \tag{2.23}$$

At high AC frequencies ($\omega_{\text{ext}}^* \gg 1$) the shielding effect is strong, as indicated by a large magnetic shielding parameter R_ω. By the same logic the magnetic skin depth is thin, as shown by Equation 2.23. Thus, the shielding is inversely proportional to the square of skin depth as shown by

$$R_\omega = \mu_p^* \sigma^* \omega_{\text{ext}}^* L_0^{*2} = 2 \left(\frac{L_0^*}{\delta_m^*} \right)^2 = 2\delta_m^{-2}. \tag{2.24}$$

Note that Equation 2.20 with $R_m \ll 1$ has been used to describe the shielding effect and justify the form of the skin depth. However, the physical interpretation applies generally, independent of the magnetic Reynolds number.

2.4 Impact of Magnetic Stirring on the Flow

The impact of the AC frequency $f_{\text{ext}}^* = \omega_{\text{ext}}^*/(2\pi)$ of the external magnetic field varies relative to how fast the melt can respond. There are two considerations associated with two time scales. The first consideration compares the viscous time scale to a

component of the external AC time scale. At high AC frequency the electromagnetic body force may change much faster than flow can respond due to $\omega^*_{\text{ext}} L^*_0 \gg V^*_0$. This exact situation arises when using traveling magnetic fields, as described in Chapter 4. When time averaged, the body force associated with a traveling magnetic field has both a net averaged component and a negligible oscillatory component, the latter of which switches direction before it can impact the flow field.

The second consideration compares the frequency at which the external AC field changes with respect to the response of the EM field in the melt. If the frequency of the external field is very high, the resulting $\mathbf{B}^*$ in the melt may not respond fully before the external field changes. This consideration is measured by the shielding effect associated with $R_\omega > 1$.

When electrically conducting media is exposed to an external alternating magnetic field, electric current $\mathbf{j}^*$ is induced by the relative motion $\mathbf{v}^*_{\text{rel}}$ between the flow and the magnetic field, as described by Ohm's Law (Equation 2.5), reproduced here as

$$\mathbf{j}^* = \sigma^*(\mathbf{E}^* + \mathbf{v}^*_{\text{rel}} \times \mathbf{B}^*). \tag{2.25}$$

In the case of low R_m, the solution of the electric and magnetic fields is decoupled from that of the velocity field. Then, treatment only depends on the frequency at which the external EM fields are driven. Rearranging (Equation 2.19) gives

$$\underbrace{\frac{L^*_0}{t^*_{0_{\text{EM}}}}}_{U_{0_{\text{EM}}}} \frac{\partial \mathbf{B}}{\partial t} = \frac{\eta^*}{L^*_0} \nabla^2 \mathbf{B} \tag{2.26}$$

where $U^*_{0_{\text{EM}}} = L^*_0 / t^*_{0_{\text{EM}}}$ is the characteristic velocity at which the external EM field is driven. If $U^*_{0_{\text{EM}}} \ll \eta^*/L^*_0$, the field will travel or rotate uniformly and slowly (with low frequency) and the magnetic field will be frozen into the fluid. Alternatively, in the high frequency limit $U^*_{0_{\text{EM}}} \gg \eta^*/L^*_0$ and the resulting Lorentz force will include both

a mean component which dominates and a high-frequency oscillatory component that changes faster than the fluid can respond.

2.4.1 Low Magnetic Reynolds Number, Low Frequency Limit

If the imposed magnetic field rotates slowly and in a uniform manner ($U^*_{0_{\mathrm{EM}}} \ll \eta^*/L^*_0$) then $\mathbf{B}^*$ in the melt will have sufficient time to diffuse and will be governed by the Laplacian in Equation 2.26. The field will be frozen into the melt. That is to say, the field in the melt will exactly mimic the externally applied field. While referred to as the low frequency limit, this case is actually better represented by a small shielding parameter, $R_\omega < 1$. Because of the potentially disparate magnitudes of the terms in $R_\omega = \mu^*_p \sigma^* \omega^*_{\mathrm{ext}} L^{*2}_0$, this limit can actually apply to moderate frequencies.

When $R_\omega < 1$ the reference frame can be rotated with $\mathbf{B}^*$ such that it appears steady. With $\partial \mathbf{B}^*/\partial t^* = 0$, Faraday's law (Equation 2.3) reduces to $\nabla^* \times \mathbf{E}^* = 0$. The electric field is then irrotational in this limit, so it can be represented by $\mathbf{E}^* = -\nabla^* \phi^*$, where ϕ^* is the electric potential function. Substituting this expression into Ohm's Law yields

$$\mathbf{j}^*_{R_\omega<1,\text{ in } \mathbf{B}^* \text{ ref. frame}} = \sigma^*(-\nabla^*\phi^* + \mathbf{v}^*_{\mathrm{rel}} \times \mathbf{B}^*). \tag{2.27}$$

This expression will be used in the case of an RMF with

2.4.2 Low Magnetic Reynolds Number, High Frequency Limit

If the imposed magnetic field oscillates with high frequency ($U^*_{0_{\mathrm{EM}}} \gg \eta^*/L^*_0$) then the diffusion of $\mathbf{B}^*$ in the melt will be limited to the skin depth into which it can penetrate before the field changes, governed by the balance of the terms in Equation 2.26. The Lorentz force within this skin depth will still be governed by $\mathbf{j}^* \times \mathbf{B}^*$, but will have both an oscillatory and time-averaged contribution. Since the

fluid has momentum, the high-frequency oscillatory component will change before it can impact the flow. Thus, only the time-averaged component of the Lorentz force is of interest for stirring the melt in crystal growth.

2.4.3 Navier-Stokes Equations Exposed to Alternating Magnetic Fields

The dimensional Navier-Stokes equations (Equation 2.11), with density ρ^* and viscosity μ^* assumed constant, when exposed to an alternating magnetic field, are then

$$\rho^* \frac{\partial \mathbf{v}^*}{\partial t^*} + \rho^* (\mathbf{v}^* \cdot \nabla^*) \mathbf{v}^* = -\nabla^* P^* + \mu^* \nabla^{*2} \mathbf{v}^* + \underbrace{\mathbf{j}^* \times \mathbf{B}^*}_{\mathbf{F}^*_{\mathrm{EM}}}. \tag{2.28}$$

With the relative velocity scale $\mathbf{v}^*_{\mathrm{rel}} = \mathbf{v}_{\mathrm{rel}} V^*_{\mathrm{rel},0}$ to address the contribution from Ohm's law, and the flow time scale $t^*_{0_{\mathrm{flow}}}$ to recognize the difference from the EM time constant, Equation 2.28 becomes

$$\rho^* \frac{V^*_0}{t^*_{0_{\mathrm{flow}}}} \frac{\partial \mathbf{v}}{\partial t} + \rho^* \frac{V^{*2}_0}{L^*_0} (\mathbf{v} \cdot \nabla) \mathbf{v} = -\frac{\Delta P^*_0}{L^*_0} \nabla P + \mu^* \frac{V^*_0}{L^{*2}_0} \nabla^2 \mathbf{v} + \sigma^* V^*_{\mathrm{rel},0} B^{*2}_0 (\mathbf{j} \times \mathbf{B}). \tag{2.29}$$

With $\mathbf{B}^*$ scaled by the characteristic magnetic flux density magnitude B^*_0, this implies that the characteristic electric current density is given by $j^*_0 = \sigma^* V^*_{\mathrm{rel},0} B^*_0$ and thus $\mathbf{j}^*$ is dominated by $\mathbf{v}^* \times \mathbf{B}^*$ in Ohm's law as opposed to $\mathbf{E}^*$. Multiplying every term by $L^*_0/(\rho^* V^{*2}_0)$ gives

$$\frac{L^*_0}{t^*_{0_{\mathrm{flow}}} {}^* V^*_0} \frac{\partial \mathbf{v}}{\partial t} + (\mathbf{v} \cdot \nabla) \mathbf{v} = -\frac{\Delta P^*_0}{\rho^* V^{*2}_0} \nabla P + \frac{\mu^*}{\rho^* V^*_0 L^*_0} \nabla^2 \mathbf{v} + \frac{\sigma^* V^*_{\mathrm{rel},0} B^{*2}_0 L^*_0}{\rho^* V^{*2}_0} (\mathbf{j} \times \mathbf{B}). \tag{2.30}$$

Substituting the characteristic time $t^*_{0_{\mathrm{flow}}} = L^*_0/V^*_0$, the characteristic inertial pressure difference $\Delta P^*_0 = \rho^* V^{*2}_0$, and the characteristic velocity $V^*_0 = \nu^*/L^*_0$, the nondimensional Navier-Stokes equations become

$$\frac{\partial \mathbf{v}}{\partial t} + (\mathbf{v} \cdot \nabla) \mathbf{v} = -\nabla P + \underbrace{\frac{\mu^*}{\rho^* V^*_0 L^*_0}}_{\frac{1}{Re_{\mathrm{classic}}}} \nabla^2 \mathbf{v} + \frac{\sigma^* V^*_{rel,0} B^{*2}_0 L^{*3}_0}{\rho^* \nu^{*2}} (\mathbf{j} \times \mathbf{B}). \tag{2.31}$$

The choice of a viscous velocity scale $V_0^* = \mu^*/(\rho^* L_0^*)$ requires $Re_{\text{classic}} = 1$. Thus, the Navier-Stokes equations take the final form

$$\frac{\partial \mathbf{v}}{\partial t} + (\mathbf{v} \cdot \nabla)\mathbf{v} = -\nabla P + \nabla^2 \mathbf{v} + \frac{\sigma^* V_{rel,0}^* B_0^{*2} L_0^{*3}}{\rho^* \nu^{*2}} (\mathbf{j} \times \mathbf{B}). \tag{2.32}$$

The nondimensional form of incompressible, constant density continuity is

$$\nabla \cdot \mathbf{v} = 0. \tag{2.33}$$

Together, Equations 2.32 and 2.33 and the no-slip, no-penetration boundary conditions on all surfaces govern the fluid flow problem, which is decoupled from the EM problem in the low R_m limit. The fluid is considered isothermal in this work, so the energy equation is not required. The choice of $V_{rel,0}^*$ is specific to the field of interest and will be shown in Chapter 3 for a RMF and Chapter 4 for a TMF.

Chapter 3

Rotating Magnetic Field

The first method of stirring to be analyzed is that obtained from the use of a rotating magnetic field (RMF). The goal of the RMF is to suppress thermal oscillations and enhance mixing during solidification, but this must be done in laminar conditions. Therefore, it is important to know the point at which the flow will transition to a new flow regime and to know the physics of this instability. The basic physics of the laminar RMF-driven flow is that the flow is predominantly azimuthal but is accompanied by a meridional secondary flow due to an imbalance between centrifugal force and radial pressure gradient inside the layers at $z = \pm R$ [36].

Figure 3.1 shows the model for the RMF case. The flow is exposed to an external alternating magnetic field. In the RMF case, the ideal magnetic field has the analytical form

$$\mathbf{B}^*_{\mathrm{ext}_{\mathrm{analytic}}} = B_0^*[\cos(\theta - \omega^*_{\mathrm{ext}} t^*)\hat{\mathbf{e}}_r - \sin(\theta - \omega^*_{\mathrm{ext}} t^*)\hat{\mathbf{e}}_\theta], \tag{3.1}$$

where B_0^* and ω^*_{ext} are the magnitude and the rotation angular frequency of the external rotating magnetic field, respectively. The azimuthal coordinate is θ, the dimensional time is t^*, and $\hat{\mathbf{e}}_r$ and $\hat{\mathbf{e}}_\theta$ are the radial and azimuthal unit vectors, respectively. The analytic external magnetic field alternates at AC frequency $f^*_{\mathrm{ext}} = \omega^*_{\mathrm{ext}}/(2\pi)$.

As shown in Chapter 2, $\mathbf{B}^*$ is decoupled from the flow field for small magnetic Reynolds number R_m for crystal growth applications. As a result, the coupling is

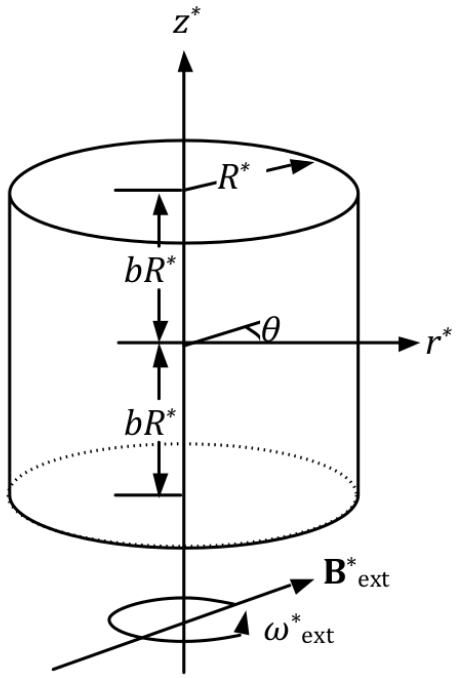

Figure 3.1 : The cylindrical melt domain exposed to an external magnetic field $\mathbf{B}^*_{\text{ext}}$ rotating with frequency $f^*_{\text{ext}} = \omega^*_{\text{ext}}/(2\pi)$.

one-way so that the fluid "feels" the effects of the magnetic field, but the flow does not influence the electromagnetics. Thus, the EM equations are first solved to find the Lorentz body forces, which are then applied to the fluid in the solution of the flow equations. Therefore, $\mathbf{B}^*$ is determined completely by

$$\underbrace{\frac{\mu_p^* \sigma^* L_0^{*2}}{1/\omega^*_{\text{ext}}}}_{R_\omega} \frac{\partial \mathbf{B}}{\partial t} = \nabla^2 \mathbf{B}, \tag{3.2}$$

where the *shielding parameter* R_ω is defined as

$$R_\omega = \mu_p^* \sigma^* \omega^*_{\text{ext}} L_0^{*2}, \tag{3.3}$$

solved in conjunction with Faraday's law, Ampère's law and conservation of charge. The boundaries of the melt are insulating, such that the normal component of the charge is zero on each surface.

The nondimensional equations for fluid flow from Chapter 2 are the Navier-Stokes equations (Equations 2.32)

$$\frac{\partial \mathbf{v}}{\partial t} + (\mathbf{v} \cdot \nabla)\mathbf{v} = -\nabla P + \nabla^2 \mathbf{v} + \frac{\sigma^* V^*_{rel,0} B^{*2}_0 L^{*3}_0}{\rho^* \nu^{*2}} \mathbf{j} \times \mathbf{B}, \tag{3.4}$$

and incompressible continuity (Equation 2.33)

$$\nabla \cdot \mathbf{v} = 0, \tag{3.5}$$

where the viscous Reynolds number has been set to unity by the choice of the viscous velocity scale $V^*_0 = \mu^*/(\rho^* L^*_0)$, and $\mathbf{B}^*$ and $\mathbf{j}^*$ have been scaled by B^*_0 and $\sigma^* V^*_{\text{rel},0} B^*_0$, respectively. For a RMF the relative velocity scale $V^*_{rel,0} = \omega^*_{\text{ext}} L^*_0$ is introduced to get the Navier Stokes equations forced by a rotating magnetic field

$$\frac{\partial \mathbf{v}}{\partial t} + (\mathbf{v} \cdot \nabla)\mathbf{v} = -\nabla P + \nabla^2 \mathbf{v} + \underbrace{\frac{\sigma^* \omega^*_{\text{ext}} B^{*2}_0 L^{*4}_0}{\rho^* \nu^{*2}}}_{2 \times Ta_m} \mathbf{j} \times \mathbf{B} \tag{3.6}$$

where the *magnetic Taylor number*[1]

$$Ta_m = \frac{\sigma^* \omega^*_{\text{ext}} B^{*2}_0 L^{*4}_0}{2\rho^* \nu^{*2}} \tag{3.7}$$

indicates the strength of the electromagnetic body force of a rotating magnetic field relative to viscous effects. The factor of 2 is typically absorbed into the scaling on the electromagnetic body force, where $\mathbf{F}^*_{\text{EM}}$ then scales as $\sigma^* \omega^*_{\text{ext}} B^{*2}_0 L^*_0/2$. The resulting nondimensional Navier-Stokes equations when exposed to a rotating magnetic field are

$$\frac{\partial \mathbf{v}}{\partial t} + (\mathbf{v} \cdot \nabla)\mathbf{v} = -\nabla P + \nabla^2 \mathbf{v} + Ta_m \mathbf{F}_{\text{EM}}. \tag{3.8}$$

The magnetic Taylor number is the parameter that governs the flow and will be used to define the point of instability.

[1] Analogous to the more common *Taylor number* $Ta = 4\omega^{*2} L^{*4}_0/\nu^{*2}$, which measures the relative importance of centrifugal forces as compared to viscous effects.

Table 3.1 : Physical properties of the melt (held constant) and resulting derived scales used for all computations involving the RMF. Note that the viscous velocity scale is equal to ν^*/L_0^*, giving a classic viscous Reynolds number of one.

magnetic permeability $\mu_p^* = \mu_0^*$	$4\pi \times 10^{-7}$ N/A^2
electrical conductivity σ^*	945,000 S/m
density ρ^*	6135 kg/m^3
kinematic viscosity ν^*	1.74×10^{-7} m^2/s
length scale $L_0^* = R^*$	0.01275 m
resulting derived scales:	
magnetic diffusivity $\eta^* = 1/(\mu_p^* \sigma^*)$	1.1875 m^2/s
viscous velocity scale V_0^* (such that $Re_{classic} = 1$)	1.365×10^{-5} m/s
flow time scale $t_{0_{\text{flow}}}^* = L_0^*/V_0^*$	934.0 s
magnetic Reynolds number $R_m = \mu_p^* \sigma^* V_0^* L_0^* = V_0^* L_0^*/\eta^*$	1.466×10^{-7}

The physical parameters used throughout this chapter for all computations and calculations are listed in Table 3.1. The parameters that are varied include the AC frequency f^* at which the RMF is driven and the electric current density j_c^* in the coils. These subsequently impact ω_{ext}^*, $t_{0_{\text{EM}}}^*$ and the characteristic velocity at which the external EM field is driven $U_{0_{\text{EM}}}^*$, and allow for a parametric study of the effects of R_ω, δ_m and Ta_m, the results of which are presented in Section 3.4. The resulting impact on the stability of the base flow is presented in Section 3.5 for axisymmetric instabilities and Section 3.6 for non-axisymmetric instabilities.

3.1 RMF Model

The numerical 'lab' setup approximates the experimental setup, which both aim for producing the analytic RMF of the form in Equation 3.1. Physically, the target analytic RMF is a constant magnetic field aligned in a particular direction at each time instance of the AC cycle.

To get the EM body forces, the equations of electromagnetism are solved for the RMF setup in Opera shown in Figure 3.2 [37]. The RMF is generated by using six solenoids equally spaced around the melt, each with the same current running through it where adjacent solenoids have 60 degree phase shifts. That is, when one solenoid is at 0 degrees of an AC cycle at a particular time instance, the other solenoids at that same time instance are at 60, 120, 180, 240, 320 degrees, respectively, in the clockwise direction when viewing from the $\hat{\mathbf{e}}_z$ direction.

At a given AC frequency, only the current running through each coil changes from one simulation to the next, and this is done to achieve a particular magnetic Taylor number. The geometry of the RMF setup remains constant for each run. The physical parameters for the melt are chosen to approximate actual parameters

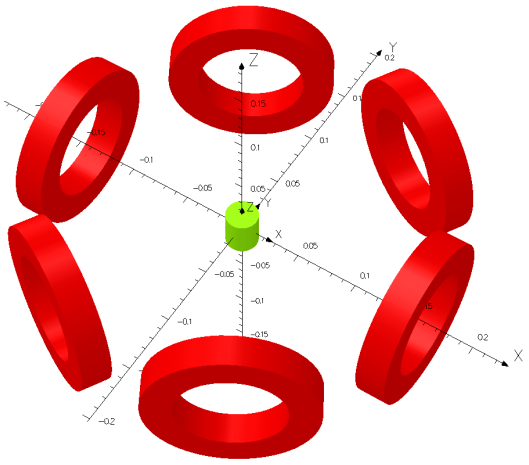

Figure 3.2 : Opera model consisting of six AC solenoids (red rings) to generate the RMF and a melt region (green cylinder) in the center. The RMF is generated by alternating current running through each coil, with 60 degree phase shifts between adjacent coils.

in laboratory experiments. The radius of the melt is $R^* = 0.01275$ m with a total length $2R^* = 0.0255$ m and the conductivity is set to $945,000$ S/m, matching that of GaInSb [38].

The dimensions of the coil were chosen somewhat arbitrarily since the current can be changed to produce the desired magnetic field strength. However, the coil must be made large enough in order to subject the entire melt to a uniform field. For reference, the inner and outer radius of each solenoid is 0.042 m and 0.066 m, respectively, so that the cross-sectional area of each solenoid is a 0.024 m by 0.024 m square.

The solution domain complete with a mesh is shown in Figure 3.3. The melt is surrounded by cylinders that are given the properties of air and extend to $r^* = 0.1$ m and $z^* = 0.1$ m. The symmetry inherent in the physics of the problem has been used to reduce the domain to one quarter of the full domain. Axial symmetry is

assumed with respect to the $z^* = 0$ plane and rotational symmetry about the axis is set between the $\theta = 0$ and $\theta = \pi$ planes.

The mesh shown in the figure contains an unstructured mixed set of linear and quadratic tetrahedral elements. The "air cylinders" that surround the melt are used to control the size of the elements. The melt is set to have a maximum element size of 0.0005 m and the air cylinders have maximum element sizes of 0.001 m, 0.002 m, 0.004 m and 0.008 m, respectively, moving outward radially away from the melt. Additionally, the mesher in Opera is often more successful when each air cylinder is cut into smaller segments, which can be seen outlined in pink in Figure 3.3(b). Overall, the mesh has approximately 1.26 million elements and 0.397 million nodes. Note that in Opera the solenoids are not part of the finite element discretization as the magnetic field is calculated at each node by integrating over all solenoids using the Biot-Savart law.

Once meshed, Opera's ELEKTRA Steady State solver is employed to solve the problem, with a typical run lasting 10-15 minutes and using approximately 1.5–2 GB of memory. The resulting fields are viewed in Opera's post-processing tool and the Lorentz forces are calculated. To get time- and azimuthally-averaged force fields, the three (Cartesian) force components are first sampled in a three-dimensional block fully containing the melt at 180 distinct, evenly-spaced time instances over a complete AC cycle. Then, the data is averaged to give the time-averaged forces within the block. This block is then loaded into Matlab where it is linearly interpolated onto the melt cylinder, the forces are converted to cylindrical coordinates, and then averaged azimuthally. The final step in computing the Lorentz forces is a correction to the interpolation that Opera performs when outputting the forces. At the cylinder boundaries the Opera interpolation has an incorrect dip in the forces, apparently due

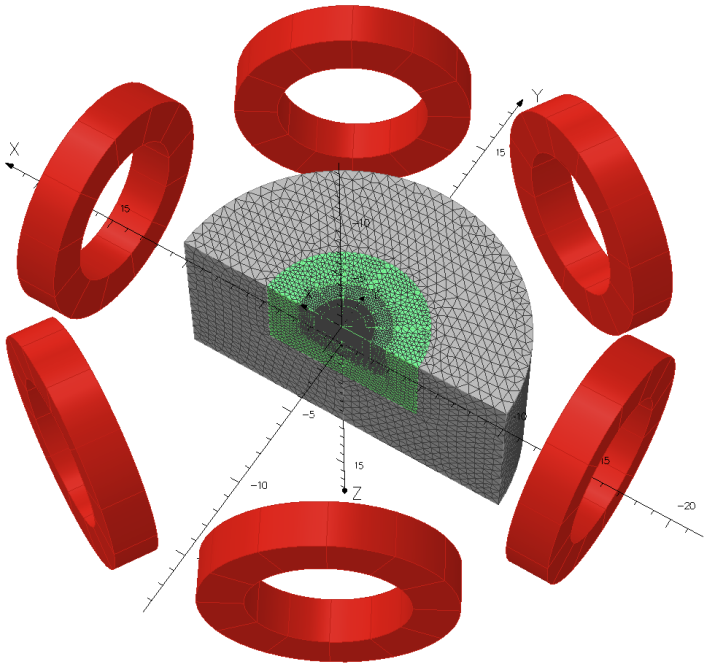

(a)

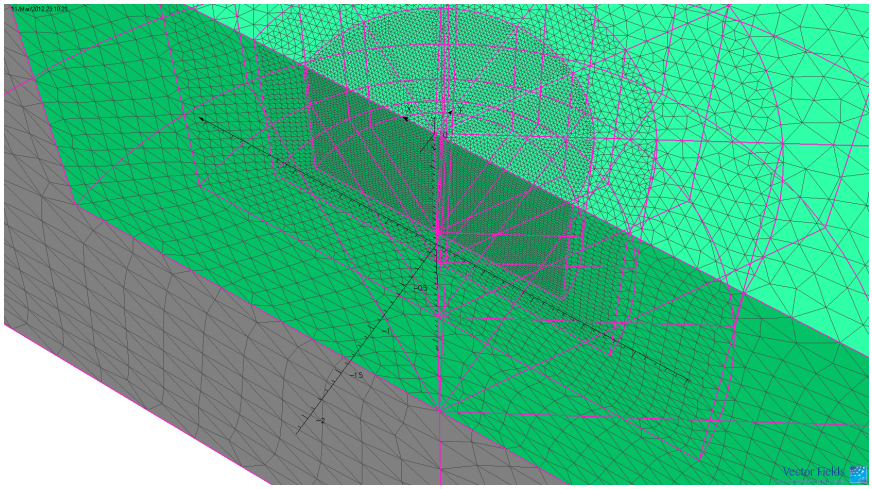

(b)

Figure 3.3 : a) The entire mesh used for the RMF simulations in Opera with only a quarter of the domain simulated due to symmetry and b) a close-up on the mesh showing fineness of the melt and the smaller divisions (outlined in pink) made in the model body to help meshing. A total of 1.26×10^6 elements and 3.97×10^5 nodes were used.

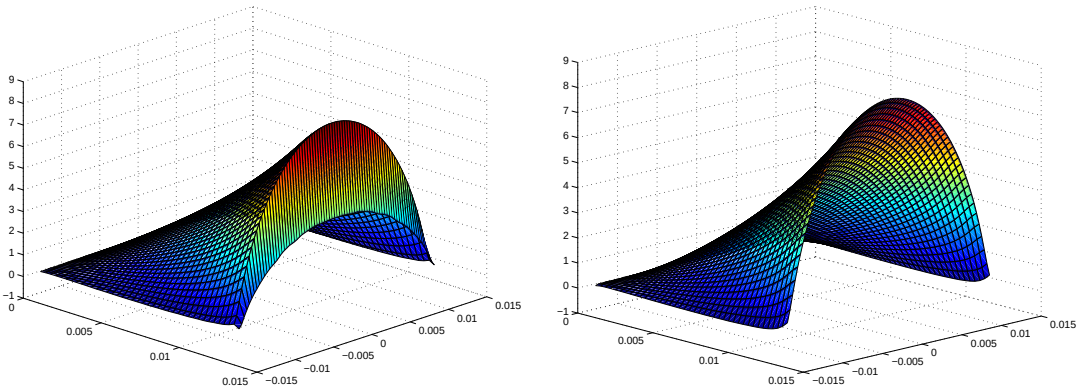

(a) (b)

Figure 3.4 : The azimuthal force a) obtained from Opera with incorrect values on the radial surface and b) the corrected azimuthal force found through cutting the edges and extrapolating using Matlab.

to interpolation with a node that is outside the melt where the force drops to zero. This error is shown in Figure 3.4(a) for the azimuthal force at the very last set of nodes on the radial surface . To correct this, the data on the three non-axis boundaries are removed and new data is approximated through Matlab's *v4* extrapolation method within the *griddata* routine [39]. Figure 3.4(b) shows the new, corrected azimuthal force that results from this extrapolation.

The magnitude of the magnetic flux density is also carried through this calculation process along with the forces so that the appropriate magnetic Taylor number can be calculated. The characteristic magnetic flux density used throughout this work is the maximum of the time- and azimuthally-averaged magnitude of $\mathbf{B}^*$ and is expressed as $\langle B^* \rangle_{\bar{\theta},max}$. This value is compared to B_0^* from the analytical solution.

3.2 Electromagnetics of the RMF

The purpose of this work is to investigate the deviation of a RMF generated in a 'lab' from that approximated by the analytic solution $\mathbf{B}^*_{\text{ext}_{\text{analytic}}}$ given by Equation 3.1. All cases in this chapter are in the low magnetic Reynolds number limit, $R_m \ll 1$, such that secondary EM fields induced by the flow of the electrically conducting melt are always negligible. This is verified by the extremely low value of R_m given in Table 3.1.

Additionally, in the low frequency limit associated with $R_\omega \ll 1$, there is negligible shielding and the magnetic flux density in the melt will be identical to that if the melt was removed. It is useful to first describe the physics in this limit. The shielding parameter requires

$$R_\omega = \mu_p^* \sigma^* R^{*2} \omega_{\text{ext}}^* = \mu_p^* \sigma^* R^{*2} (2\pi f_{\text{ext}}^*) \ll 1 \tag{3.9}$$

for the low frequency approximation to remain valid. Substituting in the values $\mu_p^* = \mu_0^* = 4\pi \times 10^{-7}$ N/A^2, $\sigma^* = 945{,}000$ S/m and $R^* = 0.01275$ m, the low frequency approximation is valid when

$$f_{\text{ext}}^* \ll 824 \text{ Hz}. \tag{3.10}$$

In addition to $R_m \ll 1$ and $R_\omega \ll 1$, it is easiest to interpret first the case of an infinitely long, cylindrical melt, as in Section 3.2.1. Then a finite length melt with $R_m \ll 1$ and $R_\omega \ll 1$ will be treated in Section 3.2.2. Finally, the EM fields at arbitrary R_ω for a finite length melt are discussed in Section 3.2.3.

First, shown in Figure 3.5 is the $\mathbf{B}^*_{\text{lab}}$ field generated by the 6 coil arrangement in Opera within the melt region, but the melt properties have been replaced by those of air, similar to the study described in Huang *et al.* [6]. As the figure shows, there is

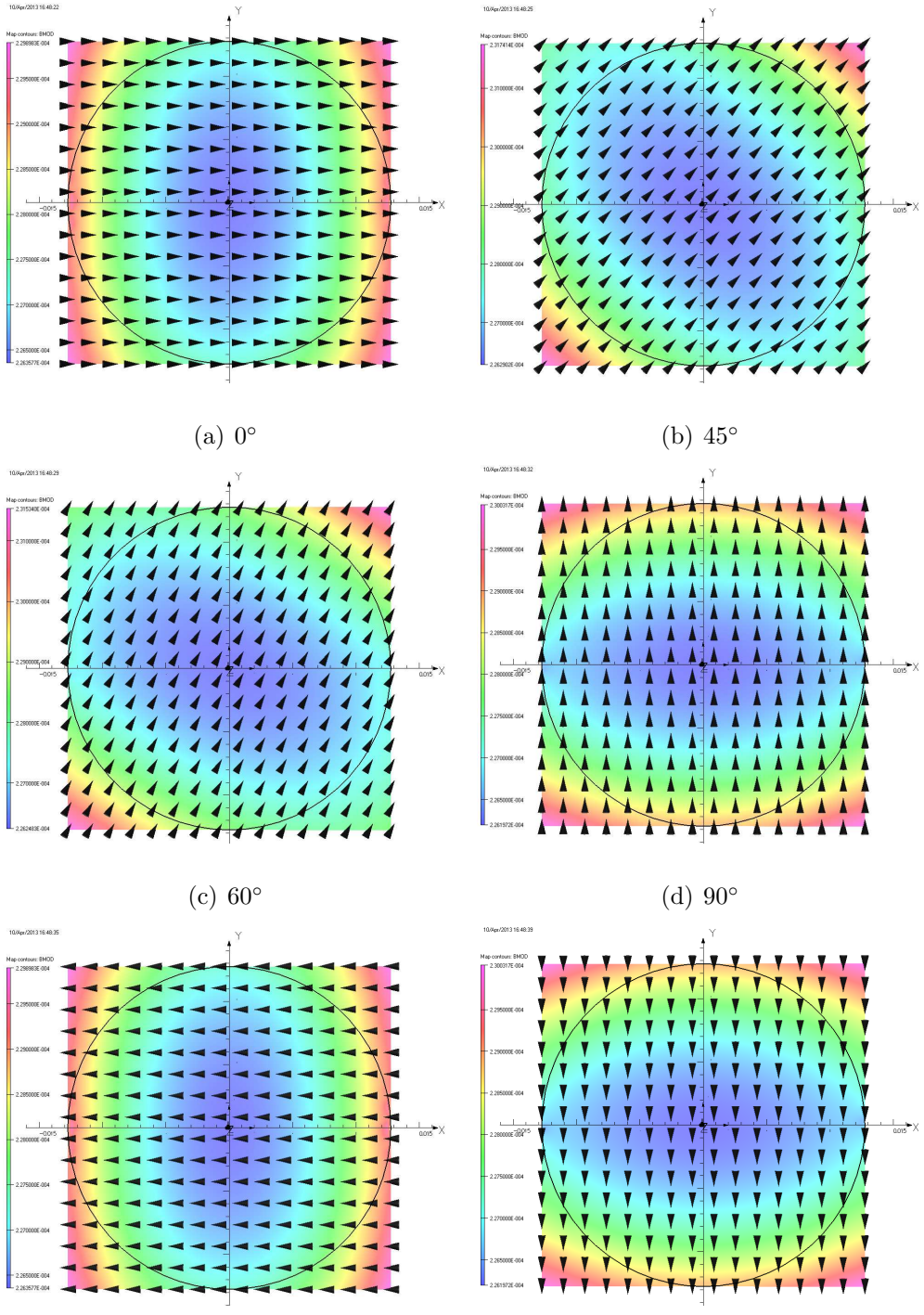

(a) 0° (b) 45°

(c) 60° (d) 90°

(e) 180° (f) 270°

Figure 3.5 : The magnetic flux density at the midplane at several time instances in an AC cycle of the RMF at $f^*_{\text{ext}} = 1$ Hz *with the melt replaced by air* and a total current in each solenoid of 209.23 A. The color and vectors indicate the magnitude and direction of $\mathbf{B}^*_{\text{lab}}$, respectively. The black circle denotes the melt boundary.

already some variation in the magnitude of the 'lab' field even without a conductor present. For instance, the maximum magnitude of the magnetic flux density at 0° of the AC cycle is 2.2977×10^{-4} T and the minimum is 2.2636×10^{-4} T, yielding a variation of 1.5% over the midplane of the melt domain. The corresponding $\mathbf{B}^*_{\text{lab}}$ field *with* the melt present is shown in Section 3.2.3.

3.2.1 Interpretation of RMF Stirring with $R_\omega \ll 1$ for an Infinitely Long, Cylindrical Melt

Consider a cylindrical conducting melt, infinitely long in $\hat{\mathbf{e}}_z$, exposed to the analytical form (Equation 3.1) for the RMF external magnetic flux density

$$\mathbf{B}^*_{\text{ext}_{\text{analytic}}} = B^*_0[\cos(\theta - \omega^*_{\text{ext}} t^*)\hat{\mathbf{e}}_r - \sin(\theta - \omega^*_{\text{ext}} t^*)\hat{\mathbf{e}}_\theta]. \tag{3.11}$$

Assuming the low frequency approximation ($R_\omega \to 0$), the magnetic flux density in the melt mimics that of the exterior applied field such that $\mathbf{B}^* = \mathbf{B}^*_{\text{ext}_{\text{analytic}}}$.

The electric current density in the melt is governed by the low frequency version of Ohm's law (Equation 2.27) reproduced here as

$$\mathbf{j}^*_{R_\omega<1,\text{ in } \mathbf{B}^* \text{ ref. frame}} = \sigma^*(-\nabla^*\phi^* + \mathbf{v}^*_{\text{rel}} \times \mathbf{B}^*). \tag{3.12}$$

The relative velocity, $\mathbf{v}^*_{\text{rel}}$, is the flow velocity relative to the velocity of the magnetic field. Typically the fluid velocity is small and can be neglected relative to the rotational velocity of the magnetic field. Thus the relative velocity can be approximated as the negative of the magnetic field velocity, $\mathbf{v}^*_{\text{rel}} = -\omega^*_{\text{ext}} r^* \hat{\mathbf{e}}_\theta$, indicating that the relative velocity is highest near the radial boundary.

Taking the divergence of Equation 3.12 zeros the left hand side due to conservation of charge and zeros the $\mathbf{v}^*_{\text{rel}} \times \mathbf{B}^*$ term because the cross product results in a component

in only the z^* direction that is independent of z^*, which drops out once the divergence operator is applied. Thus Equation 3.12 reduces to

$$\nabla^{*2}\phi^*\Big|_{R_\omega \ll 1,\, \mathbf{v}^*_{\mathrm{rel}}(\theta),\, \mathbf{B}^*(r^*,\theta)} = 0. \tag{3.13}$$

At the radial surface the condition $\mathbf{j}^*\Big|_{R_\omega \ll 1} \cdot \hat{\mathbf{n}} = \sigma^*(-\nabla^*\phi^* + \mathbf{v}^*_{\mathrm{rel}} \times \mathbf{B}^*) \cdot \hat{\mathbf{n}} = 0$ is applied. Here $\hat{\mathbf{n}} = \hat{\mathbf{e}}_r$ and the cross product term drops out since it has no r^* component, leaving $\nabla^*\phi^* \cdot \hat{\mathbf{n}} = 0$ on the boundary. Consequently, $\nabla^*\phi^* = 0$ throughout the domain and Equation 3.12 becomes simply

$$\mathbf{j}^*\Big|_{R_\omega \ll 1,\, \nabla\phi^* = 0} = \sigma^*(\mathbf{v}^*_{\mathrm{rel}} \times \mathbf{B}^*) = -\sigma^*\omega^*_{\mathrm{ext}} B_0^* r^* \cos(\theta - \omega^*_{\mathrm{ext}} t^*)\hat{\mathbf{e}}_z. \tag{3.14}$$

Thus, electric current is generated by flow in the negative azimuthal direction that crosses the magnetic field lines, which are theoretically all aligned and restricted to a constant z-plane. As a result, this electric current is entirely in the z^* direction, linear in r^*, and sinusoidal in θ. Consider the case at $t^* = 0$ where the magnetic field is aligned with $\theta = 0$. The current will be in the $+\hat{\mathbf{e}}_z$ direction and at its maximum at the radial surface. It will vary sinusoidally in the azimuthal direction so that at $\theta = \pi/2$ the current is zero and is in the $-\hat{\mathbf{e}}_z$ direction at $\theta = \pi$.

The Lorentz force in the infinitely long cylinder is then given by the current crossing the magnetic field $\mathbf{F}^*_{\mathrm{EM}} = \mathbf{j}^* \times \mathbf{B}^*$

$$\begin{aligned} &\mathbf{F}^*_{\mathrm{EM}}\Big|_{R_\omega \ll 1,\, \infty\text{-long}} = \\ &\sigma^*\omega^*_{\mathrm{ext}} B_0^{*2} r^* \left[\cos(\theta - \omega^*_{\mathrm{ext}} t^*)\sin(\theta - \omega^*_{\mathrm{ext}} t^*)\hat{\mathbf{e}}_r + \cos^2(\theta - \omega^*_{\mathrm{ext}} t^*)\hat{\mathbf{e}}_\theta\right]. \end{aligned} \tag{3.15}$$

Time-averaging this force leaves only the azimuthal component such that

$$\langle \mathbf{F}^*_{\mathrm{EM}} \rangle\Big|_{R_\omega \ll 1,\, \infty\text{-long}} = \frac{1}{2}\sigma^*\omega^*_{\mathrm{ext}} B_0^{*2} r^* \hat{\mathbf{e}}_\theta. \tag{3.16}$$

From this solution, it can be seen that the force is simply linear in the radial direction and entirely azimuthal for the infinite cylinder.

3.2.2 Analytic Solution for the RMF Body Force in a Finite Length, Cylindrical Melt with $R_\omega \ll 1$

By using a finite cylinder, the previous analysis has to be amended. The external magnetic flux density for stirring a finite length melt is still taken as $\mathbf{B}^*_{\mathrm{ext}_{\mathrm{analytic}}}$ given by Equation 3.1. Furthermore, in a long cylinder, the infinite cylinder solution is still dominant away from the axial boundaries. Near the boundaries, the no-penetration condition for the current density must be obeyed, and much like in potential fluid flow, the current must turn and slip along the boundary. This strong radial component in the current causes a drop in the azimuthal force as it approaches the axial boundary.

The body force typically used in analyses of RMF-driven flows in finite conducting cylinders is axisymmetric and assumed to have only an azimuthal component [40, 41]. The nondimensional, azimuthal, time-averaged analytic body force is given by

$$\langle F_{\mathrm{EM},\theta} \rangle \Big|_{R_\omega \ll 1,\, \mathrm{finite,\, analytic}} = r - 2 \sum_{N=1}^{\infty} \frac{J_1(\zeta_N r) \cosh(\zeta_N z)}{(\zeta_N^2 - 1) J_1(\zeta_N) \cosh(b\, \zeta_N)}, \tag{3.17}$$

where J_k is the Bessel function of the first kind and k^{th} order, r and z are the nondimensional radial and axial coordinates, respectively, b is the aspect ratio of the melt cylinder, and ζ_N are roots of $\zeta_N J_0(\zeta_N) - J_1(\zeta_N) = 0$. This body force is based on a low frequency approximation and a subsequent separation of variables solution. This means that AC frequencies are sufficiently low such that the magnetic shielding effect is weak and the magnetic skin depth is much thicker than the melt radius. Thus, $\mathbf{B}^*$ within the melt is taken to be $\mathbf{B}^*_{\mathrm{ext}_{\mathrm{analytic}}}$. A plot of the analytic body force is included in Figure 3.10, where it is compared to the numerical 'lab' generated body forces from Opera at various f^*_{ext}.

3.2.3 Lab Body Forces in a Finite Length, Cylindrical Melt at Arbitrary R_ω, Compared to the Analytic Body Force Valid at $R_\omega \ll 1$

The numerical solution for the body force in Opera is set up to approximate experimental configurations and thus will be referred to as the 'lab' field. The notation for the various lab magnetic flux density fields of interest is as follows. The instantaneous, dimensional lab magnetic flux density is given by $\mathbf{B}^*_{\text{lab}}$. The dimensional magnitude is given by the unbolded symbol B^*_{lab}. A time-averaged quantity is represented by surrounding $\langle\,\rangle$. An azimuthally averaged quantity is represented by subscript $\overline{\theta}$.

Figure 3.6 shows the corresponding instantaneous 'lab' field $\mathbf{B}^*_{\text{lab}}$ at a frequency of 1 Hz at different angles in the AC cycle for a finite melt, generated by Opera. Since $R_\omega \sim O(10^{-3})$ at 1 Hz, the field appears as expected with all arrows pointing in the direction of the AC angle and the magnitude nearly constant, varying between 2.3118×10^{-4} T and 2.3416×10^{-4} T, at 0° in the AC cycle, representing a 1.3% variation across the midplane of the melt, similar to that when the melt was replaced by air in Figure 3.5. In the analytical RMF (Equation 3.1) the magnitude of magnetic flux density is constant throughout the melt. In comparison, the magnitude B^*_{lab} shown in Figure 3.6 varies slightly due to the finite number of coils.

To better visualize the lab fields, the instantaneous magnetic flux density, electric current density, and resulting electromagnetic Lorentz body force for the $f^*_{\text{ext}} = 1$ Hz case are shown in Figure 3.7 at 0° in the AC cycle, when the magnetic field is along the x^* axis. As in the analytical approximation, $\mathbf{B}^*_{\text{lab}}$ is nearly constant throughout the melt and is aligned with the external field and $\mathbf{j}^*_{\text{lab}}$ has negligible contribution in the θ-direction (y^*-direction in the plane and instance shown). As predicted by the analytic solution, the EM body force $\mathbf{F}^*_{\text{EM, lab}}$ for the RMF is almost entirely in the azimuthal direction for this low frequency case with $R_\omega \sim O(10^{-3})$.

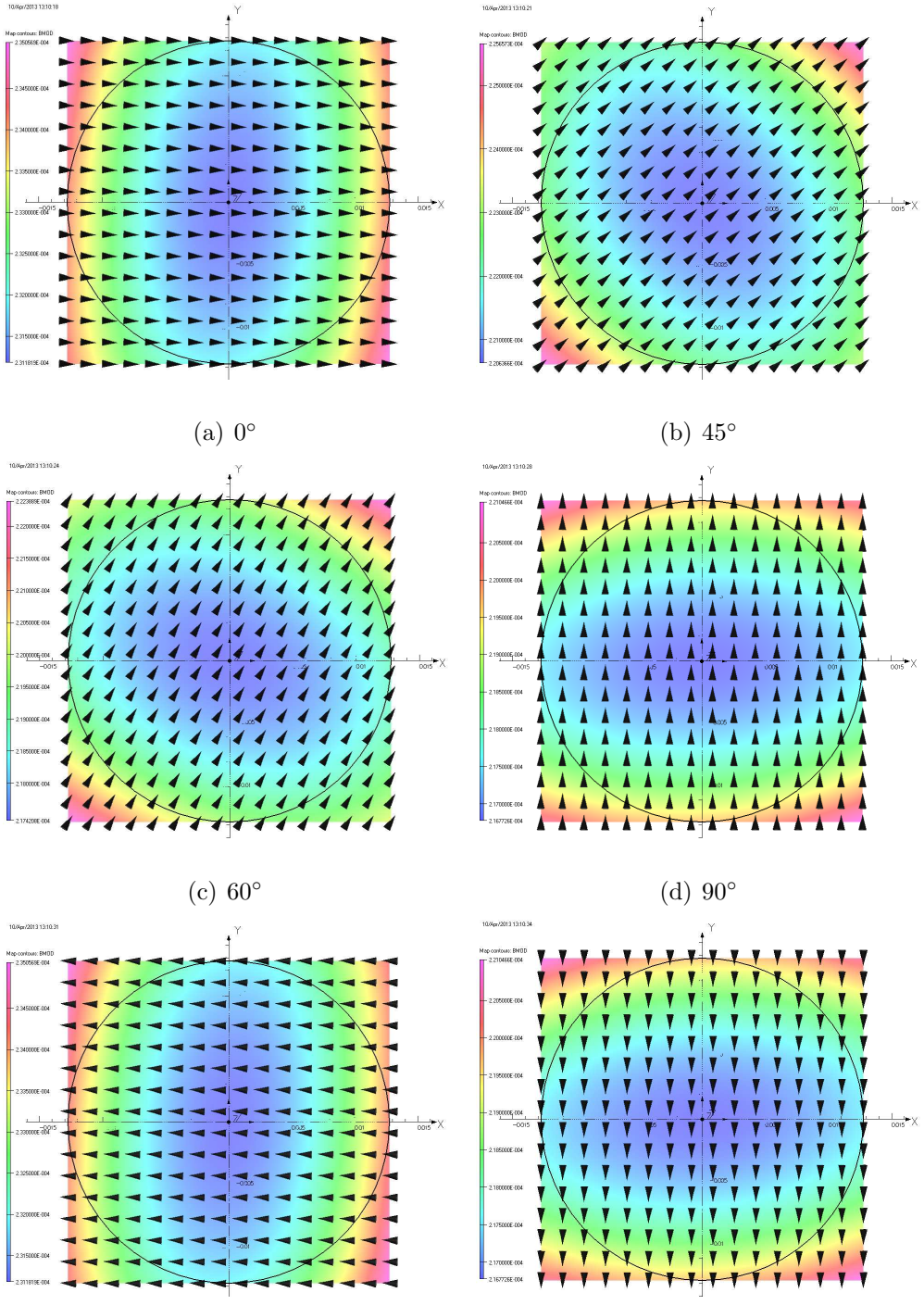

(a) 0° (b) 45°

(c) 60° (d) 90°

(e) 180° (f) 270°

Figure 3.6 : The magnetic flux density at the midplane at several time instances in an AC cycle of the RMF at $f^*_{\text{ext}} = 1$ Hz with the total current in each solenoid set to 209.23 A. The color and vectors indicates the magnitude and direction of $\mathbf{B}^*_{\text{lab}}$, respectively. The black circle denotes the melt boundary.

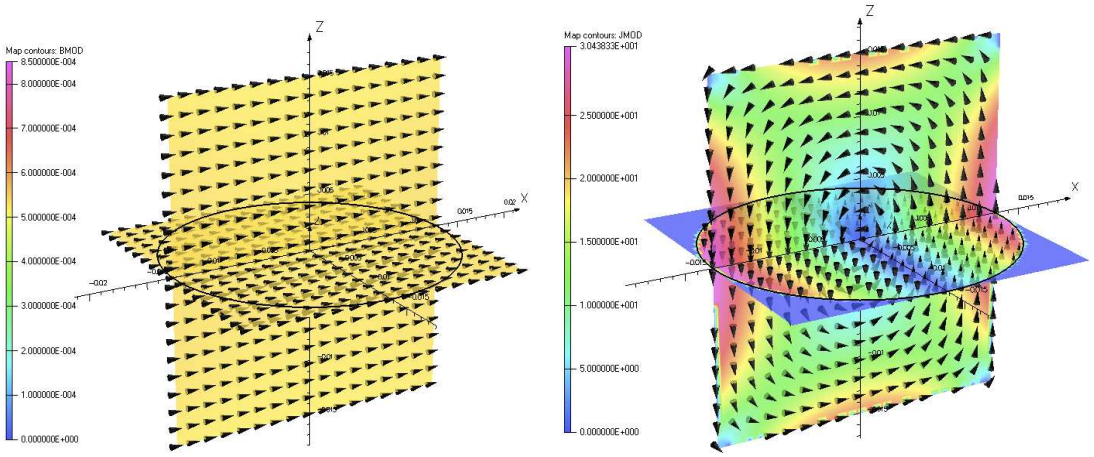

(a) $\mathbf{B}^*_{\text{lab}}$ (b) $\mathbf{j}^*_{\text{lab}}$

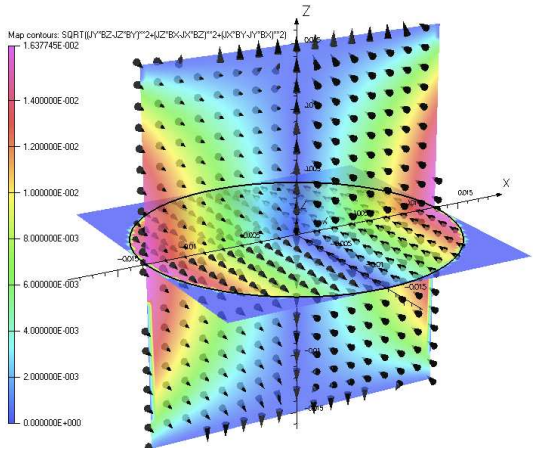

(c) $\mathbf{F}^*_{\text{EM, lab}}$

Figure 3.7 : Non-time-averaged fields for the the magnetic flux density, electric current density, and electromagnetic force with $f^*_{\text{ext}} = 1$ Hz at 0° of the AC cycle and the total current in each solenoid set to 209.23 A. The arrows denote direction and the color denotes magnitude.

At high frequencies the external magnetic field does not completely penetrate the melt so that B^*_{lab} is larger at the radial surface than near the axis. Figure 3.8 shows how the the shape of the time- and azimuthally-averaged B^*_{lab}, indicated by $\langle B^*_{\text{lab}} \rangle_{\overline{\theta}}$, changes with increases in frequency. As expected, as the frequency grows and the magnetic shielding effect increases, the magnetic field can not penetrate all the way to the centerline, so there is a higher $\langle B^*_{\text{lab}} \rangle_{\overline{\theta}}$ at the radial surface.

Figure 3.9 shows how much $\langle B^*_{\text{lab}} \rangle_{\overline{\theta}}$ varies over the r-z plane. The maximum of $\langle B^*_{\text{lab}} \rangle_{\overline{\theta},\text{max}}$ is denoted $B^*_{0,\text{lab}}$ and is taken as the magnitude appearing in the definition of magnetic Taylor number for the 'lab' fields. $B^*_{0,\text{lab}}$ does not vary much, only rising approximately 0.1 Gauss from $f^*_{\text{ext}} = 10$ Hz to $f^*_{\text{ext}} = 4000$ Hz, whereas $\langle B^*_{\text{lab}} \rangle_{\overline{\theta},\text{min}}$ drops off by 0.4 Gauss over the same range of frequencies.

Because of the magnetic shielding effect, the numerical body force diverges from the analytic force at high frequencies. Figure 3.10 compares the shape of the force field for the analytic solution with the lab force from numerical simulations. The forces are normalized in this figure and it is initially difficult to see any difference between the analytic force field and the numerical ones. Following the maximum contour line (the red contour) to where it crosses the radial boundary, a slight discrepancy is noticeable between the analytic and numerical cases for $f^*_{\text{ext}} = 100$ Hz and $f^*_{\text{ext}} = 1000$ Hz. The $f^*_{\text{ext}} = 4000$ Hz case has a larger discrepancy. This, however, is still not obvious, but there is stretching of the contour lines near the radial boundary. The real difference tends to be in the drop off in the magnitude of the maximum azimuthal force as the frequency increases. Table 3.2 highlights this trend. The maximum lab azimuthal force agrees well with the analytic azimuthal force for low frequencies, within a percent up to $f^*_{\text{ext}} = 100$ Hz and undershooting by only 2.28% at $f^*_{\text{ext}} = 1000$ Hz. The lab azimuthal force starts to deviate significantly once $f^*_{\text{ext}} \geq 2000$ Hz and is 29.4% lower

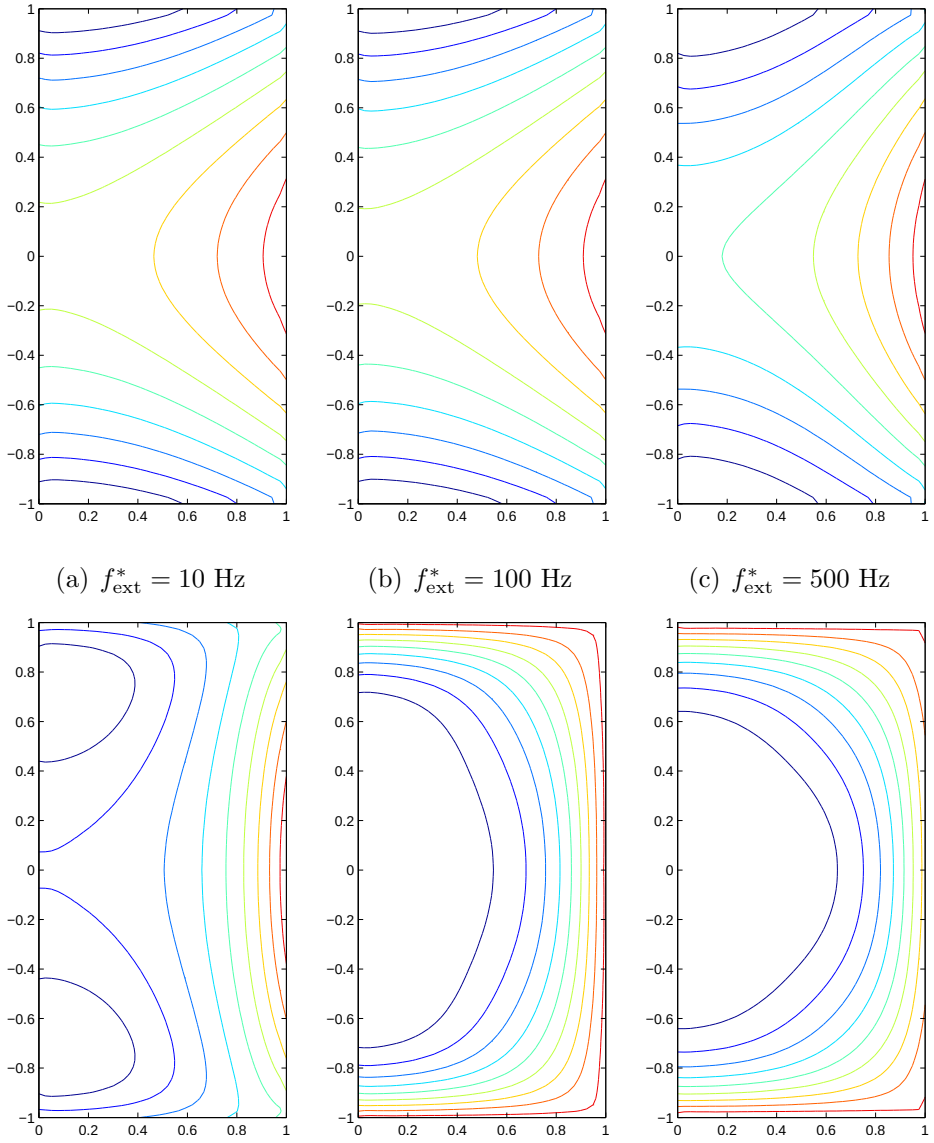

(a) $f^*_{\text{ext}} = 10$ Hz (b) $f^*_{\text{ext}} = 100$ Hz (c) $f^*_{\text{ext}} = 500$ Hz

(d) $f^*_{\text{ext}} = 1000$ Hz (e) $f^*_{\text{ext}} = 2000$ Hz (f) $f^*_{\text{ext}} = 4000$ Hz

Figure 3.8 : Contours of $\langle B^*_{\text{lab}} \rangle_{\overline{\theta}}$ at different frequencies when external coil current is held constant at 209.23 A. For comparison, the analytic B^* is constant throughout the melt. The contours are normalized such that the max is unity and the minimum is zero. The contours take steps of 0.1. For quantitative comparison, the maximum values $\langle B^*_{\text{lab}} \rangle_{\overline{\theta},\text{max}}$ are b) $B^*_{0,\text{lab}} = 2.77 \times 10^{-4}$ T, d) $B^*_{0,\text{lab}} = 2.77 \times 10^{-4}$ T, and f) $B^*_{0,\text{lab}} = 2.87 \times 10^{-4}$ T.

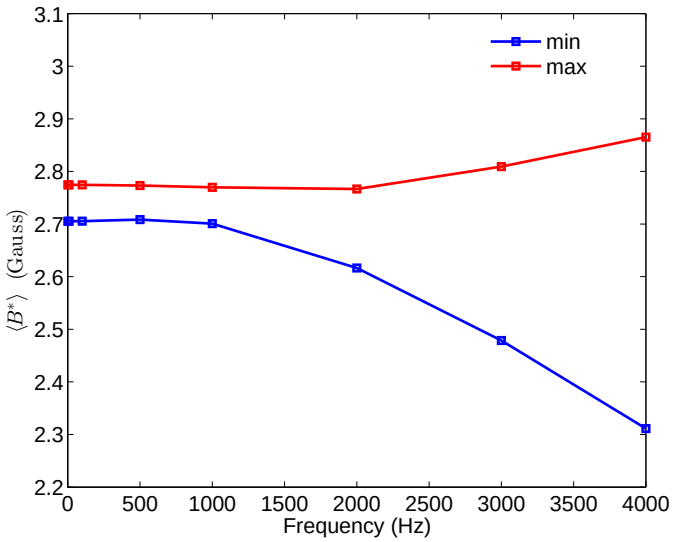

Figure 3.9 : $\langle B^*_{\rm lab} \rangle_{\bar{\theta},max} = B^*_{0,\rm lab}$ and $\langle B^*_{\rm lab} \rangle_{\bar{\theta},min}$ plotted against the frequency for the case when external coil current density is held constant at 209.23 A.

at $f^*_{\rm ext} = 5000$ Hz.

Again, magnetic shielding is the reason for such relatively low forces. The magnetic shielding affects the magnetic field, which affects the magnetic Taylor number. Because the Taylor number is calculated using the *maximum* of the time- and azimuthally-averaged magnetic flux density and magnetic shielding causes a greater variation in $\langle \mathbf{B}^*_{\rm lab} \rangle$, the Taylor number is higher than if the complete space-time-average were used. Additionally, the numerical solution creates forces in the radial and axial directions. This means that some of the electromagnetic energy that is theoretically completely transferred to the azimuthal flow energy is actually adding to the axial and radial directions, thereby decreasing that energy in the azimuthal direction.

These forces in the non-azimuthal direction are also tabulated in Table 3.2. The analytic force is purely azimuthal, but the numerical force has significant radial and

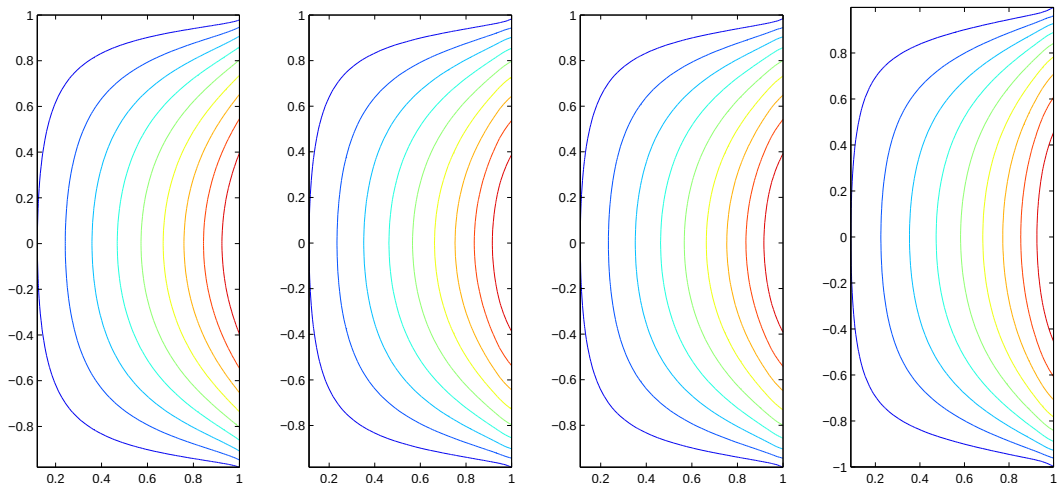

(a) Analytic (b) $f^*_{\text{ext}} = 100$ Hz (c) $f^*_{\text{ext}} = 1000$ Hz (d) $f^*_{\text{ext}} = 4000$ Hz

Figure 3.10 : The analytic azimuthal force contours compared with the lab azimuthal force at several frequencies. The forces are normalized such that the max is unity and the minimum is zero. The contours take steps of 0.1. The Taylor numbers are b) $Ta_m = 3.25 \times 10^3$, c) $Ta_m = 3.24 \times 10^4$, and d) $Ta_m = 1.39 \times 10^5$. The total current in each solenoid for the Opera simulations was 209.23 A.

axial forces. They are relatively small compared to the azimuthal force up to $f^*_{\text{ext}} =$ 100 Hz, where the azimuthal force is two orders of magnitude greater. At $f^*_{\text{ext}} =$ 1000 Hz, the azimuthal force is still approximately an order of magnitude greater than the other forces, but the axial and radial forces reach the same order as the frequency increases.

The additional force components are significant in that they are more physical so are of importance to experimentalists and because theory assumes them to be zero. In later sections, we see how the difference in numerical forces and the analytic force give different stability results.

Figure 3.11 shows the comparison of the normalized force contours in the radial and axial directions for low and high frequencies $f^*_{\text{ext}} = 100$ Hz and $f^*_{\text{ext}} = 4000$ Hz, respectively. It is easy to see that the radial force moves outward toward the radial

Table 3.2 : Summary of how the maximum nondimensional forces change with frequency and how the nondimensional lab azimuthal force compares to the analytic azimuthal force. The current in each solenoid was held constant at 209.23 A.

f^*_{ext} (Hz)	Ta_m	R_ω	$\langle F_{\text{lab},r}\rangle_{\max}$	$\langle F_{\text{lab},z}\rangle_{\max}$	$\langle F_{\text{lab},\theta}\rangle_{\max}$	analytic EM force for a finite cylinder $\langle F_{\text{EM},\theta}\rangle_{\max}\Big\vert_{R_\omega \ll 1}$	% undershoot of $\langle F_{\text{lab},\theta}\rangle_{\max}$ compared to the analytic EM force
1	3.25×10^1	0.00121	9.85×10^{-3}	1.29×10^{-2}	2.39×10^1	2.40×10^1	0.60
10	3.25×10^2	0.0121	4.46×10^{-1}	5.73×10^{-1}	2.39×10^2	2.40×10^2	0.60
100	3.25×10^3	0.121	4.21×10^1	5.67×10^1	2.39×10^3	2.40×10^3	0.62
500	1.62×10^4	0.606	1.04×10^3	1.41×10^3	1.19×10^4	1.20×10^4	1.03
1000	3.24×10^4	1.21	4.09×10^3	5.54×10^3	2.34×10^4	2.40×10^4	2.28
2000	6.46×10^4	2.43	1.54×10^4	2.08×10^4	4.42×10^4	4.78×10^4	7.66
3000	1.00×10^5	3.64	3.15×10^4	4.24×10^4	6.06×10^4	7.40×10^4	18.1
4000	1.39×10^5	4.85	4.97×10^4	6.67×10^4	7.25×10^4	1.03×10^5	29.4

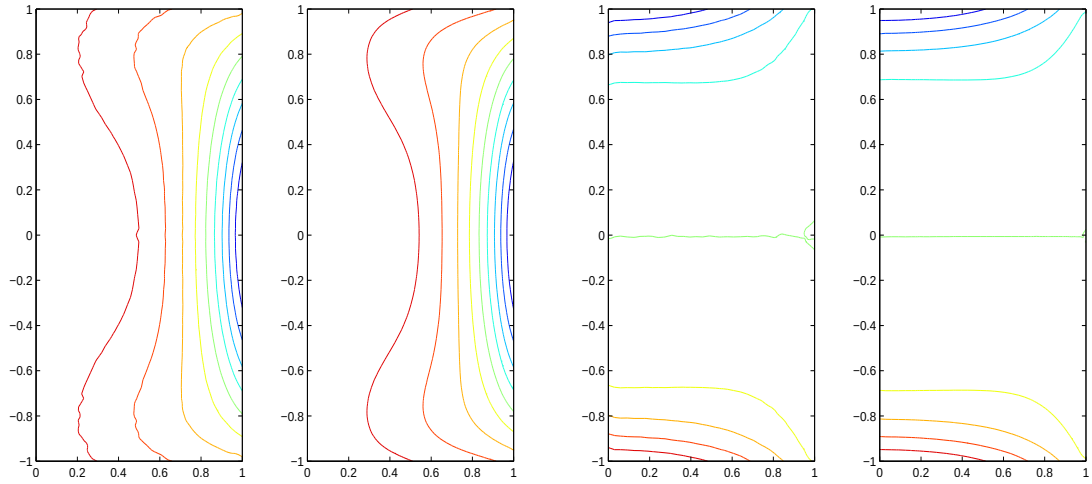

(a) $F_{\text{lab},r}$ $f^*_{\text{ext}} = 100$ Hz

(b) $F_{\text{lab},r}$ $f^*_{\text{ext}} = 4000$ Hz

(c) $F_{\text{lab},z}$ $f^*_{\text{ext}} = 100$ Hz

(d) $F_{\text{lab},z}$ $f^*_{\text{ext}} = 4000$ Hz

Figure 3.11 : Lab radial and axial time-averaged forces at $f^*_{\text{ext}} = 100$ Hz and $f^*_{\text{ext}} = 4000$ Hz. The forces are normalized so that the maximum is one and the minimum is zero. Steps are taken in increments of 0.1. The maximum nondimensional values are a) $F_{\text{lab},r,max} = 4.21 \times 10^1$, b) $F_{\text{lab},r,max} = 4.97 \times 10^4$, c) $F_{\text{lab},z,max} = 5.67 \times 10^1$, and d) $F_{\text{lab},z,max} = 6.67 \times 10^4$.

surface as the frequency goes up, but the pattern remains similar. The axial force shows much less noticeable change from low to high frequency. As in the radial forces, the axial forces are being pushed outward radially, but the change is much less substantial. Again, the maximum values associated with each force can be found in Table 3.2.

3.3 Flow Solutions for RMF Stirring

The equations of fluid flow are solved using a freely available code called Semtex [23]. Semtex is a solver for general fluid flow and advection-diffusion problems for geometries that are arbitrary in two dimensions but periodic in the other. This includes flows confined to a cylinder. The method works by using spectral elements

[42] in two dimensions and then extending into the third direction via Fourier modes. It allows standard expansion functions to be used in all elements (even those at the axis in cylinders) while maintaining the property of exponential three-dimensional spatial convergence.

The method projects the velocity exactly onto a set of two-dimensional complex Fourier modes

$$\hat{\mathbf{v}}_m(r,z,t) = \frac{1}{2\pi}\int_0^{2\pi} \mathbf{v}(r,\theta,z,t)e^{-im\theta}\,d\theta \tag{3.18}$$

which can be reconstructed in a Fourier series to recover the velocity field

$$\mathbf{v}(r,\theta,z,t) = \sum_{m=0}^{n_m} \hat{\mathbf{v}}_m(r,z,t)e^{im\theta} \tag{3.19}$$

where m is an integer wavenumber. Details of the methods used in Semtex can be found in the paper describing the formulation by Blackburn and Sherwin [23].

The Lorentz forces obtained from Opera are used as input in Semtex. The axisymmetric forces are contained in a single file that is read into Semtex and applied to the flow equations. Initially, the forces are increased linearly between nondimensional $t = 0$ and $t = 1$ such that the forces applied at a given time are $\mathbf{f}(t) = t\mathbf{f}_{\text{input}}$. When $t \geq 1$, the forces are held constant in time at the values in the input force file.

All simulations were run using the same mesh for the r-z plane, shown in Figure 3.12. The interpolation order for each element was set to 8, placing the first node a distance of 0.002506 from the boundary and yielding a maximum value of $y^+ = 0.420$ over all boundaries for the $Ta = 1.65 \times 10^5$ axisymmetric run. A brief refinement study can be found in Appendix A, validating this choice of interpolation order. The time step was set to $\Delta t = 1 \times 10^{-5}$ for all cases and proved to be stable throughout each simulation. This yielded a CFL number that was less than 0.012 for all simulations. A brief study on the temporal stability can be found in Appendix A.

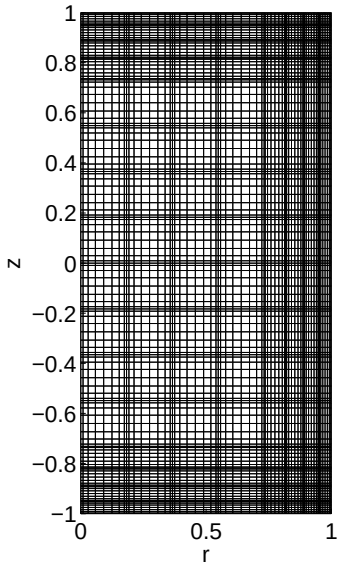

Figure 3.12 : The mesh in the r-z plane for each simulation consisting of 8×16 8th–order elements, for a total of 8385 unique nodes.

Axisymmetric runs used only the r-z plane while three-dimensional runs used 8 planes in the azimuthal direction to simulate modes 0–3. Also, all three-dimensional cases were restarted from a perturbed steady axisymmetric run. That is, for the same applied body force (ramped appropriately), an axisymmetric simulation was performed until a steady state was reached. This solution was then copied onto the eight azimuthal planes and used as the base state. Then, in an effort to introduce energy to modes other than $m = 0$, the base state was perturbed using a Gaussian distribution with a standard deviation of 0.1% of the maximum azimuthal velocity.

Flow fields were visualized using Paraview 3.98 [43] and analyzed with the built-in options in Paraview, the tools provided with Semtex, and the output files Semtex generates. Streamlines and contours were plotted in Paraview to determine features of the instabilities and to compare perturbations to linear stability theory.

3.4 Comparison of Steady, Axisymmetric Base Flows Driven by Analytic versus Laboratory EM Body Forces

Steady, axisymmetric, RMF driven base flows were computed using both the analytic EM body force and the lab body force from Opera simulations. These flows are compared at equivalent magnetic Taylor numbers, Ta_m. First, the procedure for setting the electric current in the lab coils to produce a desired Taylor number in the melt is described in Section 3.4.1. Then, for a fixed coil current, the impact of driving frequency f^*_{ext} is explored on the base flow for both analytic and lab EM body forces in Section 3.4.2. Next, Ta_m is held constant at 10,000 while f^*_{ext} is varied in Section 3.4.3. This chapter concludes with the study of axisymmetric and three-dimensional instabilities to the base flow in Sections 3.5 and 3.6, respectively.

3.4.1 Obtaining a Desired Magnetic Taylor Number at a Given Frequency

It is desirable to control the magnetic Taylor number for a given frequency for most lab simulations studied here. The strength of the magnetic field is controlled by the the amount of current running through the six coils and is approximately constant until magnetic shielding becomes too great. This is shown for the first set of tests discussed later in Subsection 3.4.2, Table 3.3.

For now, the problem of determining the appropriate current density for a given magnetic Taylor number and frequency is considered. The magnetic Taylor number for the lab RMF is defined as

$$Ta_m = \frac{\sigma^* \omega^*_{\text{ext}} B^{*2}_{0,\text{lab}} L^{*4}_0}{2\rho^* \nu^{*2}},$$

where $B^*_{0,\text{lab}} = \langle B^*_{\text{lab}} \rangle_{\overline{\theta},\max}$. The electromagnetic theory of AC coils yields a relation-

ship between the magnetic flux density and the current density such that

$$B^*_{0,\text{ext}} = C^*_j J^*_{coil}, \tag{3.20}$$

where J^*_{coil} is the total current running through each of the six coils and C^*_j is a constant that depends only on geometry. If magnetic shielding were non-existent, then the external magnetic field would fully penetrate the melt such that $B^*_{0,\text{lab}}\Big|_{R_\omega \ll 1} = B^*_{0,\text{ext}}$. Using this and substituting the known linear relationship between the magnetic flux density and current gives

$$Ta_m\Big|_{R_\omega \ll 1} = \frac{\sigma^* \omega^*_{\text{ext}} B^{*2}_{0,\text{ext}} L^{*4}_0}{2\rho^* \nu^{*2}} = \frac{\sigma^* 2\pi f^*_{\text{ext}} C^{*2}_j J^{*2}_{coil} L^{*4}_0}{2\rho^* \nu^{*2}}$$

$$\Rightarrow \quad J^*_{coil}\Big|_{R_\omega \ll 1} = \sqrt{\frac{\rho^* \nu^{*2}\, Ta_m}{\sigma^* \pi f^*_{\text{ext}} C^{*2}_j L^{*4}_0}}. \tag{3.21}$$

The value of C^*_j can be determined by theory or a by single simulation at any frequency and any fixed current in the coils. However, the assumption of negligible magnetic shielding is only good for low frequencies.

To account for shielding at higher frequencies, the magnetic flux density *in the melt* must be a function of frequency as well as current density. This effect is included by letting C^*_j be a function of frequency such that

$$B^*_{0,\text{lab}} = C_j(f^*_{\text{ext}}) J^*_{coil}. \tag{3.22}$$

Again, the substitution is made and the current can be expressed as

$$J^*_{coil} = \sqrt{\frac{\rho^* \nu^{*2}\, Ta_m}{\sigma^* \pi f^*_{\text{ext}} C_j(f^*_{\text{ext}})^{*2} L^{*4}_0}} = C_f(f^*_{\text{ext}})\, Ta_m^{\frac{1}{2}} \tag{3.23}$$

where all of the constant properties and the frequency are lumped into one term $C_f(f^*_{\text{ext}})$ that depends only on frequency. Now a single simulation at a particular frequency and any current determines the value of $C_f(f^*_{\text{ext}})$ for that frequency. Figure 3.13 shows the values for $C_f\sqrt{f^*_{\text{ext}}}$ found through simulations with and without

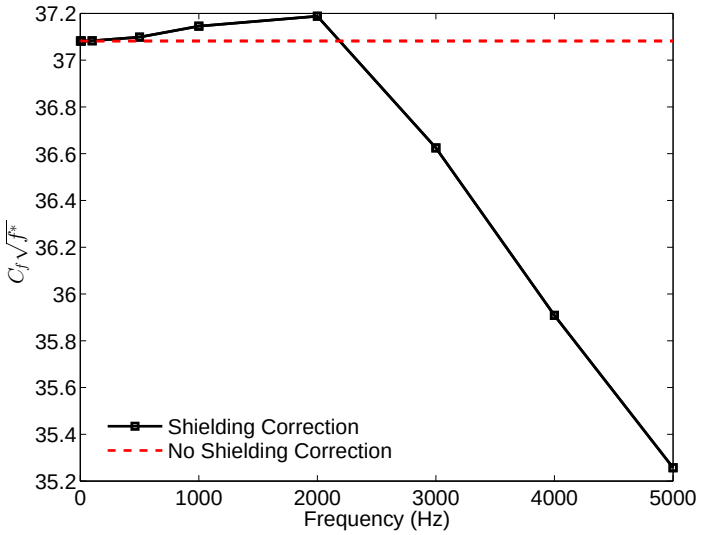

Figure 3.13 : The value of $C_f\sqrt{f^*_{\text{ext}}}$ vs frequency with and without the correction for magnetic shielding.

the correction for magnetic shielding. Without the correction, this value is a constant and is good at low frequencies as expected. However, as the figure shows, the lines begin to deviate significantly as higher frequencies are reached. This method for obtaining a desired magnetic Taylor number at a particular frequency proved to be quite accurate. The greatest % error in the cases where the Taylor number was targeted to be held constant at $Ta_m = 1.20 \times 10^5$ (but the frequency varied) was $3.4 \times 10^{-5}\%$, corresponding to an actual Taylor number of $Ta_m = 119,999.96$.

3.4.2 Constant External Current Density, Variable Frequency

The first set of tests consisted of holding the current running through each coil constant at 209.23 Amps while varying the frequency. This current was selected to set $Ta_m = 1.00 \times 10^5$ at $f^*_{\text{ext}} = 3000$ Hz. This is slightly below the critical magnetic Taylor number $Ta^{cr}_{m_{\text{analytic}}} = 1.232 \times 10^5$ predicted by linear stability analysis for flow driven by the analytic RMF body force [21]. With this choice of current, only the

$f^*_{\text{ext}} = 4000$ Hz case has a Ta_m greater than $Ta^{cr}_{m_{\text{analytic}}}$. The resultant Lorentz forces for this case were summarized in Table 3.2 and showed significant deviation as the shielding parameter increased. Here, the effect of the discrepancies in the lab forces on the base flow is investigated. Additionally, the effects of frequency on parameters such as $B^*_{0,\text{lab}}$, Ta_m, the maximum velocities, and the shielding parameter are analyzed.

Table 3.3 shows how the frequency affects the various electromagnetic parameters. The characteristic magnetic flux density $B^*_{0,\text{lab}}$ changes very little until the frequency reaches 3000 Hz, at which point it begins to rise. This is due to the magnetic shielding effect, most accurately indicated by the magnetic skin depth δ^*_m. The magnetic skin depth gives the distance radially inside the cylinder's surface where the magnetic field penetrates before being significantly distorted.

Table 3.3 : AC-frequency related quantities of the GaInSb cylindrical melt (calculations based on melt properties in Table 3.1) and melt radius $R^* = 0.01275$ m for a constant external coil current of 209.23 A.

f^*_{ext} (Hz)	$B^*_{0,\text{lab}} \times 10^4$ (T)	Ta_m	R_ω	δ^*_m (m)	$\delta_m = \sqrt{\frac{2}{R_\omega}}$
1	2.77	3.25×10^1	1.21×10^{-3}	5.18×10^{-1}	40.61
10	2.77	3.25×10^2	1.21×10^{-2}	1.64×10^{-1}	12.84
100	2.77	3.25×10^3	1.21×10^{-1}	5.18×10^{-2}	4.061
500	2.77	1.62×10^4	6.06×10^{-1}	2.32×10^{-2}	1.816
1000	2.77	3.24×10^4	1.21	1.64×10^{-2}	1.284
2000	2.77	6.46×10^4	2.43	1.16×10^{-2}	0.908
3000	2.81	1.00×10^5	3.64	9.45×10^{-3}	0.741
4000	2.87	1.39×10^5	4.85	8.19×10^{-3}	0.642

For a radius of $R^* = 0.01275$ m, the magnetic field is able to penetrate the entire cylinder for frequencies up to and including $f^*_{\text{ext}} = 1000$ Hz. At $f^*_{\text{ext}} = 2000$ Hz there is minimal shielding, with δ^*_m just slightly thinner than R^*. The nondimensional skin depth shows this most readily, with $\delta_m < 1$ for $f^*_{\text{ext}} \geq 2000$ Hz. At $f^*_{\text{ext}} = 3000$ Hz, the same frequency where a change in $B^*_{0,\text{lab}}$ is evident, the dimensional skin depth is significantly thinner than R^* and $\delta_m = 0.741$.

Figures 3.14 – 3.17 show the contours of the nondimensional base flow velocities and pressure for the cases using the analytic force (top) and the numerical lab force (bottom) to drive the flow. It should be noted that the analytic case is based on the low frequency approximation so there is not actually a frequency involved in the computation. Instead, the magnetic Taylor numbers are matched to those in the lab setup and the equivalent frequency f^*_{eq} is used to signify this. That is, f^*_{eq} is defined as the equivalent frequency (for a given coil current) at which the numerical lab forces give the magnetic Taylor number that is used in the analytically-forced flow computations.

These contours demonstrate how the flow develops as the frequency is increased. As the frequency increases, the flow is pushed towards the boundaries and boundary layers start to form. This is easy to see as v_r thins at the axial boundaries, v_z thins at the radial boundary, and v_θ thins at both axial and radial boundaries.

The shape of the contours of the analytically-forced base flow closely mimics that of the numerically-forced lab base flow. The quantitative comparison is also quite good up to $f^*_{\text{ext}} = f^*_{\text{eq}} = 1000$ Hz. At $f^*_{\text{ext}} = f^*_{\text{eq}} = 4000$ Hz, the contours are still qualitatively similar, though quantitatively they have deviated significantly. This quantitative divergence begins by $f^*_{\text{ext}} = f^*_{\text{eq}} = 2000$ Hz where shielding begins to play a role in the lab EM body force field.

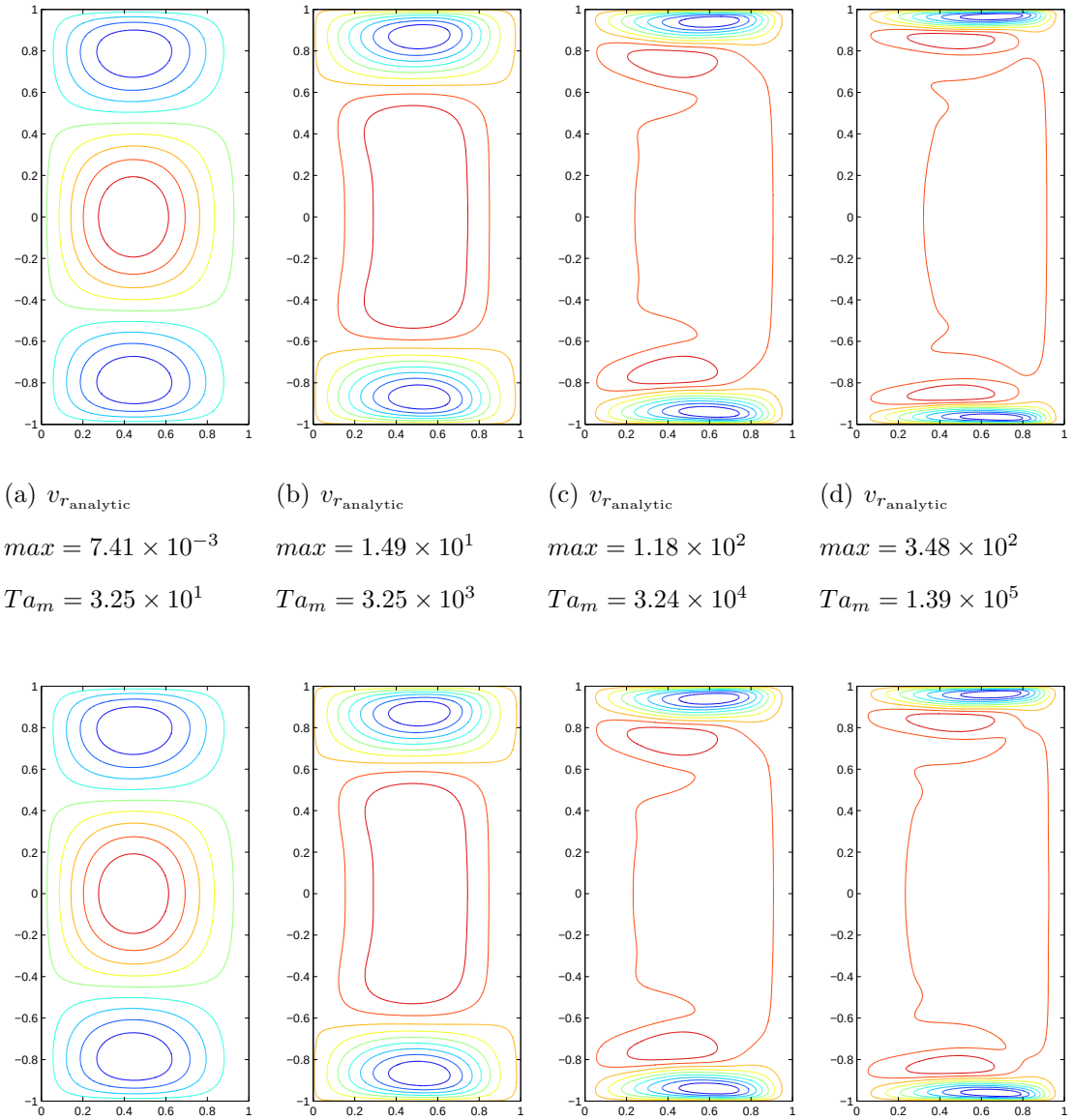

(a) $v_{r_{\text{analytic}}}$
$max = 7.41 \times 10^{-3}$
$Ta_m = 3.25 \times 10^1$

(b) $v_{r_{\text{analytic}}}$
$max = 1.49 \times 10^1$
$Ta_m = 3.25 \times 10^3$

(c) $v_{r_{\text{analytic}}}$
$max = 1.18 \times 10^2$
$Ta_m = 3.24 \times 10^4$

(d) $v_{r_{\text{analytic}}}$
$max = 3.48 \times 10^2$
$Ta_m = 1.39 \times 10^5$

(e) $v_{\text{lab},r}$
$max = 7.43 \times 10^{-3}$
$f^*_{\text{ext}} = 1$ Hz
$Ta_m = 3.25 \times 10^1$

(f) $v_{\text{lab},r}$
$max = 1.48 \times 10^1$
$f^*_{\text{ext}} = 100$ Hz
$Ta_m = 3.25 \times 10^3$

(g) $v_{\text{lab},r}$
$max = 1.15 \times 10^2$
$f^*_{\text{ext}} = 1000$ Hz
$Ta_m = 3.24 \times 10^4$

(h) $v_{\text{lab},r}$
$max = 2.62 \times 10^2$
$f^*_{\text{ext}} = 4000$ Hz
$Ta_m = 1.39 \times 10^5$

Figure 3.14 : The nondimensional base flow radial velocity contours using analytic (a-d) and numerical (e-h) forces at various frequencies. All fields shown are normalized such that the minimum is zero and the maximum is one. Contour steps are taken in increments of 0.1. The maximum nondimensional values are given below each figure.

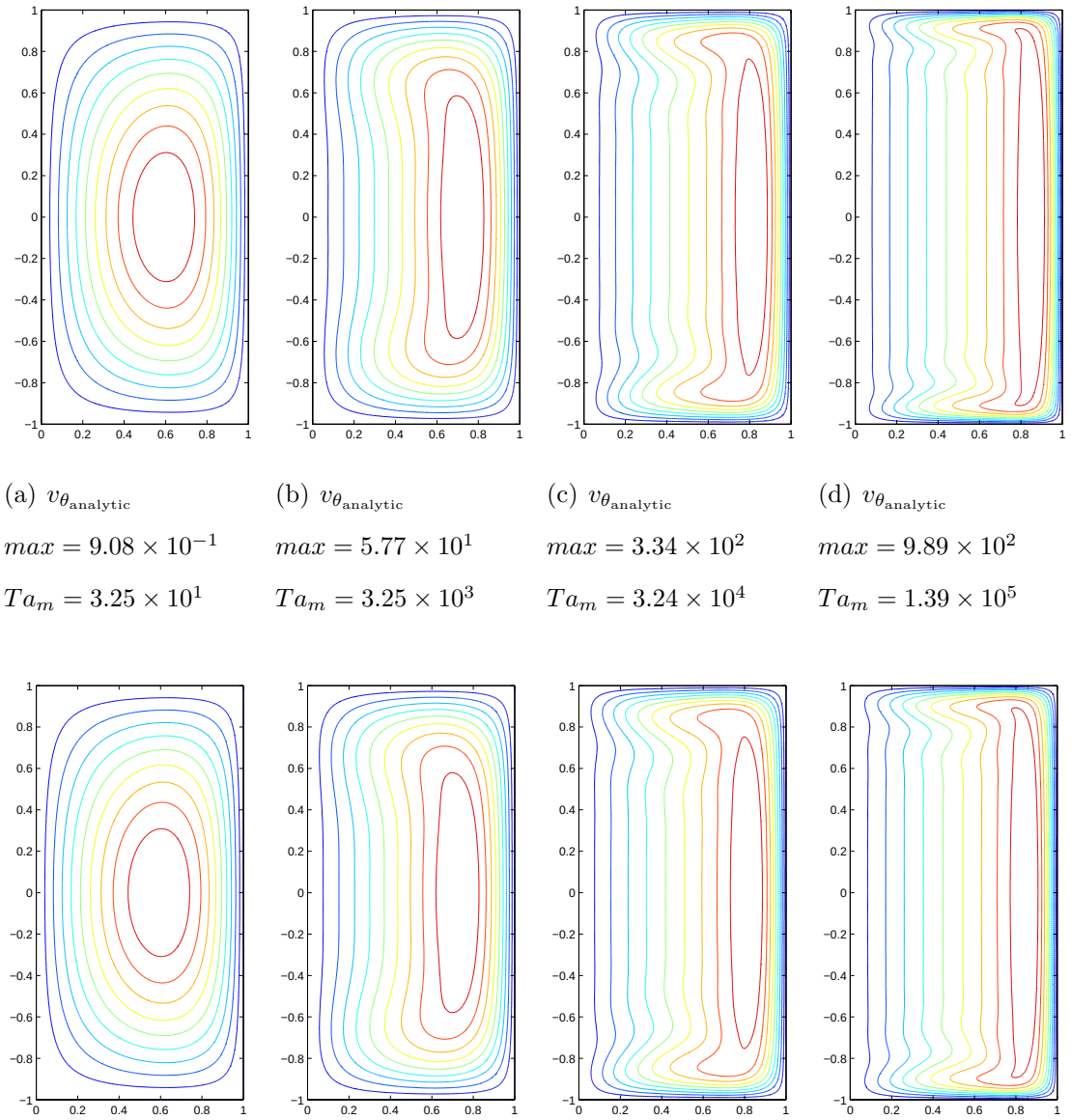

(a) $v_{\theta_{\text{analytic}}}$
$max = 9.08 \times 10^{-1}$
$Ta_m = 3.25 \times 10^1$

(b) $v_{\theta_{\text{analytic}}}$
$max = 5.77 \times 10^1$
$Ta_m = 3.25 \times 10^3$

(c) $v_{\theta_{\text{analytic}}}$
$max = 3.34 \times 10^2$
$Ta_m = 3.24 \times 10^4$

(d) $v_{\theta_{\text{analytic}}}$
$max = 9.89 \times 10^2$
$Ta_m = 1.39 \times 10^5$

(e) $v_{\text{lab},\theta}$
$max = 9.06 \times 10^{-1}$
$f^*_{\text{ext}} = 1$ Hz
$Ta_m = 3.25 \times 10^1$

(f) $v_{\text{lab},\theta}$
$max = 5.74 \times 10^1$
$f^*_{\text{ext}} = 100$ Hz
$Ta_m = 3.25 \times 10^3$

(g) $v_{\text{lab},\theta}$
$max = 3.27 \times 10^2$
$f^*_{\text{ext}} = 1000$ Hz
$Ta_m = 3.24 \times 10^4$

(h) $v_{\text{lab},\theta}$
$max = 7.54 \times 10^2$
$f^*_{\text{ext}} = 4000$ Hz
$Ta_m = 1.39 \times 10^5$

Figure 3.15 : The nondimensional base flow azimuthal velocity contours using analytic (a-d) and numerical lab (e-h) forces at various frequencies. All fields shown are normalized such that the minimum is zero and the maximum is one. Contour steps are taken in increments of 0.1. The maximum nondimensional values are given below each figure.

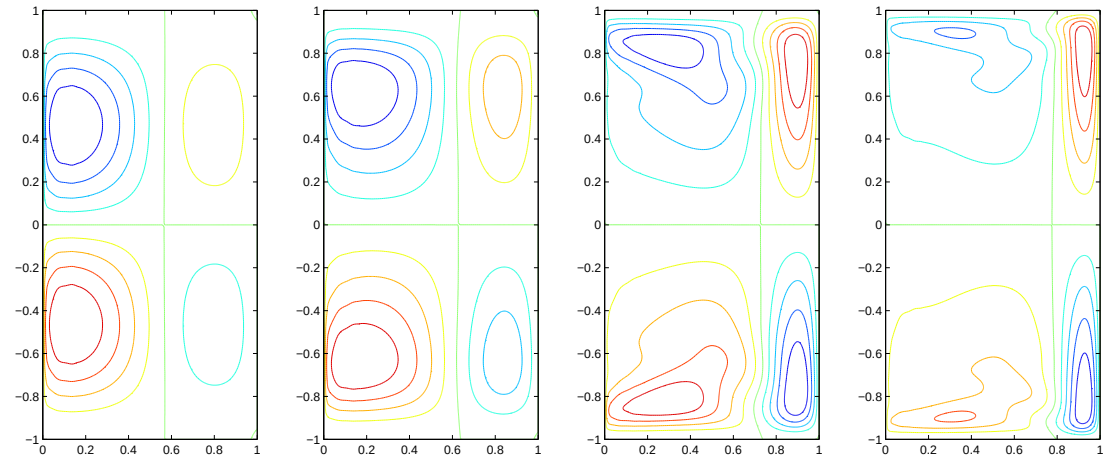

(a) $v_{z_{\text{analytic}}}$ $max = 1.43 \times 10^{-2}$ $Ta_m = 3.25 \times 10^1$

(b) $v_{z_{\text{analytic}}}$ $max = 1.75 \times 10^1$ $Ta_m = 3.25 \times 10^3$

(c) $v_{z_{\text{analytic}}}$ $max = 5.22 \times 10^1$ $Ta_m = 3.24 \times 10^4$

(d) $v_{z_{\text{analytic}}}$ $max = 1.31 \times 10^2$ $Ta_m = 1.39 \times 10^5$

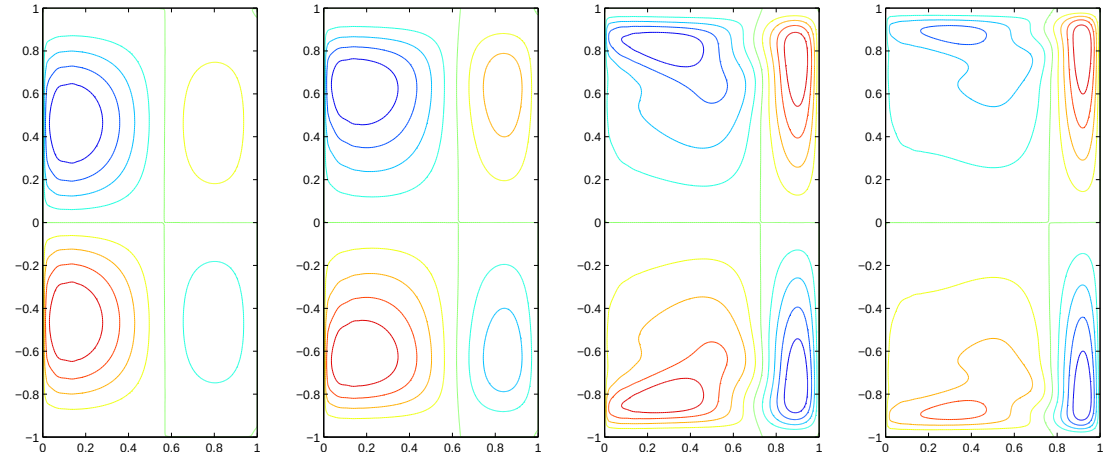

(e) $v_{\text{lab},z}$ $max = 1.43 \times 10^{-2}$ $f^*_{\text{ext}} = 1$ Hz $Ta_m = 3.25 \times 10^1$

(f) $v_{\text{lab},z}$ $max = 1.75 \times 10^1$ $f^*_{\text{ext}} = 100$ Hz $Ta_m = 3.25 \times 10^3$

(g) $v_{\text{lab},z}$ $max = 5.15 \times 10^1$ $f^*_{\text{ext}} = 1000$ Hz $Ta_m = 3.24 \times 10^4$

(h) $v_{\text{lab},z}$ $max = 1.02 \times 10^2$ $f^*_{\text{ext}} = 4000$ Hz $Ta_m = 1.39 \times 10^5$

Figure 3.16 : The nondimensional base flow axial velocity contours using analytic (a-d) and numerical lab (e-h) forces at various frequencies. All fields shown are normalized such that the minimum is zero and the maximum is one. Contour steps are taken in increments of 0.1. The maximum nondimensional values are given below each figure. e

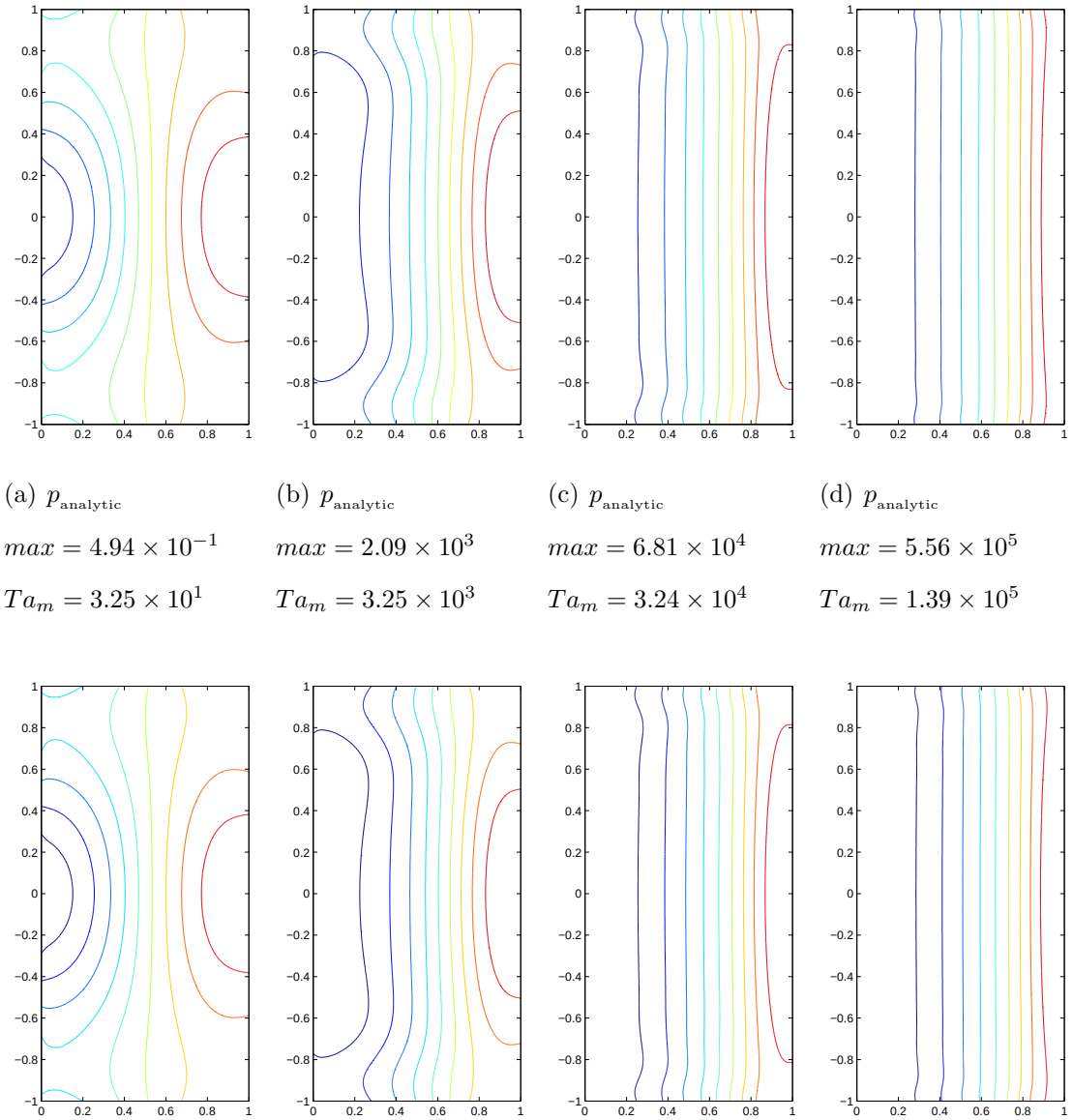

(a) p_{analytic}
$max = 4.94 \times 10^{-1}$
$Ta_m = 3.25 \times 10^1$

(b) p_{analytic}
$max = 2.09 \times 10^3$
$Ta_m = 3.25 \times 10^3$

(c) p_{analytic}
$max = 6.81 \times 10^4$
$Ta_m = 3.24 \times 10^4$

(d) p_{analytic}
$max = 5.56 \times 10^5$
$Ta_m = 1.39 \times 10^5$

(e) p_{lab}
$max = 4.89 \times 10^{-2}$
$f^*_{\text{ext}} = 1$ Hz
$Ta_m = 3.25 \times 10^1$

(f) p_{lab}
$max = 2.06 \times 10^3$
$f^*_{\text{ext}} = 100$ Hz
$Ta_m = 3.25 \times 10^3$

(g) p_{lab}
$max = 6.51 \times 10^4$
$f^*_{\text{ext}} = 1000$ Hz
$Ta_m = 3.24 \times 10^4$

(h) p_{lab}
$max = 3.18 \times 10^5$
$f^*_{\text{ext}} = 4000$ Hz
$Ta_m = 1.39 \times 10^5$

Figure 3.17 : The nondimensional base flow pressure contours using analytic (a-d) and numerical (e-h) forces at various frequencies. All fields shown are normalized such that the minimum is zero and the maximum is one. Contour steps are taken in increments of 0.1. The maximum nondimensional values are given below each figure.

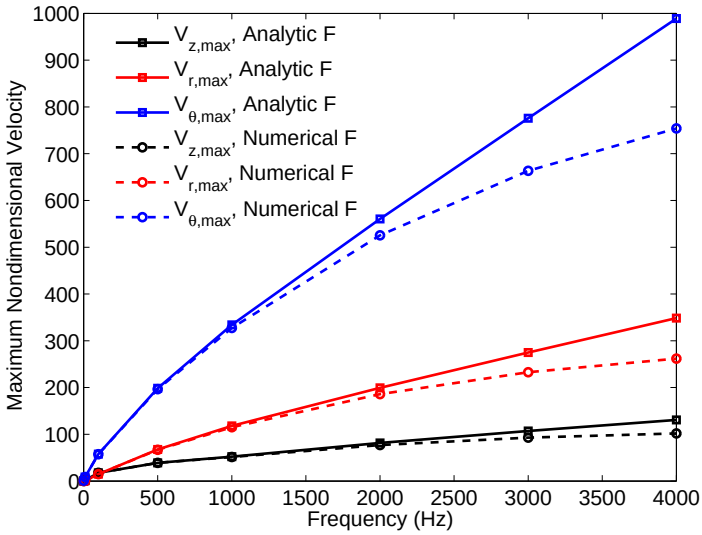

Figure 3.18 : The maximum nondimensional velocity components from the lab forces as a function of frequency compared to the maximum velocity components from the solution using the analytic forcing function. Note that the analytic solution used the magnetic Taylor number found in each numerical case since it does not depend on frequency.

Figure 3.18 shows how the maximum, nondimensional value of each lab velocity component varies as the frequency increases and how it compares to the maximum velocity components obtained from the simulation using the analytic forcing function. As expected, the agreement in all components is good for low frequencies when the numerical lab force nearly matches the analytic force, but begins to drop considerably as the frequency increases.

3.4.3 Base Flow at Constant $Ta_m = 1.0 \times 10^5$, Variable Frequency

The next set of tests consisted of holding the magnetic Taylor number constant at $Ta_m = 1.0 \times 10^5$ while varying the frequency. This required the accurate selection of the current density through the coils for the numerical lab setup in Opera as discussed in Subsection 3.4.1.

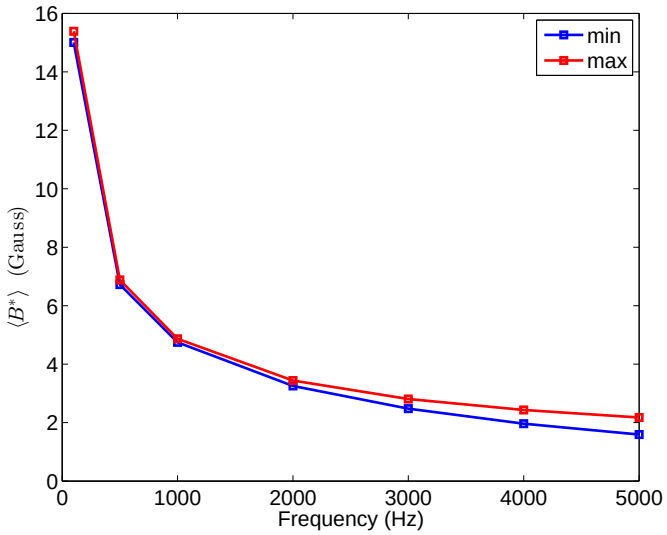

Figure 3.19 : The maximum $\langle B^*_{\text{lab}}\rangle_{\bar{\theta},max}$ and minimum $\langle B^*_{\text{lab}}\rangle_{\bar{\theta},min}$ time-averaged magnetic flux densities across the domain vs the frequency for $Ta_m = 1.0 \times 10^5$.

The values for the shielding parameter and magnetic skin depth from Table 3.3 are still valid here as they depend only on melt properties and the frequency. The frequency $f^* = 5000$ Hz has been added and its relevant values are $R_\omega = 6.06$, $\delta^*_m = 7.32 \times 10^{-3}$, and $\delta_m = 0.574$. The magnetic Taylor number is held constant here rather than the total current in the coils so the characteristic magnetic flux density has greater variation with frequency here as shown in Figure 3.19. The value of $\langle B^*_{\text{lab}}\rangle_{\bar{\theta},max}$ goes down as the frequency rises in order to counteract the frequency and keep the Taylor number constant. Figure 3.20 shows the total current running through the coils necessary to produce the desired Taylor number at each frequency. Since the relationship between the magnetic flux density and the current in the coils is nearly linear, only deviating from linearity at higher frequencies, the curve for the current is quite similar to that of the magnetic flux density.

Figures 3.21 - 3.24 show how the nondimensional base flow changes with increases in frequency for the analytically-forced solution and the numerically-forced lab solu-

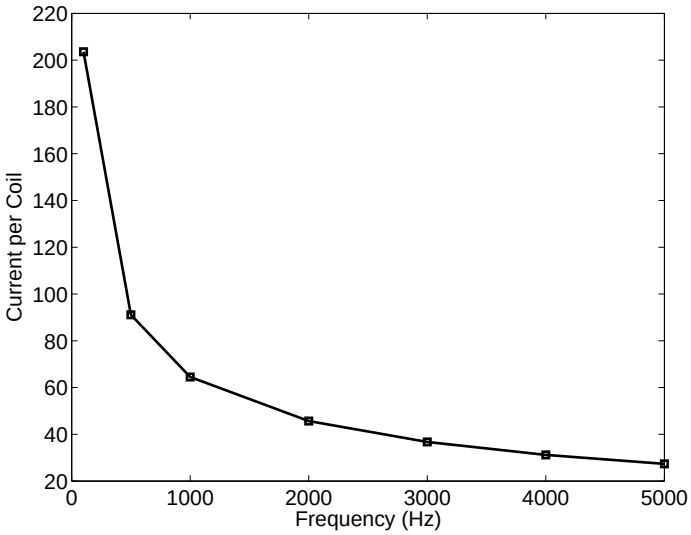

Figure 3.20 : The total current in amps applied in each coil vs the frequency to ensure $Ta_m = 1.0 \times 10^5$.

tion. Again, the low frequency approximation proves to be valid at low frequency and remains qualitatively valid even at frequencies with significant shielding, for all flow variables plotted. At $f^*_{\text{ext}} = 5000$ Hz, there is a noticeable, but small, qualitative change in the flow field variables. In particular, the azimuthal velocity, which dominates the flow field, is pushed slightly outward toward the periphery.

Finally, the values of the maximum, nondimensional velocity for each component, driven by the lab forces, are compared to those from the solution with analytic forces. Similar to the previous section, the values are in good agreement at low frequencies, but the values associated with the numerical lab forces begin to drop as the frequency increases. So, while the effects of frequency seem small when viewing the base flow shape, the magnitude of the velocities show significant differences. In Section 3.6, it will be evident that all of these differences between numerical lab-forced and analytical-forced flows have a significant impact on the physics of the instability.

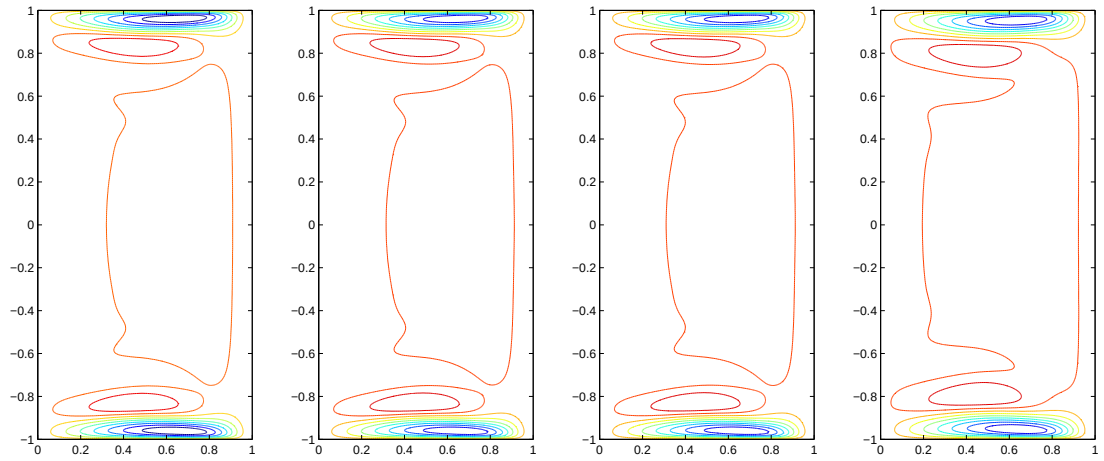

(a) $v_{r_{\text{analytic}}}$ $max = 2.75 \times 10^2$

(b) $v_{\text{lab},r}$, 100 Hz $max = 2.73 \times 10^2$

(c) $v_{\text{lab},r}$, 1000 Hz $max = 2.69 \times 10^2$

(d) $v_{\text{lab},r}$, 5000 Hz $max = 1.80 \times 10^2$

Figure 3.21 : The nondimensional, analytic base flow radial velocity contours compared to those found using numerical lab forces at various frequencies for $Ta_m = 1.0 \times 10^5$. All fields shown are normalized such that the minimum is zero and the maximum is one. Contour steps are taken in increments of 0.1. The maximum values are given below each figure.

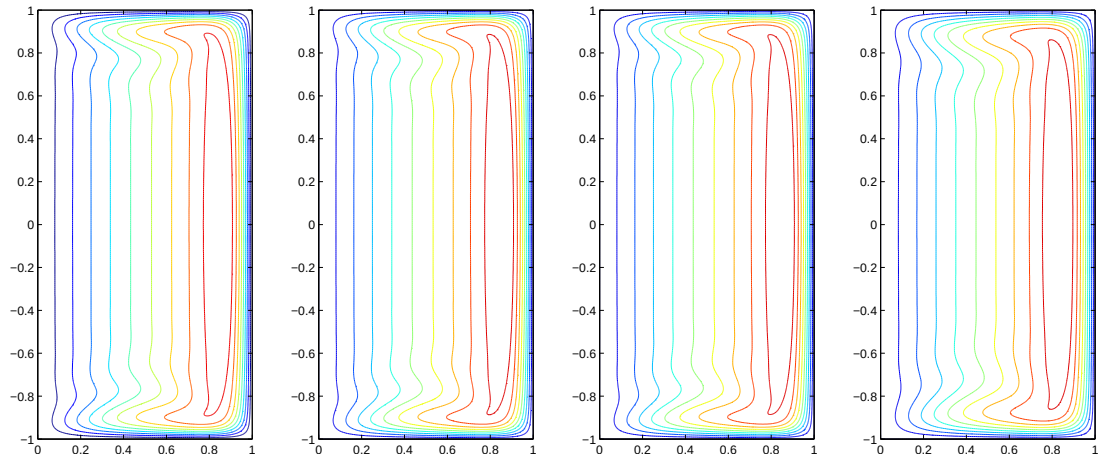

(a) $v_{\theta_{\text{analytic}}}$ $max = 7.76 \times 10^2$

(b) $v_{\text{lab},\theta}$, 100 Hz $max = 7.71 \times 10^2$

(c) $v_{\text{lab},\theta}$, 1000 Hz $max = 7.61 \times 10^2$

(d) $v_{\text{lab},\theta}$, 5000 Hz $max = 5.20 \times 10^2$

Figure 3.22 : The nondimensional, analytic base flow azimuthal velocity contours compared to those found using numerical lab forces at various frequencies for $Ta_m = 1.0 \times 10^5$. All fields shown are normalized such that the minimum is zero and the maximum is one. Contour steps are taken in increments of 0.1. The maximum values are given below each figure.

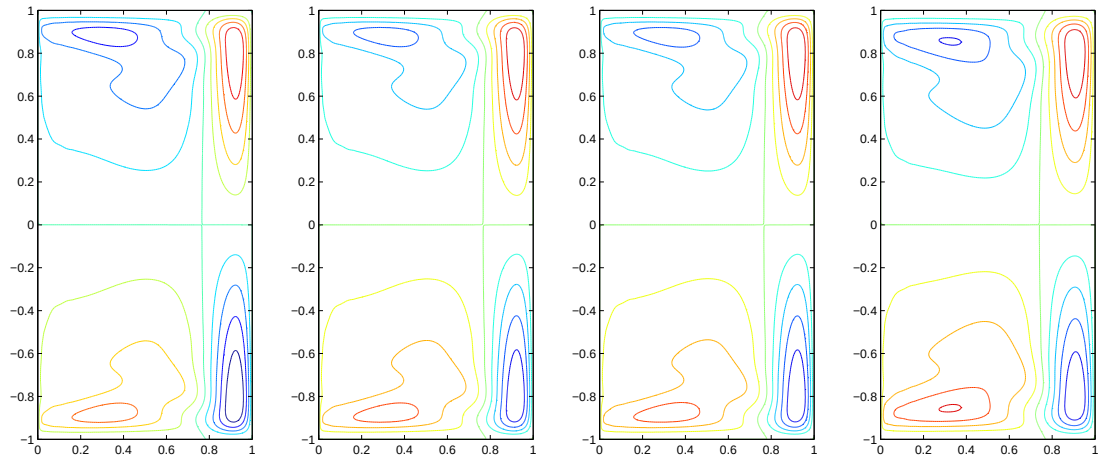

(a) $v_{z_{\text{analytic}}}$ (b) $v_{\text{lab},z}$, 100 Hz (c) $v_{\text{lab},z}$, 1000 Hz (d) $v_{\text{lab},z}$, 5000 Hz

$max = 1.07 \times 10^2$ $max = 1.07 \times 10^2$ $max = 1.06 \times 10^2$ $max = 7.39 \times 10^1$

Figure 3.23 : The nondimensional, analytic base flow axial velocity contours compared to those found using numerical lab forces at various frequencies for $Ta_m = 1.0 \times 10^5$. All fields shown are normalized such that the minimum is zero and the maximum is one. Contour steps are taken in increments of 0.1. The maximum values are given below each figure.

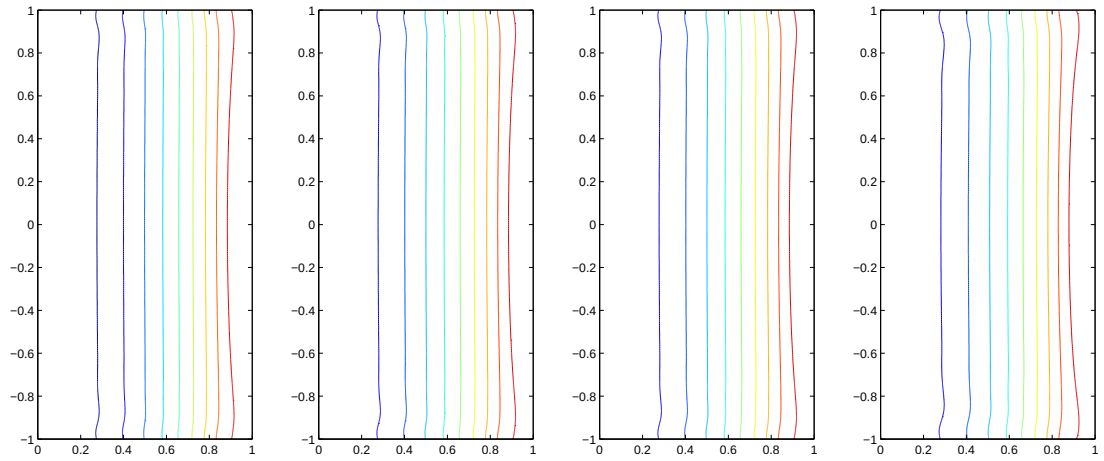

(a) p_{analytic} (b) p_{lab}, 100 Hz (c) p_{lab}, 1000 Hz (d) p_{lab}, 5000 Hz

$max = 3.48 \times 10^5$ $max = 3.42 \times 10^5$ $max = 3.33 \times 10^5$ $max = 1.53 \times 10^5$

Figure 3.24 : The nondimensional, analytic base flow pressure contours compared to those found using numerical lab forces at various frequencies for $Ta_m = 1.0 \times 10^5$. All fields shown are normalized such that the minimum is zero and the maximum is one. Contour steps are taken in increments of 0.1. The maximum values are given below each figure.

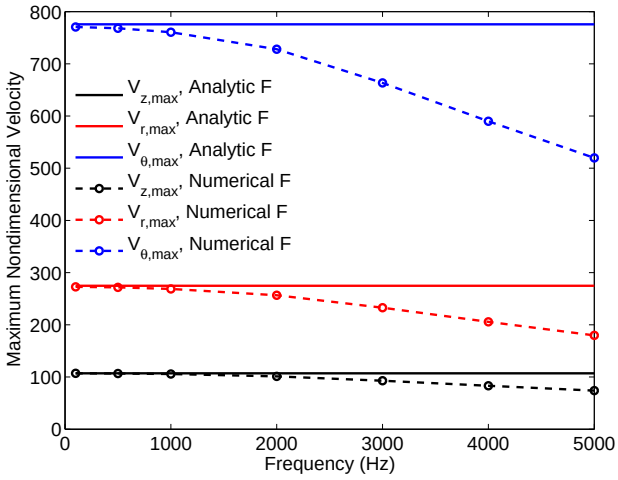

Figure 3.25 : The maximum nondimensional velocity components from the lab forces as a function of frequency compared to the maximum velocity components from the solution using the analytic forcing function.

3.5 Axisymmetric Instabilities in Flow Driven by the Analytic Body Force

Fully three-dimensional instabilities are more complicated and, in RMF driven flow, are dominant and therefore more physically meaningful. However, an initial investigation of axisymmetric instabilities with the analytic EM body force allows for efficient benchmarking of the flow field solver. Thus, in this section only axisymmetric instabilities are allowed.

Grants and Gerbeth [20] found that the initial point of instability for an $m = 0$ mode occurs at $Ta^{\mathrm{axi},cr}_{m_{\mathrm{l\text{-}s}}} = 1.636 \times 10^5$ according to linear stability theory, indicated by subscript 'l-s'. They also showed in another study that this $m = 0$ mode is not the dominant mode for the fully three-dimensional problem as the symmetric and antisymmetric $m = 1$ and $m = 2$ modes all present earlier [21]. Thus, the flow field must be constrained to axisymmetry by performing simulations with only the $m = 0$

mode contributing in order to investigate purely axisymmetric instabilities.

Via axisymmetric simulations in Semtex, the point of instability was bounded between $Ta^{\text{axi}}_{m_{\text{t-d, analytic}}}$ of 1.60×10^5 and 1.65×10^5 for the flow driven by the analytic RMF body force, where the subscript 't-d' indicates a time-dependent simulation, as opposed to a linear stability analysis. The growth of the instability was determined by monitoring the energy in the axisymmetric mode, defined as

$$E_0 = \frac{1}{2} \int_{-1}^{1} \int_{0}^{1} \mathbf{v}^\dagger \, \mathbf{v} \, r \, dr \, dz,$$

where $\mathbf{v}^\dagger$ is the complex conjugate of $\mathbf{v}$.

For the $m = 0$ mode, energy that levels out in time is stable while oscillatory behavior is indicative of the presence of a periodic instability. The energy for $Ta^{\text{axi}}_{m_{\text{t-d, analytic}}}$ at 1.60×10^5 and 1.65×10^5 is shown in Figure 3.26. The figure clearly shows steadiness at the lower Taylor number and oscillations at the higher one, thus bounding the critical magnetic Taylor as expected from the predictions of linear stability theory. Figure 3.26(a) demonstrates the initial linear ramping of the forces and the subsequent constant applied force as well as the nonlinear saturation of the unstable mode as it oscillates between energies $E_{0_{\text{analytic}}} = 3183.03$ and $E_{0_{\text{analytic}}} = 3547.46$. Figure 3.26(b) shows a close-up on the energy after nonlinear saturation for nearly 2.5 periods so that the oscillations are clearly viewable.

In addition to accurately predicting the critical magnetic Taylor number, comparisons can be made between the shape of the perturbations as well as the period of oscillation. Figure 3.27 shows the contours of the azimuthal velocity perturbations from time-dependent simulations compared to the those found in linear stability theory. Also included are the perturbation velocity streamlines in a plane compared to those from linear stability theory. To create the plots from the time-dependent simulations, the steady base state before onset of instability has been subtracted from

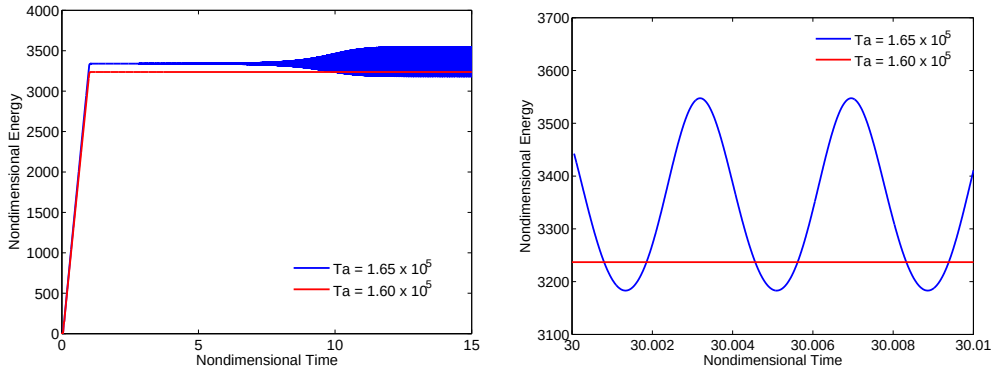

Figure 3.26 : Total nondimensional energy vs nondimensional time for $Ta^{\text{axi}}_{m_{\text{t-d, analytic}}}$ at 1.60×10^5 and 1.65×10^5 cases. The oscillations in the 1.65×10^5 case indicate an instability. The same plot is shown for a) 15 nondimensional time units from the beginning of the run and b) 0.01 nondimensional time units.

the perturbed flow. In each case, good agreement is seen.

Finally, the frequency of the oscillation can be compared to that found by Grants and Gerbeth [20]. At the critical point, they found the imaginary part of the eigenvalue to be $\xi^{\text{axi},cr}_{i_{\text{l-s}}} = 1659.1$, corresponding to a period of 0.003787 nondimensional time units. The period calculated in the present work at a Taylor number approximately 0.856% higher is 0.0037649 nondimensional time units. This corresponds to $\xi^{\text{axi}}_{\text{t-d, analytic}} = 2\pi/0.0037649 = 1668.9$, which is 0.591% higher than the frequency predicted by linear stability theory. These values appear to be in good agreement.

The good agreement in critical magnetic Taylor number, velocity perturbations and period of oscillation between linear stability theory and time-dependent, axisymmetric calculations validates the use of Semtex. With confidence in the ability to accurately simulate the flow, three-dimensional instabilities are now discussed.

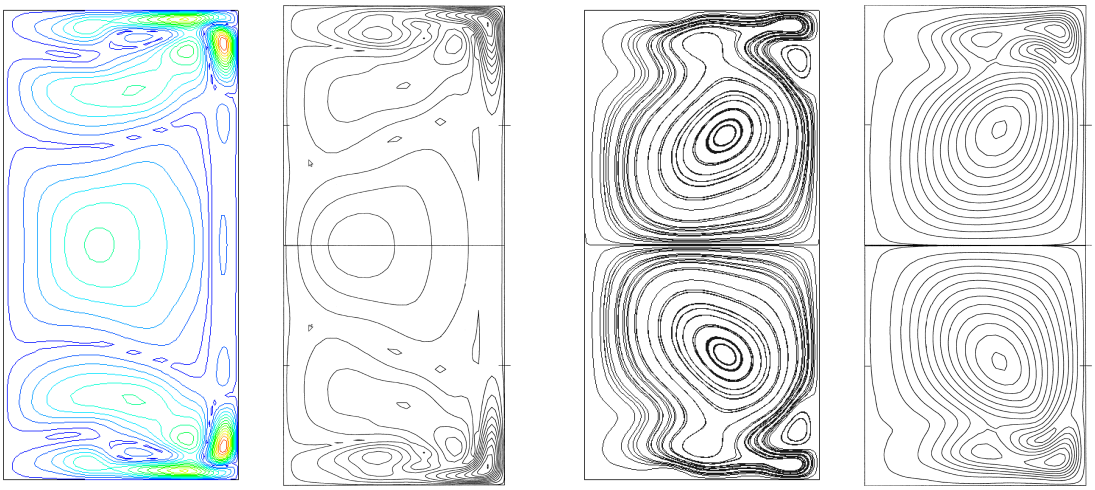

(a) time-dependent (b) linear stability (c) time-dependent (d) linear stability

Figure 3.27 : The magnitude of the azimuthal velocity perturbations from a) time-dependent simulations and b) linear stability theory [20]. Planar perturbation velocity streamlines from c) time-dependent simulations and d) linear stability theory [20]. The contours from the axisymmetric, time-dependent simulations are made by evenly spaced values between the minimum and maximum values.

3.6 Non-axisymmetric Instabilities in RMF Driven Flow

The approach to bounding the critical magnetic Taylor number for non-axisymmetric instabilities is the same as that taken for the axisymmetric instabilities. Again, linear stability theory predicts a critical magnetic Taylor value Ta_m^{cr}, which is used as a basis for selecting Taylor numbers simulation at which to carry out three-dimensional, time-dependent simulations. Grants and Gerbeth found that the critical Taylor number for a unit aspect ratio cylinder is $Ta_{m_{\text{l-s}}}^{cr} = 1.232 \times 10^5$ and presents as an $m = 2$ symmetric mode [21]. With this value in mind, $Ta_m = 1.20 \times 10^5$ and $Ta_m = 1.30 \times 10^5$ were selected for initial simulations, which were carried out using both the analytic body force and the lab body force.

The existence of an instability is found through monitoring the energy in each

mode after initially perturbing the flow randomly. The nondimensional energy in each mode m has the form

$$E_m = \frac{1}{2}\int_{-1}^{1}\int_{0}^{1} \hat{\mathbf{v}}_m^{\dagger}\,\hat{\mathbf{v}}_m\, r\, dr\, dz \tag{3.24}$$

where

$$\hat{\mathbf{v}}_m = \frac{1}{2\pi}\int_{0}^{2\pi} \mathbf{v} e^{-im\theta}\, d\theta \tag{3.25}$$

for modes $m = 0, 1, ..., n_m$. For the RMF simulations here, the highest order mode monitored is $n_m = 3$. The magnetic Taylor numbers associated with the three-dimensional, time-dependent simulations include subscript 't-d, analytic' or 't-d, lab' to indicated time-dependent simulations with either analytic or lab body forces.

3.6.1 Non-axisymmetric Instabilities Using the Analytic Body Force

In this subsection, the analytic body force (Equation 3.17), reproduced here as

$$\langle F_{\mathrm{EM},\theta}\rangle\Big|_{R_\omega \ll 1,\ \text{finite, analytic}} = r - 2\sum_{N=1}^{\infty} \frac{J_1(\zeta_N r)\cosh(\zeta_N z)}{(\zeta_N^2 - 1)J_1(\zeta_N)\cosh(b\,\zeta_N)},$$

is used to drive the flow and increases linearly with the Taylor number. Since this body force is the same one used for previous results from linear stability theory, it was expected that the critical magnetic Taylor number for three-dimensional, time-dependent simulations should be similar.

Once the axisymmetric base flow has been found, it is expanded onto eight planes in the azimuthal direction. This base flow is then perturbed randomly using a Gaussian distribution with a standard deviations of 0.1% of the maximum azimuthal velocity for all cases. Three-dimensional simulations use the perturbed base state as a starting point for the continued simulation.

The simulation for $Ta_{m_{\text{t-d, analytic}}} = 1.20 \times 10^5$ did prove to be stable as can be seen in Figure 3.28. The perturbation does initially cause instability in the flow, but the

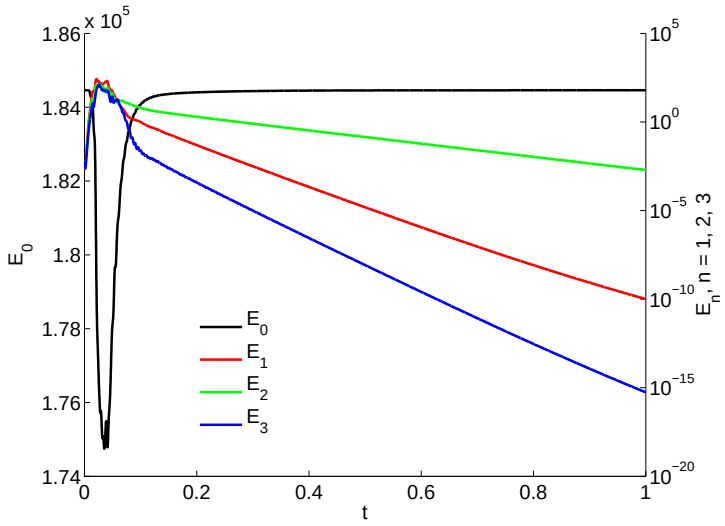

Figure 3.28 : Energy in modes $0-3$ in time for the $Ta_{m_{\text{t-d, analytic}}} = 1.20\times10^5$ simulation with the analytic body force. All modes with $m > 0$ decay in time, indicating stability.

immediate spikes in energy seen in modes 1–3 have nearly all returned to mode 0 by $t = 0.2$. The figure shows that the $m = 2$ mode is the slowest to decay, which is expected since it is the mode that is predicted to grow above the critical magnetic Taylor number. Similarly, the $m = 1$ mode has the next slowest rate of decay, also as predicted by linear stability theory.

Linear stability analysis suggests that, just above the critical magnetic Taylor number, the $m = 2$ mode grows while perturbations in other modes decay. As Figure 3.29(a) shows, for the $Ta_{m_{\text{t-d, analytic}}} = 1.30\times10^5$ simulation, after the initial "shake up" region ($0.0 < t < \sim 0.15$) the energy in modes 1 and 3 does appear to decay. The energy in the $m = 2$ mode begins to grow as expected. However, at approximately $t = 0.315$, the energy in modes 1–3 grows very abruptly and again there is another region characterized by stochastic behavior, which later settles down. Figure 3.29(b) indicates that this pattern of stochastic behavior followed by growth/decay in the $m = 2$ mode/all other modes continues for the duration of the simulation.

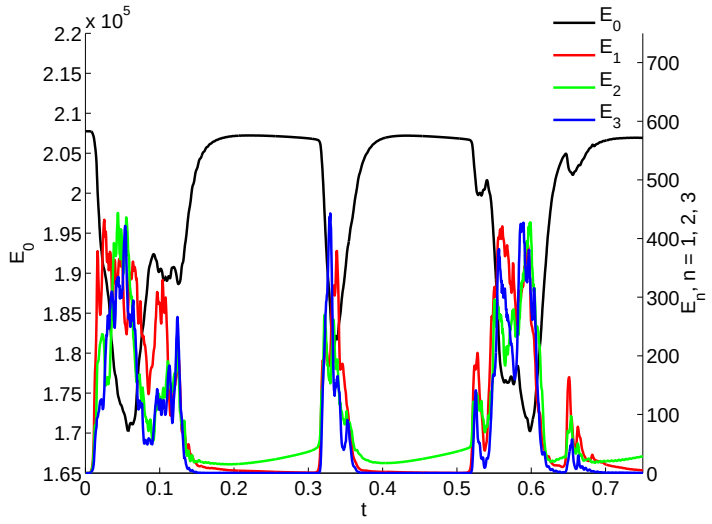

(a)

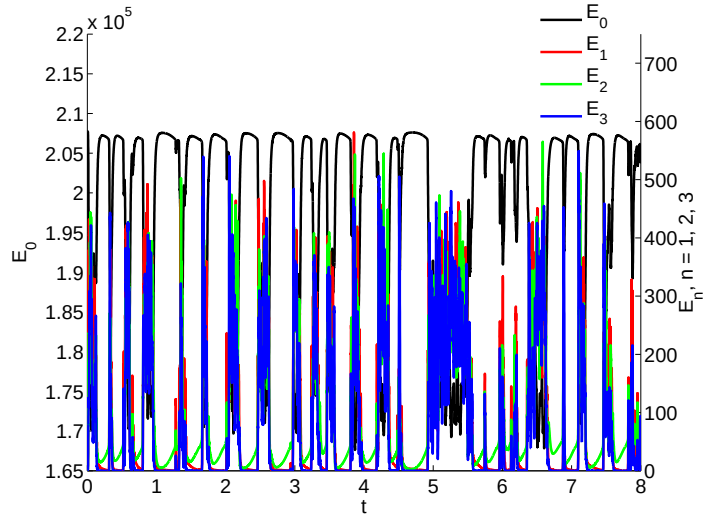

(b)

Figure 3.29 : Energy in modes $0-3$ in time for the $Ta_{m_{\text{t-d, analytic}}} = 1.30 \times 10^5$ simulation with the analytic body force over a) 0.75 nondimensional time units and b) 8.0 nondimensional time units.

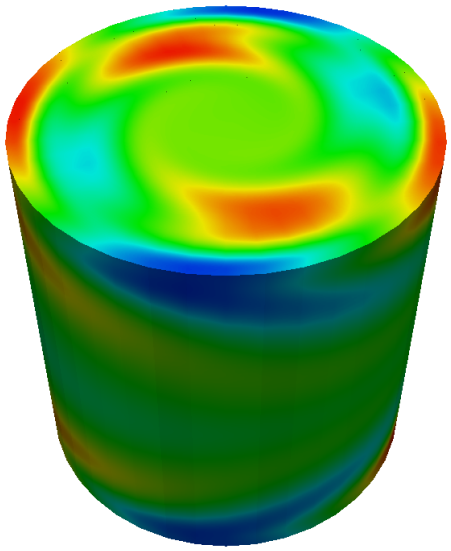

Figure 3.30 : Surface of the melt colored by instantaneous pressure perturbations (after subtracting the base state), indicating the presence of a symmetric $m = 2$ mode at $Ta_{m_{\text{t-d, analytic}}} = 1.30 \times 10^5$, with the flow driven by the analytic body force.

Figure 3.30 shows that during the initial growth phase of the $m = 2$ mode, the pressure perturbations resemble the symmetric $m = 2$ mode as expected from the magnitude of the energy in each mode, and consistent with linear stability theory. In Figure 3.31, the pressure on the surface of the melt and the streamlines at a cross-section of the melt are shown at a time instance of the stochastic flow. The cross-section in Figure 3.31(b) is perpendicular to the front of the region shown in Figure 3.31(a) with the right side of 3.31(b) matching the front of 3.31(a). The nonlinear instabilities come in the form of Taylor-Görtler vortices, which are numerous around the edge as the figure shows. The pressure profile on the surface of the melt is indicative of the motion of the vortices and shows the non-axisymmetric pattern.

The next goal is to narrow in the value of $Ta_{m_{\text{t-d, analytic}}}$ on the point of initial instability. This is found through simulations around the critical value of $Ta^{cr}_{m_{\text{l-s}}} =$

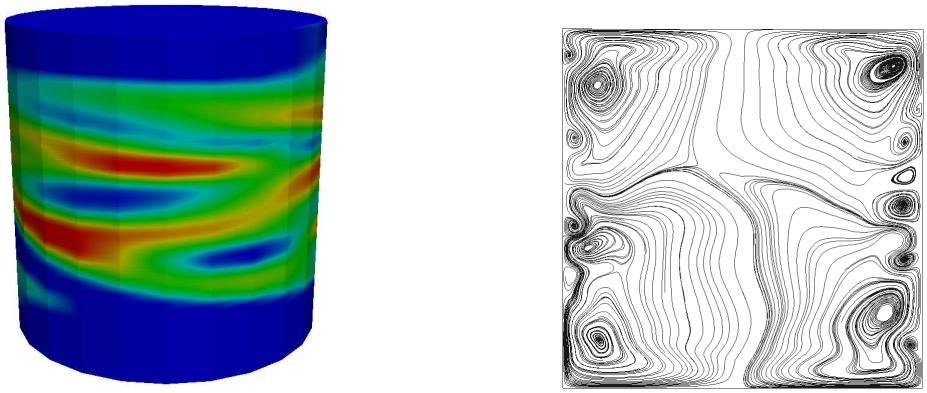

(a) (b)

Figure 3.31 : Visualization of a) the pressure on the surface during a stochastic period and b) planar streamlines showing the stochastic instability in the form of Taylor-Görtler vortices. The plane is through the center of the melt perpendicular to the page with the right side of the plane in (b) corresponding to the front of (a).

1.232×10^5 predicted by linear stability analysis. Simulations were run for magnetic Taylor numbers of 1.22×10^5, 1.23×10^5, and 1.24×10^5. Figure 3.32 shows the energy in the $m = 2$ mode in time, at the three different values of $Ta_{m_{\text{t-d, analytic}}}$. As expected, the $Ta_{m_{\text{t-d, analytic}}} = 1.22 \times 10^5$ and 1.23×10^5 cases showed energy decay in all modes with decay rates for the $m = 2$ mode of 3.20 and 0.51, respectively. The $Ta_{m_{\text{t-d, analytic}}} = 1.24 \times 10^5$ simulation reveals an initial stochastic region as expected and then the $m = 2$ mode begins to grow. However, the flow does not return to the stochastic region as it did when $Ta_{m_{\text{t-d, analytic}}} = 1.30 \times 10^5$, but instead saturates.

This saturation was not seen by Koal *et al.*, who carried out simulations for the same problem at $Ta_{m_{\text{t-d, analytic}}} = 1.25 \times 10^5$ [22]. With Gaussian perturbations with standard deviations of 1%, 0.01%, and even as low as 10^{-10}% of the maximum velocity, they found nonlinear (stochastic) instabilities at $Ta_{m_{\text{t-d, analytic}}} = 1.25 \times 10^5$.

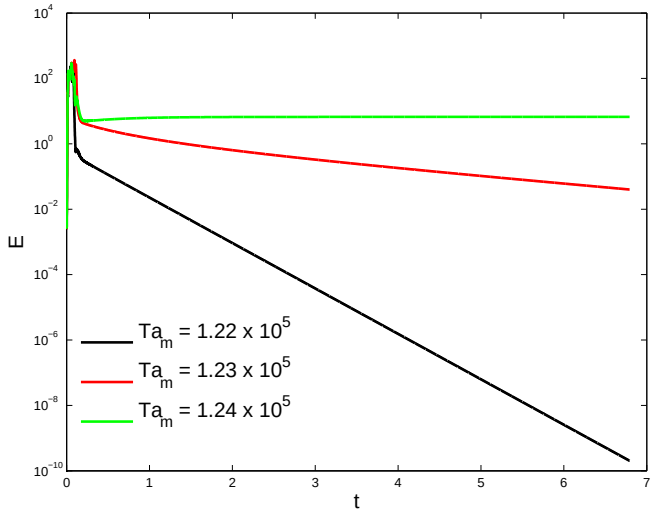

Figure 3.32 : Energy of the $m = 2$ mode in time for flows with magnetic Taylor numbers $Ta_{m_{\text{t-d, analytic}}}$ of 1.22×10^5, 1.23×10^5, and 1.24×10^5.

The appearance of nonlinear saturation suggests a small window exists just above the critical point where the linear instability dominates over the nonlinear, stochastic instabilities. The mechanism switches between $Ta_{m_{\text{t-d, analytic}}} = 1.24 \times 10^5$ and 1.25×10^5. The growth rate at $Ta_{m_{\text{t-d, analytic}}} = 1.24 \times 10^5$ is approximately 0.44 and the decay rate at 1.23×10^5 is approximately 0.51. A linear interpolation of those values gives an estimated critical point of $Ta^{cr}_{m_{\text{t-d, analytic}}} = 1.235 \times 10^5$, which is 0.24% higher than the value predicted by linear stability theory.

Finally, Figure 3.33 shows how the magnitude of the velocity perturbations at $Ta_{m_{\text{t-d, analytic}}} = 1.24 \times 10^5$ compare to those from linear stability theory. Primed variables (marked with $'$) indicate perturbations which do not include the base state. There is decent agreement, indicating that the linearly unstable mode can grow and saturate in time-dependent, three-dimensional simulations. However this mode is very sensitive to Ta_m. With only a slight increase in magnetic Taylor number the perturbation transitions to a state where Taylor-Görtler vortices dominate.

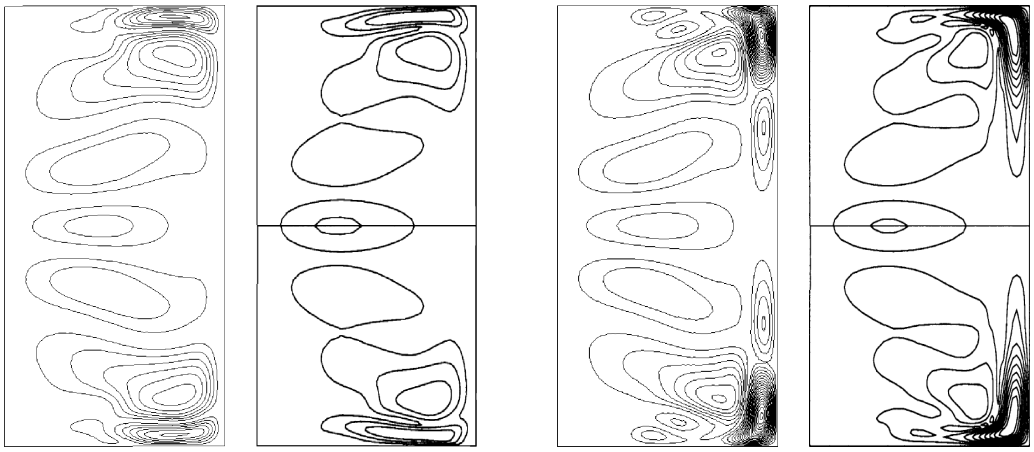

(a) 3D simulations $|v'_{r_{\text{analytic}}}|$ (b) linear stability $|v'_{r_{\text{analytic}}}|$ (c) 3D simulations $|v'_{\theta_{\text{analytic}}}|$ (d) linear stability $|v'_{\theta_{\text{analytic}}}|$

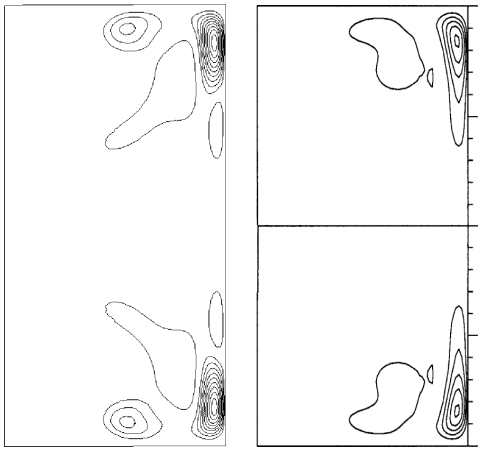

(e) 3D simulations $|v'_{z_{\text{analytic}}}|$ (f) linear stability $|v'_{z_{\text{analytic}}}|$

Figure 3.33 : The magnitude of the radial, azimuthal and axial velocity perturbations from axisymmetric, time-dependent simulations in a), c) and e), respectively, at $Ta_{m_{\text{t-d, analytic}}} = 1.24 \times 10^5$ and from linear stability eigenfuctions in b), d) and f), respectively. The steady base state has been subtracted from the simulations and contours are taken once the flow has reached nonlinear saturation. The azimuthal velocity magnitude is shown in a θ plane where it reaches a maximum and the other two velocity perturbation components are shown in an plane rotated by $\pi/4$ from the that plane. Contour levels from simulations take 20 evenly spaced steps from 0 to $|v'_{\theta_{\text{analytic}}}|$ for all perturbation velocity components. Eigenvector magnitudes from linear stability results are adopted from Grants and Gerbeth [21] for the $m = 2$ mode (reprinted with permission). Both three-dimensional simulations and linear stability results are from analytic EM forcing.

3.6.2 Non-axisymmetric Instabilities Using Numerical Lab Body Forces

The use of the numerical lab body forces introduces significant axial and radial force components that are not present in the analytic body force. Additionally, as the frequency grows the low frequency approximation becomes invalid and the body forces deviate significantly from the analytic force by undershooting them. This subsection investigates how these changes in the forcing function translate to the occurrence of an instability and the type of instability seen.

Figure 3.34 shows the energy in the $m = 2$ mode for runs at $Ta_{m_{\text{t-d, lab}}} = 1.3 \times 10^5$ for frequencies $f^*_{\text{ext}} \geq 1000$ Hz. Because the azimuthal force drops off with increases in frequency, the initial perturbations decay rather quickly for $f^*_{\text{ext}} \geq 2000$ Hz and the decay rate grows as the frequency gets higher. At $f^*_{\text{ext}} = 1000$ Hz, the energy decay is much slower and the decay rate is so small that the magnetic Taylor number for this flow is just below the critical value.

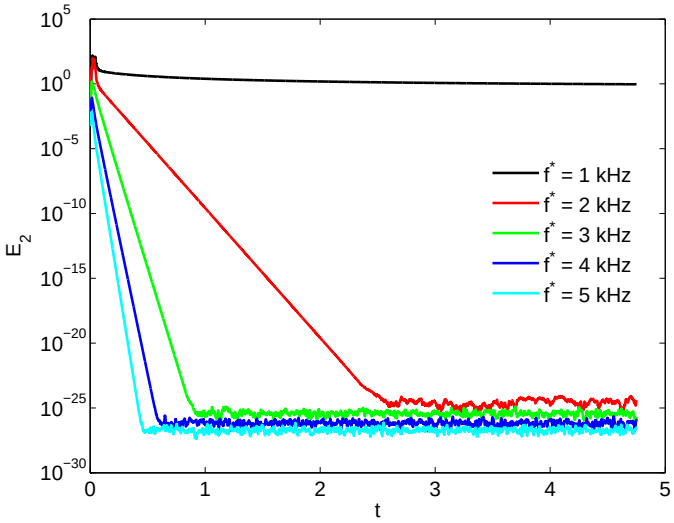

Figure 3.34 : Energies in the $m = 2$ mode versus nondimensional time for $f^*_{\text{ext}} \geq 1000$ Hz at $Ta_{m_{\text{t-d, lab}}} = 1.3 \times 10^5$, showing that the decay rate increases with frequency.

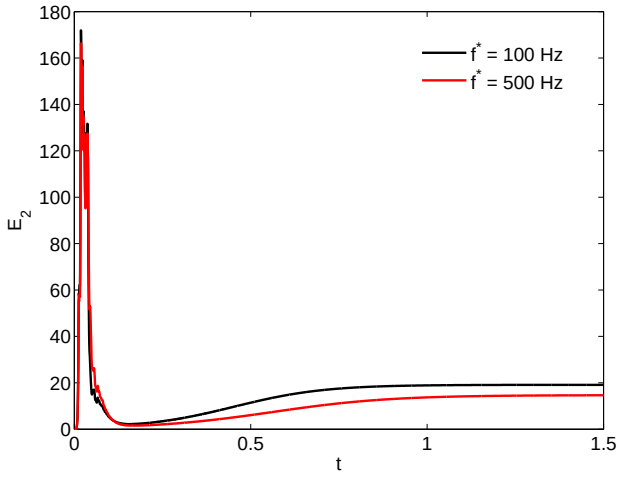

Figure 3.35 : Time evolution of mode 2 energy showing nonlinear saturation for $f^*_{\text{ext}} = 100$ Hz and $f^*_{\text{ext}} = 500$ Hz at $Ta_{m_{\text{t-d, lab}}} = 1.3 \times 10^5$.

Cases for $f^*_{\text{ext}} = 100$ Hz and $f^*_{\text{ext}} = 500$ Hz are initially similar to each other as shown in Figure 3.35. There is a nonlinear stochastic region initially due to the random perturbations. These energies reduce and all modes decay except for the $m = 2$ mode shown, which begins growing. However, unlike the case with the analytic body forces at magnetic Taylor number 1.3×10^5, here the stochastic behavior does not repeat and the $m = 2$ mode saturates. The plot of the mode 2 energies at 100 Hz and 500 Hz can be seen in Figure 3.35. The nondimensional saturation energies and maximum azimuthal velocity perturbations are 19.125 and 41.61, respectively, at $f^*_{\text{ext}} = 100$ Hz, and are 14.671 and 36.65, respectively, at $f^*_{\text{ext}} = 500$ Hz.

Figure 3.36 shows the comparison of the magnitude of velocity perturbation profiles to those from linear stability theory. Primed variables (marked with $'$) indicate perturbations which do not include the base state. Each velocity magnitude demonstrates good agreement between three-dimensional, time-dependent simulations and linear stability eigenmodes.

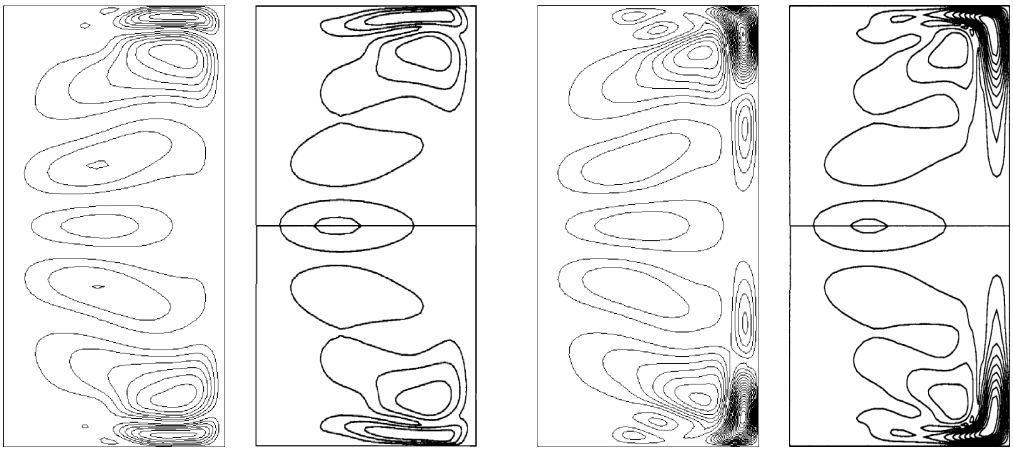

(a) 3D simulations $|v'_{\text{lab},r}|$ (b) linear stability $|v'_{r_{\text{analytic}}}|$ (c) 3D simulations $|v'_{\text{lab},\theta}|$ (d) linear stability $|v'_{\theta_{\text{analytic}}}|$

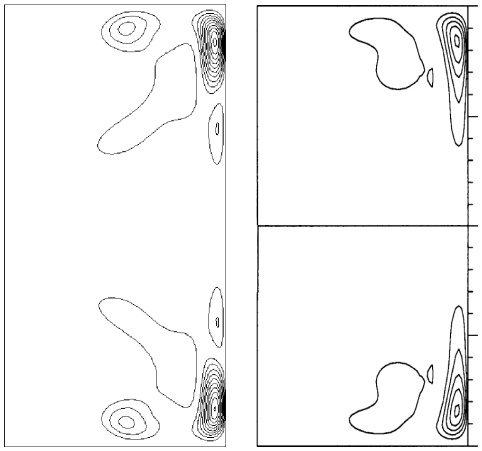

(e) 3D simulations $|v'_{\text{lab},z}|$ (f) linear stability $|v'_{z_{\text{analytic}}}|$

Figure 3.36 : The magnitude of the radial, azimuthal and axial velocity perturbations from 3D, time-dependent simulations in a), c) and e) respectively, at $Ta_{m_{\text{t-d, lab}}} = 1.30 \times 10^5$ and $f^*_{\text{ext}} = 100$, and from linear stability eigenfuctions in b), d) and f), respectively. The steady base state has been subtracted from the 3D simulations and contours are taken once the flow has reached nonlinear saturation. The azimuthal velocity magnitude is shown in a θ plane where it reaches a maximum and the other two velocity perturbation components are shown in an plane rotated by $\pi/4$ from the that plane. Contour levels from simulations take 20 evenly spaced steps from 0 to $|v'_{\theta_{\text{analytic}}}|$ for all perturbation velocity components. Eigenvector magnitudes from linear stability results are adopted from Grants and Gerbeth [21] for the $m = 2$ mode (reprinted with permission). Three-dimensional simulations are forced with $\mathbf{F}^*_{\text{EM,lab}}$. Linear stability results are from azimuthal only forcing with $\langle F_{\text{EM},\theta} \rangle \Big|_{R_\omega \ll 1, \text{ finite, analytic}}$.

This result highlights the difference in the effect of the numerical lab body force, which is much closer to laboratory experiments, versus that of the analytic body force. The high frequency cases are expected to deviate from the analytic case because of the low frequency approximation and they proved to be more stable because of the reduction in the azimuthal force. However, the low frequency approximation leads one to believe that the results should be the same between the low frequency numerical lab cases and the case with the analytic body force. Here, it is shown that this assumption is not entirely valid.

While the body forces in the azimuthal direction are approximated very well by the analytic solution for $R_\omega \ll 1$, there is still some small discrepancy. Additionally, the analytic solution fails to include the axial and radial forces, shown in Figure 3.37. At $Ta_{m_{\text{t-d, lab}}} = 1.30 \times 10^5$, the maximum radial and axial forces are quite substantial. Even at low frequencies ($f^*_{\text{ext}} \leq 1000$ Hz), the maximum radial and axial forces are only approximately one to two orders of magnitude less than the maximum azimuthal force. The difference decreases as the frequency grows. By $f^*_{\text{ext}} = 3000$ Hz, the maximum forces are all the same order of magnitude. This combination of forces has a stabilizing effect, preventing the formation of Taylor vortices and any additional instabilities that form from the $m = 2$ state. A Taylor vortex is caused by relatively fast moving fluid getting force to the boundary where a no-slip condition exists. A boundary layer forms but if the flow just beyond the boundary layer is forced hard enough outward, then the flow "rolls."

The question then is what prohibits the occurrence of the Taylor vortices. The radial and axial force fields plotted in Figure 3.37 show that the radial force is much higher near the radial boundary resisting outward flow, which suggests that it would resist the formation of Taylor vortices. In addition, the axial force also resist flow

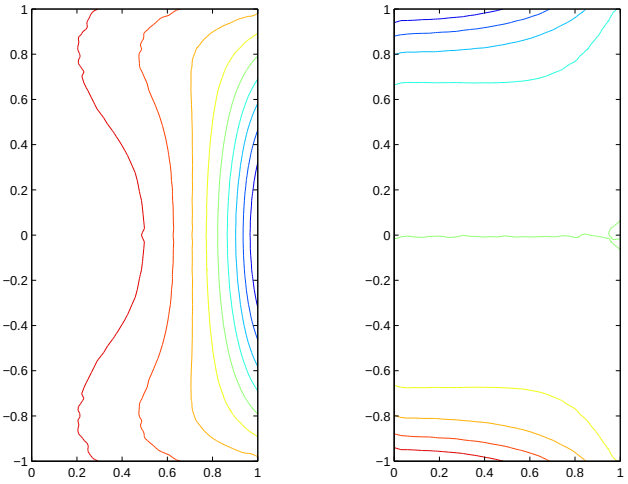

(a) $\langle F_{\mathrm{EM,lab},r} \rangle_{\overline{\theta}}$ $max = 1.73 \times 10^3$

(b) $\langle F_{\mathrm{EM,lab},z} \rangle_{\overline{\theta}}$ $max = 2.30 \times 10^3$

Figure 3.37 : Nondimensional radial and axial numerical lab forces for $Ta_{m_{\text{t-d, lab}}} = 1.3 \times 10^5$ and $f^*_{\text{ext}} = 100$. The maximum values for these forces are almost two orders of magnitude smaller than the maximum azimuthal force, $\langle F_{\mathrm{EM,lab},\theta} \rangle_{\overline{\theta},max} = 9.55 \times 10^4$.

into the boundary layer at the top and bottom axial boundaries, again leading one to believe that instabilities would be damped in this region as well.

To test the hypothesis that the additional radial and axial forces are the primary resistive force against Taylor vortex formation, simulations were run using the numerical lab azimuthal force with the radial and axial forces set to zero. However, the hypothesis was shown to be incorrect as the linear instability formed with no additional instabilities occurring.

The next test was to keep the radial and axial lab forces but use the analytic azimuthal force. This resulted in Taylor vortices as seen in the purely analytic forcing case. Thus, the numerical azimuthal force seems to be key in allowing for nonlinear saturation despite the seemingly minor difference between the numerical force and analytic force at $f^*_{\text{ext}} = 100$ Hz.

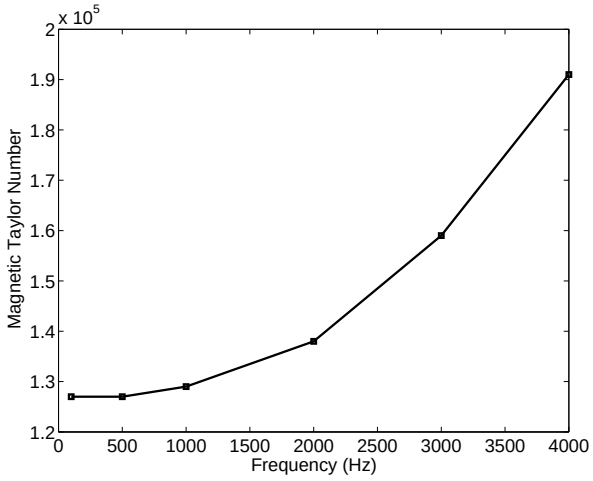

Figure 3.38 : The predicted critical lab magnetic Taylor numbers $Ta^{l}_{m_{\text{t-d, lab}}}$ as frequency increases. Critical values are predicted through a linear interpolation of growth and decay rates above and below the critical point, respectively.

Finally, frequency impact on the critical magnetic Taylor number was investigated. The approach here was to use growth and decay values with linear interpolation to predict the point of instability [44]. Then simulations were run above and below this estimated critical point to bound it. Figure 3.38 shows the lower bound for the critical value. The upper bound in each case is 0.01×10^5 higher in magnetic Taylor number. At low frequencies, the critical lab magnetic Taylor number $Ta^{cr}_{m_{\text{t-d, lab}}}$ is similar to, but a bit higher than, the critical value in the analytic case as expected. At $f^{*}_{\text{ext}} = 100$ Hz, the lower bound is $Ta^{l}_{m_{\text{t-d, lab}}} = 1.27 \times 10^5$, which means the upper bound is $Ta^{u}_{m_{\text{t-d, lab}}} = 1.28 \times 10^5$. This upper bound is 3.9% higher than the value predicted by linear stability analysis using the analytic force ($Ta^{cr}_{m_{\text{l-s}}} = 1.232 \times 10^5$).

The critical value grows slightly at $f^{*}_{\text{ext}} = 1000$ Hz, but begins to grow more rapidly after. The upper bound on the critical Taylor number for $f^{*}_{\text{ext}} = 4000$ Hz was as high as $Ta^{u}_{m_{\text{t-d, lab}}} = 1.92 \times 10^5$, 55.84% higher than the value found with linear stability analysis and the analytic force. Table 3.4 shows the upper and lower bounds for

each frequency and also provides the growth and decay rates for simulations where they could be found. That is, because the flow is initially nonlinearly unstable to stochastic perturbations, the energy grows rapidly before dropping and then growing more predictably again in the linear regime. Only in cases when the energy dropped low enough before the exponential growth of the mode began could a growth rate be determined. In some cases the energy drop from the stochastic region makes it appear that the energy in that mode is decaying, when in actuality it is just decaying to its saturation energy. In these cases the linear growth never appears explicitly.

Table 3.4 : The bounds on the critical lab magnetic Taylor number for the numeric lab-forced flows as the frequency increases. The superscripts l and u are used to denote lower and upper bounds, respectively. The rates for growth and decay are given. Note that some growth rates can not be extracted from energy plots due to the initial nonlinear instability.

f^*_{ext} (Hz)	$Ta^l_{m_{\text{t-d, lab}}} \times 10^{-5}$	Decay Rate	$Ta^u_{m_{\text{t-d, lab}}} \times 10^{-5}$	Growth Rate
100	1.27	1.06	1.28	0.17
500	1.27	2.78	1.28	
1000	1.29	2.56	1.30	
2000	1.38	2.14	1.39	
3000	1.59	1.15	1.60	1.13
4000	1.91	0.83	1.92	1.19

3.7 RMF Conclusions

The objective of the current study is to compare theoretical and laboratory solutions to the same problem within the bounds in which the theory is applicable and beyond. This means comparing to the theoretical and laboratory force fields and the effect they have on the base flow and instabilities.

First, the time-averaged force fields were compared and the azimuthal component was shown to be very similar for all external frequencies studied. The differences were more noticeable at high frequencies, as expected, where the high magnetic shielding caused the force to be more localized to near the radial boundary, which can be seen as stretching of the force contour lines near the radial surface. Additionally, the magnitude of the lab azimuthal force showed a significant drop when compared to the analytic solution as the frequency increased. The increase in frequency also increased the magnitude of the radial and axial forces that are zero in the analytic solution.

The effect of the difference in forces was investigated in the solutions for the axisymmetric, steady base flow. Again, the flow contours showed only minor differences at low frequencies, but the differences did become more apparent at higher frequencies. The reduction in maximum velocities can be attributed to the reduction in the azimuthal force with the increase in frequency.

Next, instabilities through analytic forcing and laboratory forcing were analyzed. The flow was first restricted to axisymmetric instabilities and bounds were found via time-dependent simulations on the axisymmetric critical magnetic Taylor number, driven by the analytic EM body force. The critical axisymmetric value from linear stability theory ($Ta^{\text{axi},cr}_{m_{\text{l-s}}} = 1.636 \times 10^5$) was contained within $Ta^{\text{axi}}_{m_{\text{t-d, analytic}}}$ between the bounds of 1.60×10^5 and 1.65×10^5. The critical frequency on the upper bound matched well, and the perturbation flow field matched the eigenfunctions from linear

stability theory, as shown in Figure 3.27.

Then, the flow was allowed to be fully three-dimensional and the analytic forces were applied to time-integrations. Results at $Ta_{m_{\text{t-d, analytic}}} = 1.3 \times 10^5$, included in Figure 3.29, agreed well with those found by Koal *et al.* [22], with small perturbations leading to the development of nonlinear instabilities and stochastic flow characterized by Taylor-Görtler vortices. The stochastic region was followed by a return to the base state and subsequent initial increase in the $m = 2$ modal energy as expected, but the stochastic flow reappeared soon after. This pattern of linear and nonlinear instabilities continued for the duration of the simulation. However, simulations at Taylor numbers just above the critical point found through linear stability analyses ($Ta^{cr}_{m_{\text{l-s}}} = 1.232 \times 10^5$) exhibited different behavior. At $Ta_{m_{\text{t-d, analytic}}} = 1.24 \times 10^5$ the initial stochastic region formed, but quickly gave way to the linear instability that proceeded to grow and saturate, as shown in Figure 3.32.

With the laboratory forces, the linear instability consistently dominated over the nonlinear instability, as seen through plots of the modal energy. The $m = 2$ symmetric mode was found in each case and the flow perturbation contours matched well with the eigenfunctions from linear stability analyses. Even at low frequencies where the analytic force matched very well with the laboratory force, the small differences were enough to stabilize the flow against transitions to nonlinear stochastic flow regimes. Additionally, bounds were found for the critical magnetic Taylor number for the range of frequencies studied, shown in Figure 3.38. For frequencies less than 1 kHz, the critical point calculated through numerical simulations with lab forces was about 4% higher than expected value from linear stability theory. The instabilities were axially symmetric with $m = 2$, consistent with linear stability theory. Beyond 1 kHz, the frequency had a more considerable stabilizing effect as the critical Taylor number

grew to as high as $Ta^{u}_{m_{\text{t-d, lab}}} = 1.92 \times 10^5$ (upper bound) at $f^{*}_{\text{ext}} = 4000$ Hz, though the instability remained $m = 2$ and symmetric in the axial direction.

Thus the frequency, which is not accounted for in RMF studies that utilize the analytic EM body force, has a significant impact on the value of the critical magnetic Taylor number in the lab setting. As the frequency increases between 1 and 4 kHz, the base flow is significantly stabilized. Furthermore, the flow driven by the lab RMF forces is much less vulnerable to stochastic instabilities, and this remains true over all the frequencies studied.

Chapter 4

Traveling Magnetic Field

Next, stirring the melt with a Traveling Magnetic Field (TMF) is analyzed. The primary goal of TMF stirring is to counteract the effects of gravity by creating a strong flow in the axial direction that carries heavier elements back to the growth front rather than allowing them to settle at the bottom. However, crystal growth is most effective under laminar conditions so this analysis is aimed at finding the points of instability and understanding the physics in stable and unstable flow regimes.

Figure 4.1 shows the model for the TMF case. The theoretical TMF can be

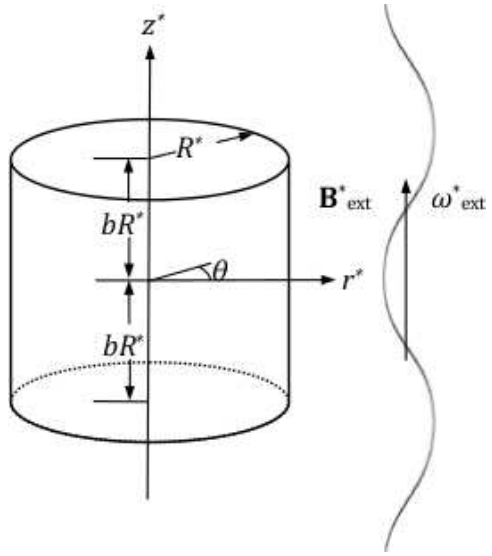

Figure 4.1 : The cylindrical melt domain exposed to an external magnetic field $\mathbf{B}^*_{\text{ext}}$ traveling in the axial direction with a wavelength $\lambda^* = 2\pi/k^*$ and frequency $f^*_{\text{ext}} = \omega^*_{\text{ext}}/(2\pi)$.

introduced through the vector potential $\mathbf{A}^*$ defined by

$$\nabla^* \times \mathbf{A}^* = \mathbf{B}^* \tag{4.1}$$

with

$$\nabla^* \cdot \mathbf{A}^* = 0. \tag{4.2}$$

Substituting for $\mathbf{A}^*$ in Faraday's law gives

$$\nabla^* \times \mathbf{E}^* = -\nabla^* \times \frac{\partial \mathbf{A}^*}{\partial t^*} \tag{4.3}$$

Recognizing that the curl of a gradient is zero, Equation 4.3 allows solutions of the form

$$\mathbf{E}^* = -\frac{\partial \mathbf{A}^*}{\partial t^*} - \nabla^* \phi^* \tag{4.4}$$

where ϕ^* is the electrostatic potential function.

A typical analytic form for an axially aligned TMF is given by

$$\mathbf{A}^*_{\text{ext}_{\text{analytic}}} = 0.5 B_0^* r^* \cos\left(\omega^*_{\text{ext}} t^* - k^* z^*\right) \hat{\mathbf{e}}_\theta \tag{4.5}$$

where B_0^* is the amplitude of the traveling magnetic field, ω^*_{ext} is the AC frequency, k^* is the axial wavenumber, r^* is the radial coordinate, z^* is the axial coordinate, and t^* is time. With this vector potential, the magnetic field is

$$\mathbf{B}^*_{\text{ext}_{\text{analytic}}} = \nabla^* \times \mathbf{A}^*_{\text{ext}_{\text{analytic}}} = 0.5 B_0^* k^* r^* \sin\left(k^* z^* - t^* \omega^*_{\text{ext}}\right) \hat{\mathbf{e}}_r + B_0^* \cos\left(k^* z^* - t^* \omega^*_{\text{ext}}\right) \hat{\mathbf{e}}_z. \tag{4.6}$$

Because of the small magnetic Reynolds number, $\mathbf{B}^*$ is decoupled from the flow field and the magnetic field can first be solved to find the Lorentz force for the flow equations.

The nondimensional Navier-Stokes equations (Equation 2.32) from Chapter 2 are

$$\frac{\partial \mathbf{v}}{\partial t} + (\mathbf{v} \cdot \nabla)\mathbf{v} = -\nabla P + \underbrace{\frac{\mu^*}{\rho^* V_0^* L_0^*}}_{\frac{1}{Re_{\text{classic}}}} \nabla^2 \mathbf{v} + \frac{\sigma^* V^*_{rel,0} B_0^{*2} L_0^{*3}}{\rho^* \nu^{*2}} (\mathbf{j} \times \mathbf{B}),$$

and continuity (Equation 2.33) gives

$$\nabla \cdot \mathbf{v} = 0.$$

Again the viscous Reynolds number is set to unity by the choice of the viscous velocity scale $V_0^* = \mu^*/(\rho^* L_0^*)$. The relative velocity scale is chosen such that the TMF Taylor number matches the nondimensional forcing parameter of Grants and Gerbeth [20]. Thus, the relative velocity scale is $V_{rel,0}^* = \omega_{\text{ext}}^* k^* L_0^{*2}/2$ and the Navier-Stokes equations for TMF forcing are

$$\frac{\partial \mathbf{v}}{\partial t} + (\mathbf{v} \cdot \nabla)\mathbf{v} = -\nabla P + \nabla^2 \mathbf{v} + \underbrace{\frac{\sigma^* \omega_{\text{ext}}^* k^* B_0^{*2} L_0^{*5}}{2\rho^* \nu^{*2}}}_{2 \times Ta_{\text{TMF}}} \mathbf{j} \times \mathbf{B} \tag{4.7}$$

where the magnetic Taylor number for the TMF

$$Ta_{\text{TMF}} = \frac{\sigma^* \omega_{\text{ext}}^* k^* B_0^{*2} L_0^{*5}}{4\rho^* \nu^{*2}} \tag{4.8}$$

measures the electromagnetic body force of a traveling magnetic field over viscous effects. Like in the RMF case, the factor of 2 is used in scaling the body force so that $\mathbf{F}_{\text{EM}}^*$ then scales as $\sigma^* \omega_{\text{ext}}^* B_0^{*2} L_0^*/2$. The resulting nondimensional Navier-Stokes equations when exposed to a traveling magnetic field are

$$\frac{\partial \mathbf{v}}{\partial t} + (\mathbf{v} \cdot \nabla)\mathbf{v} = -\nabla P + \nabla^2 \mathbf{v} + Ta_{\text{TMF}} \mathbf{F}_{\text{EM}}. \tag{4.9}$$

Again, the TMF magnetic Taylor number is the parameter that governs the flow and will be used to define the point of instability.

The parameters used throughout this chapter for all calculations and computations are listed in Table 4.1.

4.1 TMF Model

The TMF model, much like the RMF model, attempts to approximate a laboratory configuration. The target magnetic field in this case is one that is sinusoidal in the

Table 4.1 : Physical properties of the melt (held constant) and resulting derived scales used for all computations involving the TMF. Note that the viscous velocity scale is equal to ν^*/L_0^*, giving a classic viscous Reynolds number of one.

magnetic permeability $\mu_p^* = \mu_0^*$	$4\pi \times 10^{-7}$ N/A^2
electrical conductivity σ^*	945,000 S/m
density ρ^*	6135 kg/m^3
kinematic viscosity ν^*	1.74×10^{-7} m^2/s
length scale $L_0^* = R^*$	0.01275 m
resulting derived scales:	
magnetic diffusivity $\eta^* = 1/(\mu_p^* \sigma^*)$	1.1875 m^2/s
viscous velocity scale V_0^* (such that $Re_{classic} = 1$)	1.365×10^{-5} m/s
flow time scale $t_{0_{\text{flow}}}^* = L_0^*/V_0^*$	934.0 s
magnetic Reynolds number $R_m = \mu_p^* \sigma^* V_0^* L_0^* = V_0^* L_0^*/\eta^*$	1.466×10^{-7}

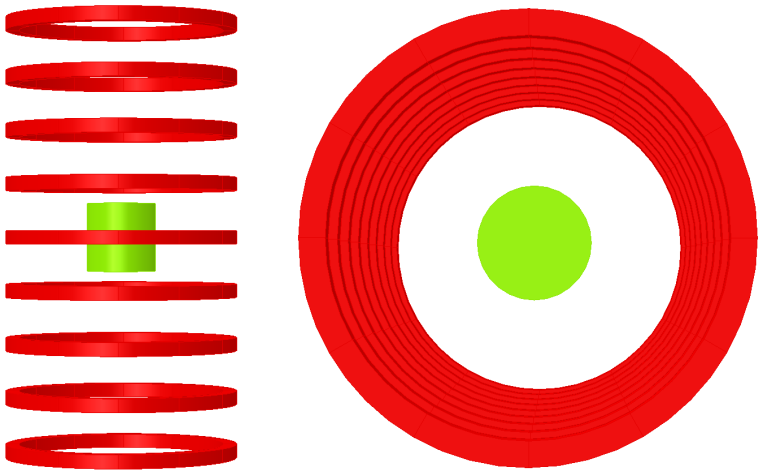

(a) Side View (b) Top View

Figure 4.2 : Setup in Opera to generate the TMF consisting of nine AC solenoids (red rings) and a melt region (green cylinder) located in the center.

axial direction and is given by Equation 4.6.

The TMF induced body forces are found through the use of Opera. The TMF setup is shown from the side and from the top in Figure 4.1. There are 9 coils placed in a series with uniform spacing in the axial direction, symmetric about the midplane. This geometry remains constant for all simulations. The total current is the same in each coil, but changes from one simulation to the next to achieve a desired magnetic Taylor number.

While the dimensions of the coils are somewhat arbitrary, these are included here for completeness. The coils have an inner diameter of three times the melt radius, $3R^* = 0.03825$ m, and a square cross-section that is 0.005 m by 0.005 m. The coils are axisymmetric about the axis so the resulting fields and forces are axisymmetric. Opera does not have an axisymmetric option, but does allow for a thin 3D wedge domain. Thus, only 1/16 of the domain is simulated. The full domain mesh and a

close-up on the melt are shown in Figure 4.3. The full domain surrounding the melt has a radius of 0.08 m and a total length of 0.156 m.

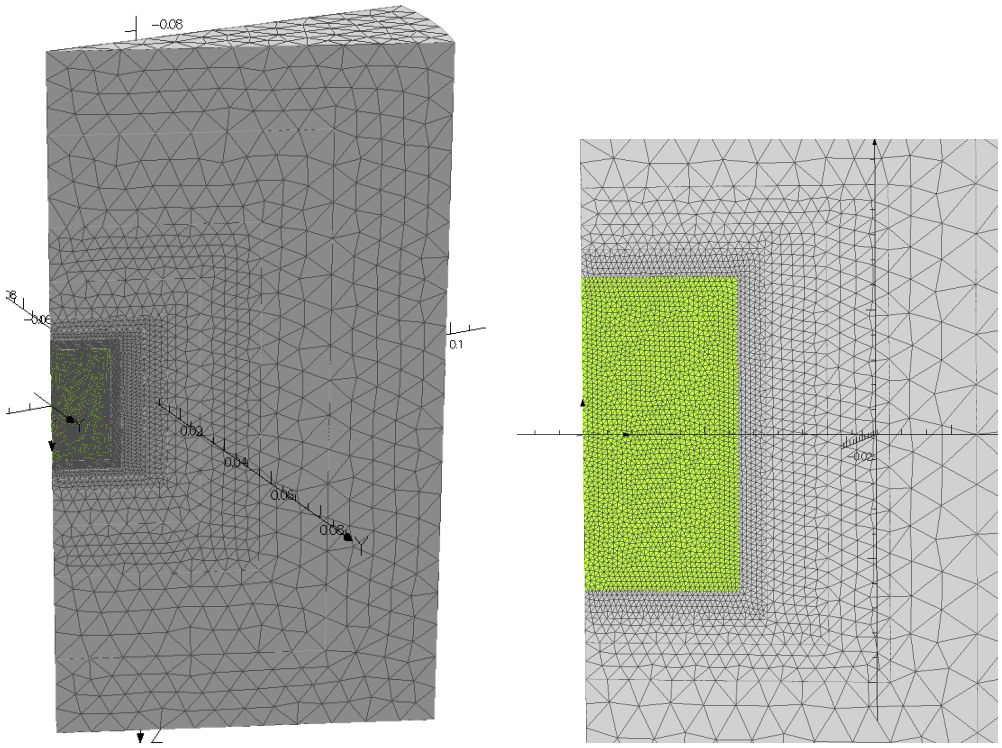

(a) (b)

Figure 4.3 : a) The entire mesh used for the TMF simulations in Opera. b) A close-up on the mesh showing fineness of the melt. The mesh has a total of 321,902 elements and 123,695 nodes.

The mesh here is similar to the one from the RMF case in that it uses an unstructure mixed set of linear and quadratic tetrahedral elements, uses "air cylinders" to control the maximum element size as we move outward radially, and cuts each subdomain into even smaller domains to help with meshing. The melt is set to have a maximum element size of 0.0005 m and the air cylinders have maximum element sizes of 0.001 m, 0.002 m, 0.004 m, and 0.008 m, as we move outward radially away from the melt. The mesh consists of 321,902 elements and 123,695 nodes. The solenoids

are not meshed as they are governed by the Biot-Savart law, which is applied at every node for every solenoid.

Opera's ELEKTRA Steady State solver is used to solve the problem, which only takes 5-6 minutes since the domain is so small. The fields are viewed in Opera's post-processor and the Lorentz forces are calculated. Since the simulation is essentially axisymmetric, it is not necessary to get the force in a three-dimensional box as was required for the RMF. Instead, forces are calculated on a single plane and then averaged over 180 distinct, evenly-spaced time instances of the AC cycle. The time-averaged data is loaded into Matlab where the incorrectly interpolated edges given by Opera can be cut away and recomputed through the use of Matlab's *v4* extrapolation routine [39]. The absolute value of the axial magnetic field is carried through these calculations as well so that the appropriate B_0^* can be chosen.

4.2 Electromagnetics of the TMF

The purpose of this work is to investigate the deviation of a TMF generated in a 'lab' from that approximated by the analytic solution given by Equation 4.6. All cases studied are in the low magnetic Reynolds number limit, $R_m \ll 1$, such that secondary EM fields induced by the flow of the electrically conducting melt are negligible and the solution to the EM fields decouples from the solution of the flow field. The low value of R_m given in Table 4.1 justifies this assumption.

In the low frequency limit $R_\omega \ll 1$ and there is negligible shielding. The magnetic flux density in the melt will then be identical to that if the melt was removed. The low shielding parameter limit requires

$$R_\omega = \mu_p^* \sigma^* R^{*2} \omega_{\text{ext}}^* = \mu_p^* \sigma^* R^{*2} (2\pi f_{\text{ext}}^*) \ll 1 \tag{4.10}$$

for the low frequency approximation to remain valid. Substituting in the values $\mu_p^* = \mu_0^* = 4\pi \times 10^{-7}$ N/A^2, $\sigma^* = 945,000$ S/m and $R^* = 0.01275$ m, the low frequency approximation is valid when

$$f_{\text{ext}}^* \ll 824 \text{ Hz}. \tag{4.11}$$

It is useful to first describe the physics in this limit.

4.2.1 Analytic Solution for the TMF Body Force with Long Axial Wavelength and $R_\omega \ll 1$ in a Cylindrical Melt

The theoretical TMF was introduced at the beginning of Chapter 4 and the expression for the magnetic field was obtained from a magnetic vector potential expressed in Equation 4.5 and given in Equation 4.6. If we assume that k^* is very small, then the wavelength of the TMF, $\lambda^* = 2\pi/k^* \gg R^*$.

In general, Ohm's Law (Equation 2.5) gives

$$\mathbf{j}^* = \sigma^*(\mathbf{E}^* + \mathbf{v}_{\text{rel}}^* \times \mathbf{B}^*), \tag{4.12}$$

where σ^* is the electrical conductivity. For the TMF, this scales as

$$j_0^* \, \mathbf{j} = \sigma^* \left(\frac{L_0^* B_0^*}{t_{0_{\text{EM}}}^*} \, \mathbf{E} + V_{\text{rel},0}^* B_0^* \, \mathbf{v}_{\text{rel}} \times \mathbf{B} \right), \tag{4.13}$$

where Faraday's law has been used to relate the electric field scaling to the magnetic flux density scaling. The characteristic velocity at which the external EM field is driven is given by $U_{0_{\text{EM}}}^* = L_0^*/t_{0_{\text{EM}}}^*$, where $U_{0_{\text{EM}}}^*$ is the wave speed (phase velocity) given by $\omega_{\text{ext}}^*/k^*$. The relative velocity scale of the flow is $V_{rel,0}^* = \omega_{\text{ext}}^* k^* L_0^{*2}/2$. With these scales, Equation 4.13 then becomes

$$j_0^* \, \mathbf{j} = \frac{\sigma^* \omega_{\text{ext}}^* B_0^*}{k^*} \, \mathbf{E} + \frac{\sigma^* \omega_{\text{ext}}^* k^* L_0^{*2} B_0^*}{2} \, \mathbf{v}_{\text{rel}} \times \mathbf{B}. \tag{4.14}$$

Dividing by the dimensional coefficient on $\mathbf{E}$, replacing $L_0^* = R^*$ and taking the characteristic electric current density to be $j_0^* = \sigma^* \omega_{\text{ext}}^* B_0^* / k^*$ gives

$$\mathbf{j} = \mathbf{E} + \frac{k^{*2} R^{*2}}{2} \mathbf{v}_{\text{rel}} \times \mathbf{B}. \tag{4.15}$$

Thus, for $k^* R^* \ll 1$, the $\mathbf{v}_{\text{rel}} \times \mathbf{B}$ induced electric current density is negligible compared to the contribution from the electric field.

Replacing $\mathbf{E}^*$ in Equation 4.12 by using Equation 4.4, and applying the above scaling yields the simplified version of Ohm's law for a TMF

$$\mathbf{j}^*\Big|_{k^* R^* \ll 1} = \sigma^* \left(-\frac{\partial \mathbf{A}^*}{\partial t^*} - \nabla^* \phi^* \right) \tag{4.16}$$

where ϕ^* denotes the electric potential. Taking the divergence of this expression and applying conservation of charge and the solenoidal nature of $\mathbf{A}^*$ leaves only

$$\nabla^{*2} \phi^* = 0. \tag{4.17}$$

Since the normal component of $\mathbf{j}^*$ is zero on the boundary, $\partial \phi^* / \partial n^* = 0$ on the boundary. This leads to $\nabla^* \phi^* = 0$ throughout the domain. Thus, the electric current density in the melt can be written as

$$\mathbf{j}^*\Big|_{k^* R^* \ll 1} = -\sigma^* \frac{\partial \mathbf{A}^*}{\partial t^*} = 0.5 \sigma^* \omega_{\text{ext}}^* B_0^* r^* \sin\left(\omega_{\text{ext}}^* t^* - k^* z^*\right) \hat{\mathbf{e}}_\theta. \tag{4.18}$$

In the low frequency limit, $\mathbf{B}$ in the melt approaches $\mathbf{B}_{\text{ext}}$ given by Equation 4.6 and the Lorentz force is then

$$\mathbf{F}_{\text{EM}}^* = \mathbf{j}^*\Big|_{k^* R^* \ll 1} \times \mathbf{B}^*\Big|_{R_\omega \ll 1} =$$
$$0.25 B_0^{*2} r^* \sigma^* \omega_{\text{ext}}^* \left[-2 \cos\left(k^* z^* - t^* \omega_{\text{ext}}^*\right) \sin\left(k^* z^* - t^* \omega_{\text{ext}}^*\right) \hat{\mathbf{e}}_r + \sin^2\left(k^* z^* - t^* \omega_{\text{ext}}^*\right) \hat{\mathbf{e}}_z \right]. \tag{4.19}$$

Time-averaging zeros out the radial component and leaves just the axial component

$$\left\langle F_{\text{EM},z}^* \right\rangle\Big|_{R_\omega \ll 1,\, k^* R^* \ll 1,\, \text{analytic}} = \frac{\sigma^* \omega_{\text{ext}}^* B_0^{*2} k^* r^{*2}}{8}. \tag{4.20}$$

4.2.2 Analytic Solution for the TMF Body Force with Arbitrary Axial Wavelength and R_ω in a Cylindrical Melt

In the case where the wavenumber and the shielding parameter can be arbitrarily large, the forces become [45]

$$F_r^* = \frac{\sigma^* \omega_{\text{ext}}^* B_0^{*2} k^*}{2} \frac{\text{Im}[\beta^* I_1(\beta^{*\dagger} r^*) I_0(\beta^* r^*)]}{k \left|\beta^* I_0(\beta^*)\right|^2} \tag{4.21}$$

$$F_z^* = \frac{\sigma^* \omega_{\text{ext}}^* B_0^{*2} k^*}{2} \frac{\left|I_1(\beta^* r^*)\right|^2}{\left|\beta^* I_0(\beta^*)\right|^2} \tag{4.22}$$

where $k = k^* R^*$ and $\beta^* = \sqrt{k^2 + iR_\omega}$. However, Galindo *et al.* [29] found through numerical simulations that the axial force along the midplane agrees better with Equation 4.20 than Equation 4.22.

4.2.3 Lab TMF Body Forces at Arbitrary R_ω, Compared to the Analytic Body Force Valid at $R_\omega \ll 1$

Figure 4.4 shows the lab magnetic field at different angles of the AC cycle for $f_{\text{ext}}^* = 10$ Hz and $k = k^* L_0^* = 0.5$. The wavelength stretches from the bottom coil to the top coil and at $\theta = 0°$, when the bottom and top coils are both at their maximum current. Thus, those coils are at their maximum magnetic field contribution in the positive z^* direction. The centerpoint of the wave, which is aligned with the center of the melt at $z^* = 0$, is then at a minimum, meaning that the field is at full strength, but pointing in the negative z^* direction, which can be seen in the first plot of Figure 4.4. As the AC angle is increased, it is easy to see the wave moving through the melt. At an angle of 90° and 270°, the axial component of the magnetic field at the centerline is expected to be at zero and the results show this to be true. As the end of the cycle is approached, the wave appears to be starting back at the beginning.

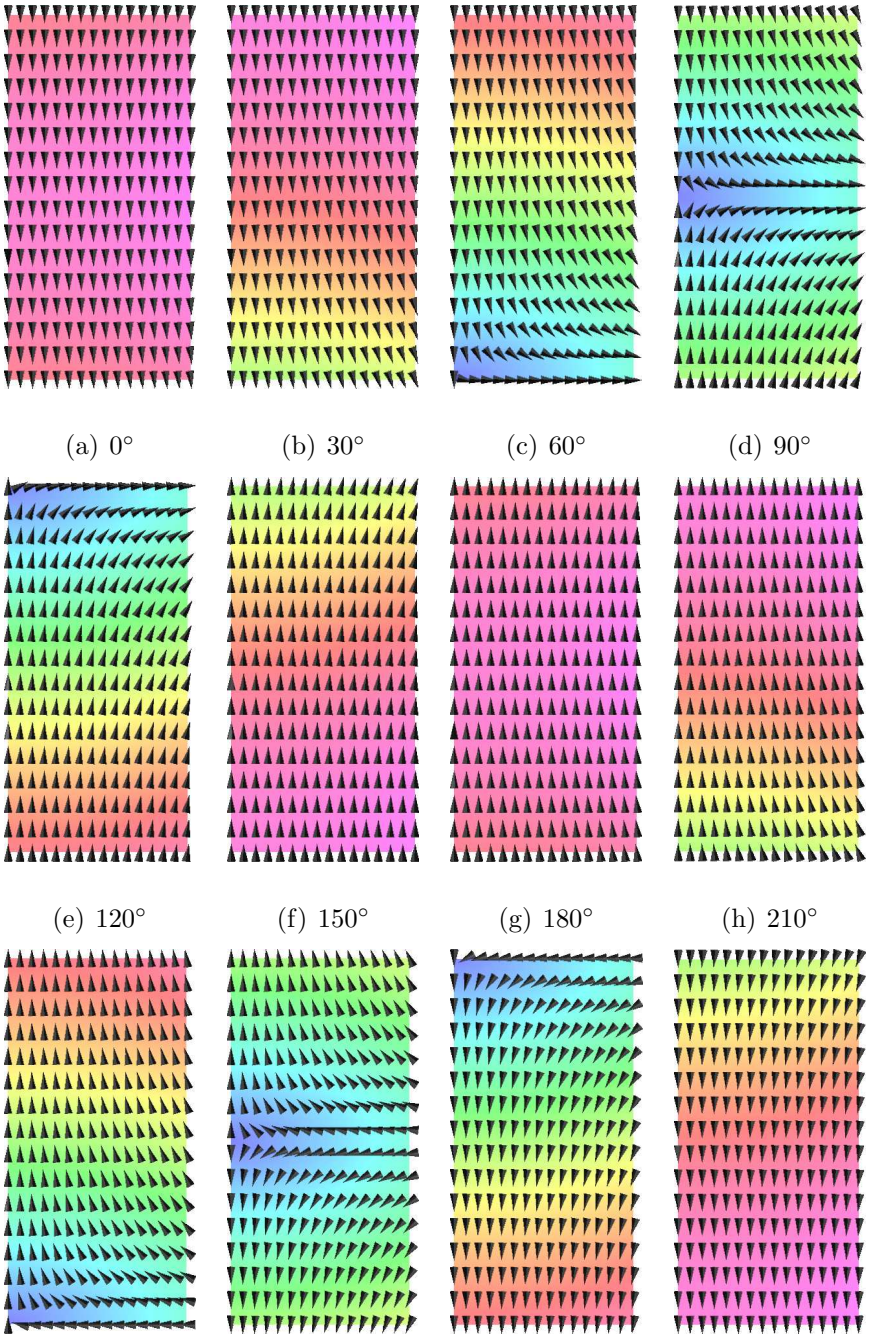

(a) 0° (b) 30° (c) 60° (d) 90°

(e) 120° (f) 150° (g) 180° (h) 210°

(i) 240° (j) 270° (k) 300° (l) 330°

Figure 4.4 : The magnetic flux density on an $r^* - z^*$ plane at several time instances in an AC cycle of the TMF at $f^*_{\text{ext}} = 10$ Hz. The color and vectors indicates the magnitude and direction of $\mathbf{B}^*$, respectively.

Figure 4.5 shows the magnetic flux density, the current density, and the electromagnetic body force at an AC angle of 60°. Equation 4.18 indicates that the current density should be sinusoidal in z^* and linear in r^*, with all current going in the azimuthal direction. At 60° the sinusoid is positive so the current should be in the negative azimuthal direction. The figure shows this to be the case. We have shown that the resulting force should only have an axial component quadratic in r^*, but that is when time-averaged. The force at a time instance also includes a radial force that is much stronger than the axial force for small $k^* L_0^*$. Thus, the force in Figure 4.5 is primarily radial.

For force computations, the correct B_0^* must be calculated. For the TMF, B_0^* is defined as the maximum value of B_z^* at the centerline $z^* = 0$. To get this value, the absolute value of B_z^* is time-averaged. Since the expected form is $B_z^* = B_0^* \cos(k^* z^* - \omega_{\text{ext}}^* t^*)$, the value of B_0^* falls out of the time integration such that

$$\frac{\omega_{\text{ext}}^*}{2\pi} \int_0^{2\pi/\omega_{\text{ext}}^*} |B_z^*| \, dt = \frac{2B_0^*}{\pi}. \tag{4.23}$$

Thus, the time-averaged absolute values of B_z^* taken from Opera can be multiplied by $\pi/2$ to get B_0^*.

Figure 4.6 shows how the time-averaged absolute value of the axial component of the magnetic field changes over the domain as the frequency is increased. As expected, the magnetic shielding effect impacts the magnetic field by pushing it outward and upward in the direction of the traveling magnetic field.

Next, we look at how the force field changes with frequency. In Figure 4.7, the body force at $f_{\text{ext}}^* = 10$ Hz is clearly only a function of r^* and shows good agreement with the analytic force for low frequency and small wavenumber. As the frequency increases, the force becomes stronger in the bottom half of the domain, and in particular is strongest where the radial surface meets the bottom of the domain. The

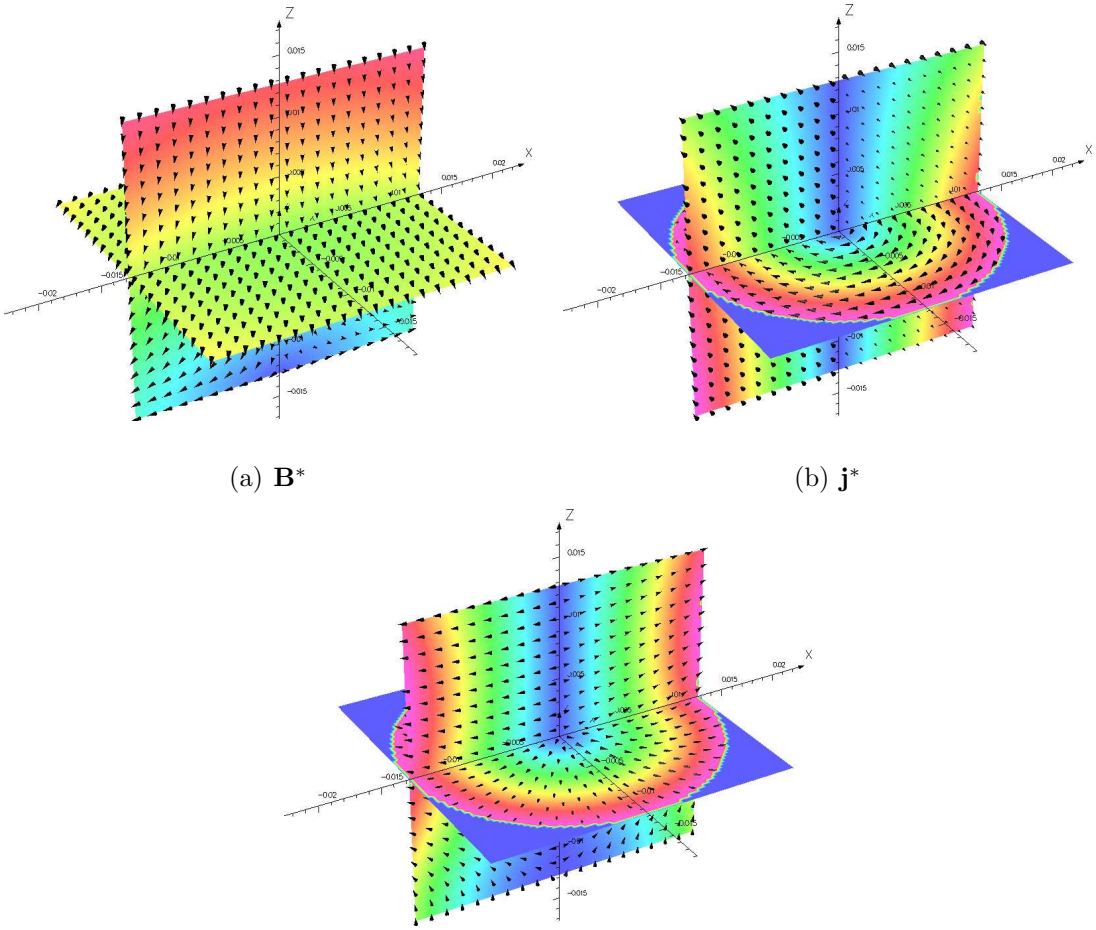

(a) $\mathbf{B}^*$

(b) $\mathbf{j}^*$

(c) $\mathbf{F}^*_{\mathrm{EM}}$

Figure 4.5 : Non-time-averaged fields for the the magnetic flux density, current density, and electromagnetic force with $f^*_{\mathrm{ext}} = 10$ Hz and at 60° of the AC cycle. The arrows denote direction and the color denotes magnitude.

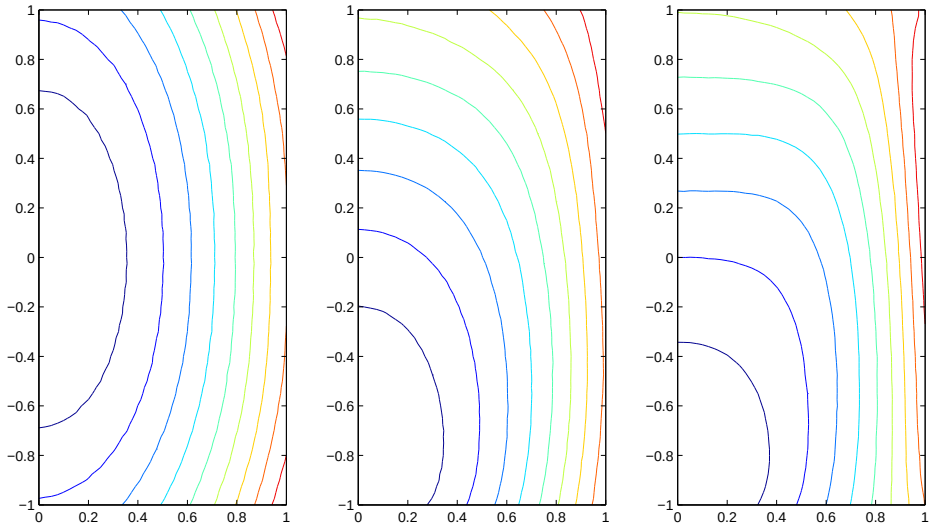

(a) $f^*_{\text{ext}} = 10$ Hz (b) $f^*_{\text{ext}} = 1000$ Hz (c) $f^*_{\text{ext}} = 4000$ Hz

Figure 4.6 : Contours of $\langle B^*_z \rangle$ at different frequencies when external coil current density is held constant. The analytic $\langle B^*_z \rangle$ is constant throughout the melt. The values are normalized such that the max is unity and the minimum is zero. The contours take steps of 0.1. For quantitative comparison, the characteristic magnetic flux densities are a) $B^*_0 = 5.45 \times 10^{-4}$ Tesla, b) $B^*_0 = 5.47 \times 10^{-4}$ Tesla, and c) $B^*_0 = 5.71 \times 10^{-4}$ Tesla.

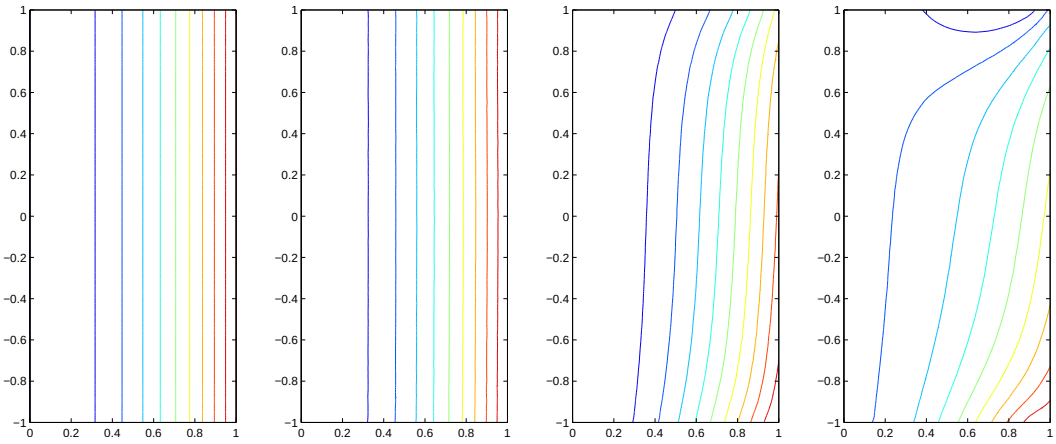

(a) Analytic (b) $f^*_{\text{ext}} = 10$ Hz (c) $f^*_{\text{ext}} = 1000$ Hz (d) $f^*_{\text{ext}} = 4000$ Hz

Figure 4.7 : The analytic azimuthal force contours compared with the numerical azimuthal force at several frequencies. The forces are normalized such that the max is unity and the minimum is zero. The contours take steps of 0.1. The Taylor numbers are b) $Ta_{\text{TMF}} = 3.13 \times 10^1$, c) $Ta_{\text{TMF}} = 3.16 \times 10^4$, and d) $Ta_{\text{TMF}} = 1.38 \times 10^5$.

shape of the radial forces shown in Figure 4.8 is also affected by shielding, being pushed outward as the frequency rises. The more noticeable difference in the radial force is in the magnitude. Table 4.2 shows how the radial and axial forces vary with frequency both at the centerline and over the whole domain. The axial forces at the centerline are compared to the analytic solution, which has a TMF Taylor-normalized maximum value of 0.5.

The table shows that the force at the centerline shows good agreement until $f^*_{\text{ext}} = 2000$ Hz, where it is 7.44% lower than the analytic force. As the shielding becomes greater, the magnitude of the TMF Taylor-normalized axial force continues to decrease at the centerline. The opposite is true for the axial force in the entire domain. The shielding causes the axial Taylor-normalized force to grow to 0.687 at $f^*_{\text{ext}} = 4000$ Hz. For the radial force, shielding causes growth everywhere in the domain. The radial force is expected to be zero at low frequencies and is very near zero

Table 4.2 : Summary of how the maximum forces change with frequency in the entire domain and at the centerline ($z^* = 0$), and how the maximum axial force at the centerline compares to the analytic axial force for low frequency and small wavenumber. All forces here are normalized by the TMF Taylor number.

f^*_{ext} (Hz)	Ta_{TMF}	R_ω	$\langle F_r \rangle_{max}/Ta_{\text{TMF}}$	$\langle F_z \rangle_{max}/Ta_{\text{TMF}}$	$\langle F_r \rangle_{max,z=0}/Ta_{\text{TMF}}$	$\langle F_z \rangle_{max,z=0}/Ta_{\text{TMF}}$	% Error
10	3.13×10^2	1.21×10^{-2}	0.021	0.511	0.004	0.505	1.08
100	3.13×10^3	1.21×10^{-1}	0.038	0.521	0.028	0.505	1.06
500	1.57×10^4	6.06×10^{-1}	0.135	0.562	0.132	0.502	0.48
1000	3.16×10^4	1.21	0.259	0.605	0.258	0.494	-1.23
2000	6.46×10^4	2.43	0.475	0.662	0.471	0.463	-7.44
3000	1.00×10^5	3.64	0.635	0.686	0.620	0.421	-15.8
4000	1.38×10^5	4.85	0.740	0.687	0.707	0.376	-24.8

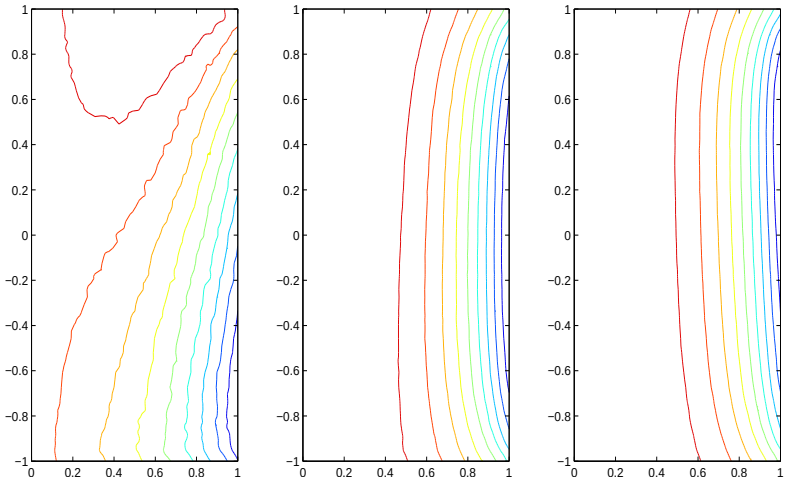

(a) F_r, $f^*_{\text{ext}} = 100$ Hz (b) F_r, $f^*_{\text{ext}} = 1000$ Hz (c) F_r, $f^*_{\text{ext}} = 4000$ Hz

Figure 4.8 : Numerical solutions for the time-averaged radial forces at $f^*_{\text{ext}} = 100$ Hz, $f^*_{\text{ext}} = 1000$ Hz, and $f^*_{\text{ext}} = 4000$ Hz. The forces are normalized so that the maximum is one and the minimum is zero. Steps are taken in increments of 0.1. The maximum values are a) $\langle F_{r,max} \rangle / Ta_{\text{TMF}} = 0.038$, b) $\langle F_{r,max} \rangle / Ta_{\text{TMF}} = 0.259$, and c) $\langle F_{r,max} \rangle / Ta_{\text{TMF}} = 0.740$.

until $f^*_{\text{ext}} = 500$ Hz, where the Taylor-normalized value is 0.135, and this continues to rise to 0.687 at $f^*_{\text{ext}} = 4000$ Hz.

The next two sections show how the differences in the electromagnetic forces cause changes in the base flow and the instabilities that arise.

4.3 TMF Base Flows

In this section, we compare the base flow found through the use of numerical lab forces with that of the base flow found with the analytical force of Grants and Gerbeth [20] for the low frequency, small wavenumber approximation. The magnetic Taylor number was predicted just as it was in Subsection 3.4.1. All laboratory simulations use a value of $k^* = 39.22$ m^{-1} for the dimensional wavenumber, which results in a

nondimensional wavenumber of $k = 0.5$.

4.3.1 Constant External Current Density, Variable Frequency

We first hold the current in the each coil constant at 21.31 A and vary the frequency from $f^*_{\text{ext}} = 10$ Hz to $f^*_{\text{ext}} = 4000$ Hz. Note that this amperage is chosen such that the TMF Taylor number is $Ta_{\text{TMF}} = 1 \times 10^5$ at $f^*_{\text{ext}} = 3000$ Hz. Table 4.3 summarizes the effect the frequency has on the magnetic field and the amount of shielding. R_ω and δ^*_m are defined the same as they were for the RMF case and, as in that case, the shielding effect starts impacting B^*_0 at $f^*_{\text{ext}} = 2000$ Hz and the effect gets stronger as the frequency grows.

Table 4.3 : AC-frequency related quantities of the GaInSb cylindrical melt (calculations based on melt properties in Table 4.1) for a constant exteral coil current of 21.31 A.

f^*_{ext} (Hz)	$B^*_0 \times 10^4$ (Tesla)	Ta_{TMF}	R_ω	δ^*_m (m)
10	5.45	3.13×10^2	1.21×10^{-2}	1.64×10^{-1}
100	5.45	3.13×10^3	1.21×10^{-1}	5.18×10^{-2}
500	5.45	1.57×10^4	6.06×10^{-1}	2.32×10^{-2}
1000	5.47	3.16×10^4	1.21	1.64×10^{-2}
2000	5.53	6.46×10^4	2.43	1.16×10^{-2}
3000	5.62	1.00×10^5	3.64	9.45×10^{-3}
4000	5.71	1.38×10^5	4.85	8.19×10^{-3}

Figure 4.9 – Figure 4.11 show the contours of the base flow velocities and pressure for the both the analytical and numerical lab forcing simulations as the frequency

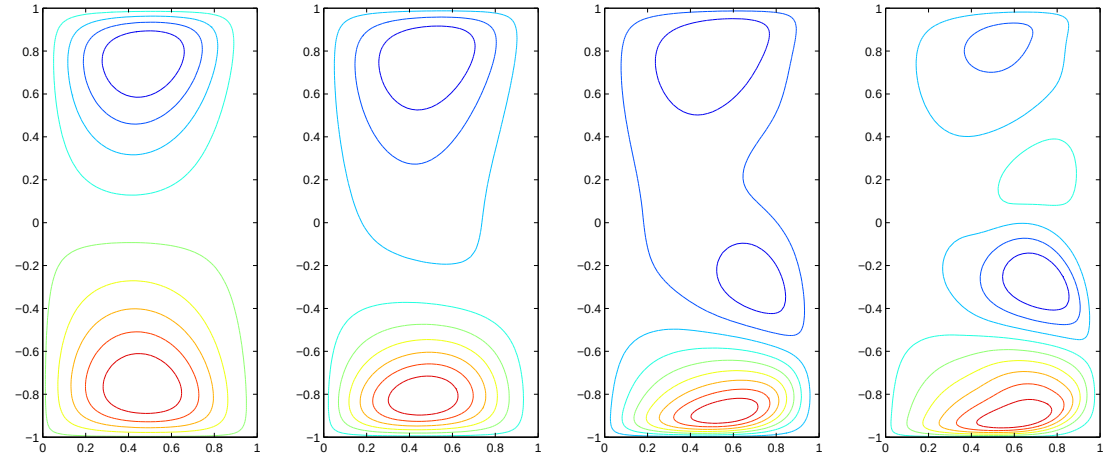

(a) $v_{r_{\text{analytic}}}$ $Ta_{\text{TMF}} = 3.13 \times 10^2$

(b) $v_{r_{\text{analytic}}}$ $Ta_{\text{TMF}} = 3.13 \times 10^3$

(c) $v_{r_{\text{analytic}}}$ $Ta_{\text{TMF}} = 3.16 \times 10^4$

(d) $v_{r_{\text{analytic}}}$ $Ta_{\text{TMF}} = 1.38 \times 10^5$

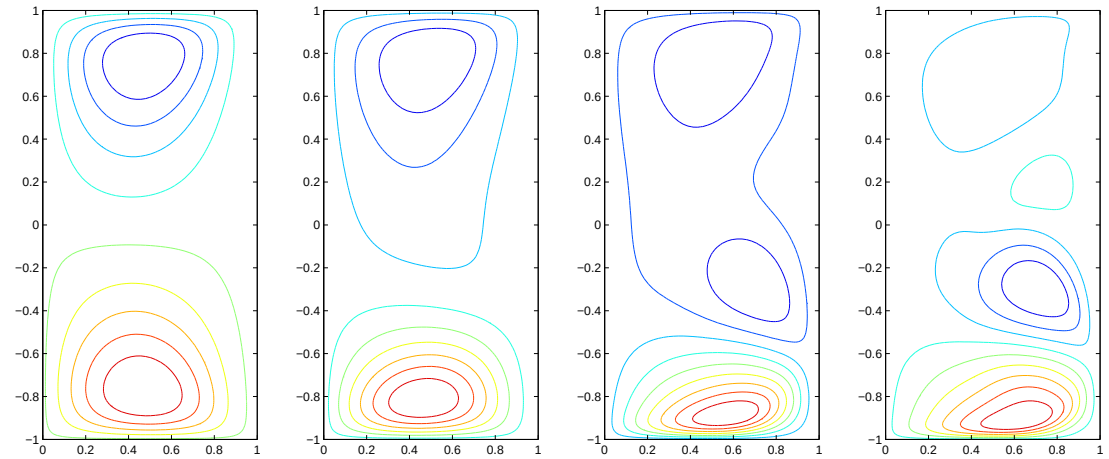

(e) $v_{\text{lab},r}$ $f^*_{\text{ext}} = 1$ Hz $Ta_{\text{TMF}} = 3.13 \times 10^2$

(f) $v_{\text{lab},r}$ $f^*_{\text{ext}} = 100$ Hz $Ta_{\text{TMF}} = 3.13 \times 10^3$

(g) $v_{\text{lab},r}$ $f^*_{\text{ext}} = 1000$ Hz $Ta_{\text{TMF}} = 3.16 \times 10^4$

(h) $v_{\text{lab},r}$ $f^*_{\text{ext}} = 4000$ Hz $Ta_{\text{TMF}} = 1.38 \times 10^5$

Figure 4.9 : The base flow radial velocity contours using analytic (a-d) and numerical lab (e-h) forces at various frequencies. All fields shown are normalized such that the minimum is zero and the maximum is one. Contour steps are taken in increments of 0.1. The maximum values are a) $v_{r,max} = 8.49 \times 10^{-1}$, b) $v_{r,max} = 1.10 \times 10^1$, c) $v_{r,max} = 9.88 \times 10^1$, d) $v_{r,max} = 2.83 \times 10^2$, e) $v_{r,max} = 8.52 \times 10^{-1}$, f) $v_{r,max} = 1.10 \times 10^1$, g) $v_{r,max} = 9.88 \times 10^1$, and h) $v_{r,max} = 2.39 \times 10^2$.

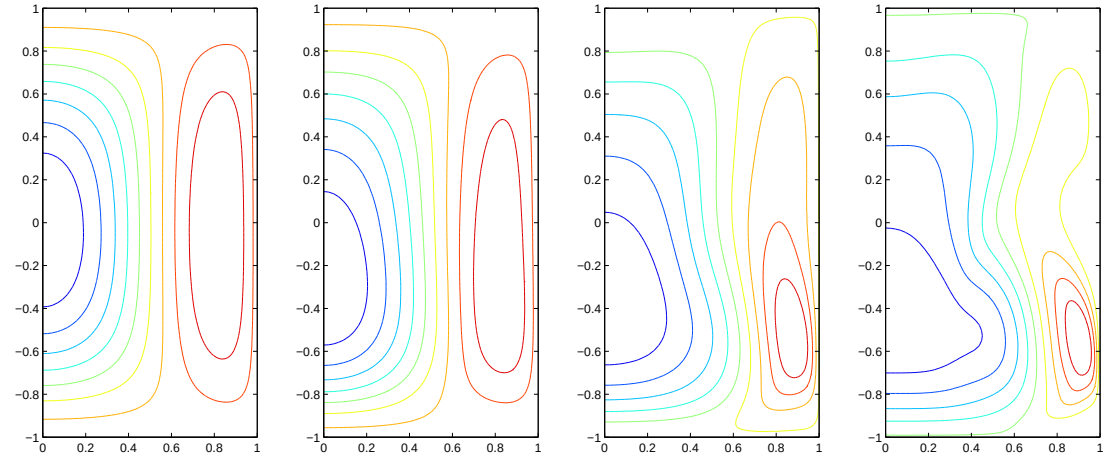

(a) $v_{z_{\text{analytic}}}$ $Ta_{\text{TMF}} = 3.13 \times 10^2$

(b) $v_{z_{\text{analytic}}}$ $Ta_{\text{TMF}} = 3.13 \times 10^3$

(c) $v_{z_{\text{analytic}}}$ $Ta_{\text{TMF}} = 3.16 \times 10^4$

(d) $v_{z_{\text{analytic}}}$ $Ta_{\text{TMF}} = 1.38 \times 10^5$

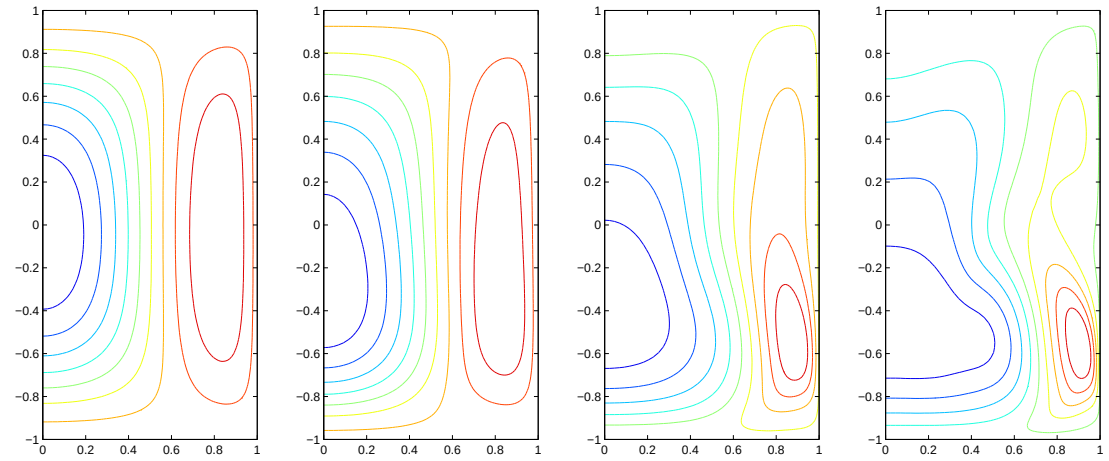

(e) $v_{\text{lab},z}$ $f^*_{\text{ext}} = 1$ Hz $Ta_{\text{TMF}} = 3.13 \times 10^2$

(f) $v_{\text{lab},z}$ $f^*_{\text{ext}} = 100$ Hz $Ta_{\text{TMF}} = 3.13 \times 10^3$

(g) $v_{\text{lab},z}$ $f^*_{\text{ext}} = 1000$ Hz $Ta_{\text{TMF}} = 3.16 \times 10^4$

(h) $v_{\text{lab},z}$ $f^*_{\text{ext}} = 4000$ Hz $Ta_{\text{TMF}} = 1.38 \times 10^5$

Figure 4.10 : The base flow axial velocity contours using analytic (a-d) and numerical lab (e-h) forces at various frequencies. All fields shown are normalized such that the minimum is zero and the maximum is one. Contour steps are taken in increments of 0.1. The maximum values are a) $v_{z,max} = 2.95 \times 10^0$, b) $v_{z,max} = 2.62 \times 10^1$, c) $v_{z,max} = 1.39 \times 10^2$, d) $v_{z,max} = 3.29 \times 10^2$, e) $v_{z,max} = 2.94 \times 10^0$, f) $v_{z,max} = 2.62 \times 10^1$, g) $v_{z,max} = 1.35 \times 10^2$, and h) $v_{z,max} = 2.72 \times 10^2$.

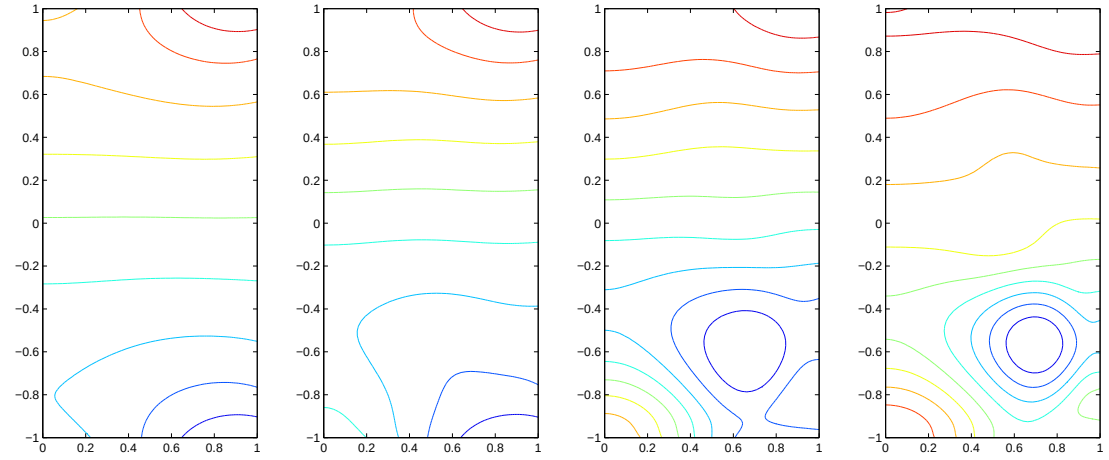

(a) p_{analytic} $Ta_{\text{TMF}} = 3.13 \times 10^2$

(b) p_{analytic} $Ta_{\text{TMF}} = 3.13 \times 10^3$

(c) p_{analytic} $Ta_{\text{TMF}} = 3.16 \times 10^4$

(d) p_{analytic} $Ta_{\text{TMF}} = 1.38 \times 10^5$

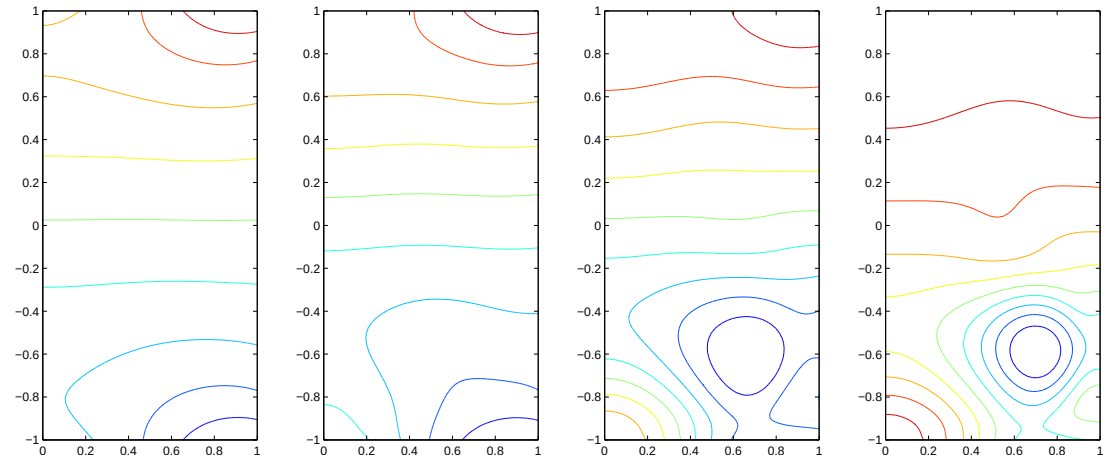

(e) p_{lab} $f^*_{\text{ext}} = 1$ Hz $Ta_{\text{TMF}} = 3.13 \times 10^2$

(f) p_{lab} $f^*_{\text{ext}} = 100$ Hz $Ta_{\text{TMF}} = 3.13 \times 10^3$

(g) p_{lab} $f^*_{\text{ext}} = 1000$ Hz $Ta_{\text{TMF}} = 3.16 \times 10^4$

(h) p_{lab} $f^*_{\text{ext}} = 4000$ Hz $Ta_{\text{TMF}} = 1.38 \times 10^5$

Figure 4.11 : The base flow pressure contours using analytic (a-d) and numerical lab (e-h) forces at various frequencies. All fields shown are normalized such that the minimum is zero and the maximum is one. Contour steps are taken in increments of 0.1. The maximum values are a) $p_{max} = 1.06 \times 10^2$, b) $p_{max} = 1.14 \times 10^3$, c) $p_{max} = 1.59 \times 10^4$, d) $p_{max} = 1.17 \times 10^5$, e) $p_{max} = 1.06 \times 10^{-2}$, f) $p_{max} = 1.14 \times 10^3$, g) $p_{max} = 1.53 \times 10^4$, and h) $p_{max} = 7.78 \times 10^4$.

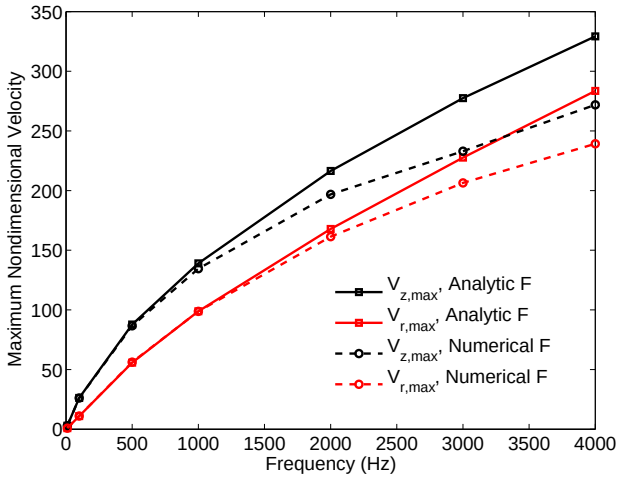

Figure 4.12 : The maximum lab velocity components as a function of frequency compared to the maximum velocity components of from the solution using the analytic forcing function. Note that the analytic solution used the magnetic Taylor number found in each numerical lab case since it does not depend on frequency. Also, the azimuthal velocity is not shown as it is zero in each case.

grows. For the analytical case, there is not a frequency involved since a low frequency approximation is assumed. As was done for the RMF cases, the TMF magnetic Taylor numbers are matched for the analytically-forced simulations.

As the frequency increases, we can see from the contours that the boundary layer at $z = -1$ gets much thinner as most of the radial flow component gets forced to the bottom of the domain. This strong radial component near the bottom wall also has an impact on the axial velocity, which gets pushed outward radially in the lower half of the domain as the frequency grows. There is no flow moving in the azimuthal direction in either case. In all cases, the numerical lab-forced base flow appears to match the analytically-forced base flow well with only a small variation in shape noticeable at $f^*_{\text{ext}} = 4000$ Hz. As with the RMF flow simulations, the shape of the flow field does not significantly change as the frequency increases, but the magnitude is greatly affected. Figure 4.12 shows how the radial and axial flow component maximum values change

with frequency. For both components, there is good agreement at low frequencies as expected, but the numerical lab-forced velocities begins to drop much lower than the analytically-forced values. By $f^*_{\text{ext}} = 4000$ Hz, the axial velocity is 17.4% lower and the radial velocity is 15.6% lower than the analytic case.

4.3.2 Constant $Ta_{\mathbf{TMF}} = 1.0 \times 10^5$, Variable Frequency

In this subsection, the Taylor number is held constant at $Ta_{TMF} = 1.0 \times 10^5$ while the frequency varies from $f^*_{\text{ext}} = 10$ Hz to $f^*_{\text{ext}} = 4000$ Hz. This means the current in the external coils changes to alter the magnitude of the magnetic flux density to counteract the growing frequency in an effort to keep the TMF Taylor number constant Again, the magnetic Taylor number was selected based on the method discussed in Subsection 3.4.1.

The shielding parameter and magnetic skin depth are the same here as they were in the previous section as the physical parameters and the frequency range are the same. The electromagnetic property that does change is the magnitude of $\langle \mathbf{B}^* \rangle$. For the traveling field, the maximum axial component of the magnetic field along the centerline is monitored and used in computing a TMF Taylor number. Figure 4.13 shows how the time-averaged axial component of the magnetic flux density changes with frequency through the maximum and minimum values throughout the domain. Figure 4.14 shows how the current in each coil must be dropped in order to get the desired B^*_0 to keep the TMF Taylor number constant. The two figures have a similar shape as there is a linear relationship between B^*_0 and j^*_{coil}.

Figures 4.15 - 4.17 show how the base flow changes as the frequency increases and how this compares to the low frequency, low wavenumber analytically-forced base flow. As expected, there is very little difference at low frequencies. At $f^*_{\text{ext}} = 100$

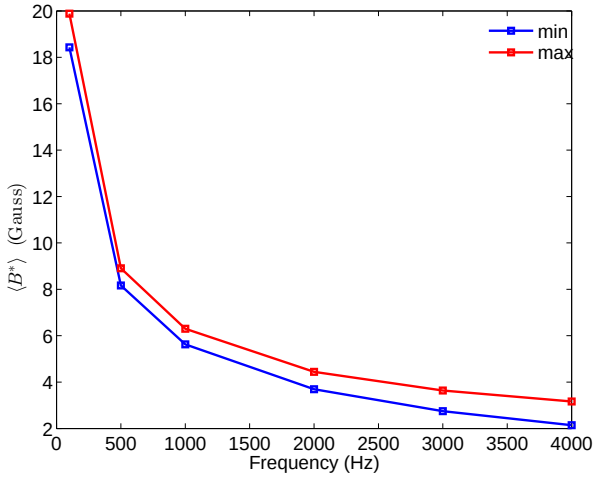

Figure 4.13 : The maximum and minimum time-averaged axial component of the magnetic flux density across the domain vs the frequency for $Ta_{\mathrm{TMF}} = 1.0 \times 10^5$.

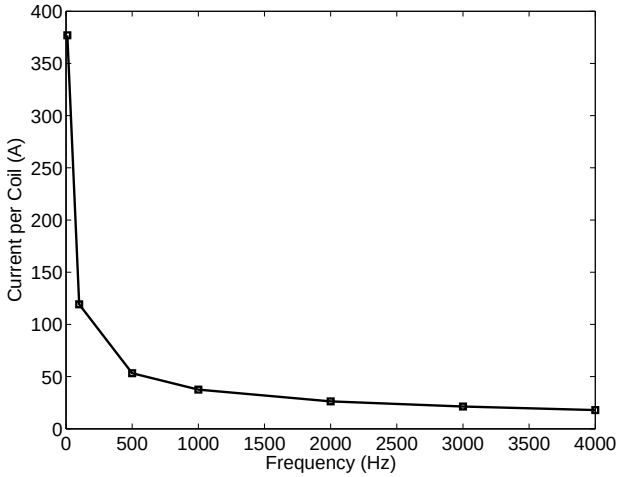

Figure 4.14 : The current applied in each coil vs the frequency to ensure $Ta_{\mathrm{TMF}} = 1.0 \times 10^5$.

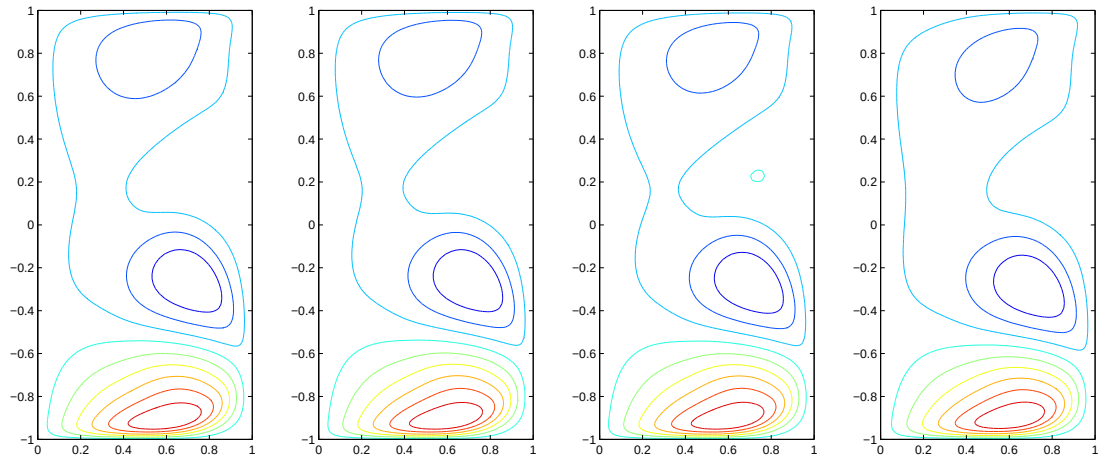

(a) v_r, Analytic (b) v_r, 100 Hz (c) v_r, 1000 Hz (d) v_r, 4000 Hz

Figure 4.15 : The analytic base flow radial velocity contours compared to those found using numerical lab forces at various frequencies for $Ta_{\mathrm{TMF}} = 1.0 \times 10^5$. All fields shown are normalized such that the minimum is zero and the maximum is one. Contour steps are taken in increments of 0.1. The maximum values are a) $v_{r,max} = 2.27 \times 10^2$, b) $v_{r,max} = 2.29 \times 10^2$, c) $v_{r,max} = 2.27 \times 10^2$, and d) $v_{r,max} = 1.92 \times 10^2$.

Hz, the base flow contours are very similar to those for the analytic case and at $f^*_{\mathrm{ext}} = 1000$ Hz, they are also nearly the same, but it is easy to see a change in the pressure contours near the top of the domain. At $f^*_{\mathrm{ext}} = 4000$ Hz, the radial velocity contours are still very much the same, though small differences do exist, while the axial velocity contour lines have been noticeably forced downward near the axis. The pressure contour change is quite obvious as the contour lines in the upper half of the domain move downward and the pressure levels out.

Again, the most significant difference in the flow field as the frequency increases is not in its shape, but in the magnitude of the velocity components. Figure 4.18 shows how the axial and radial velocities vary with frequency and how that compares to the value found through analytic forcing. At low frequencies, the lab velocity overshoots slightly, but drops off dramatically as the frequency increases. This is especially true

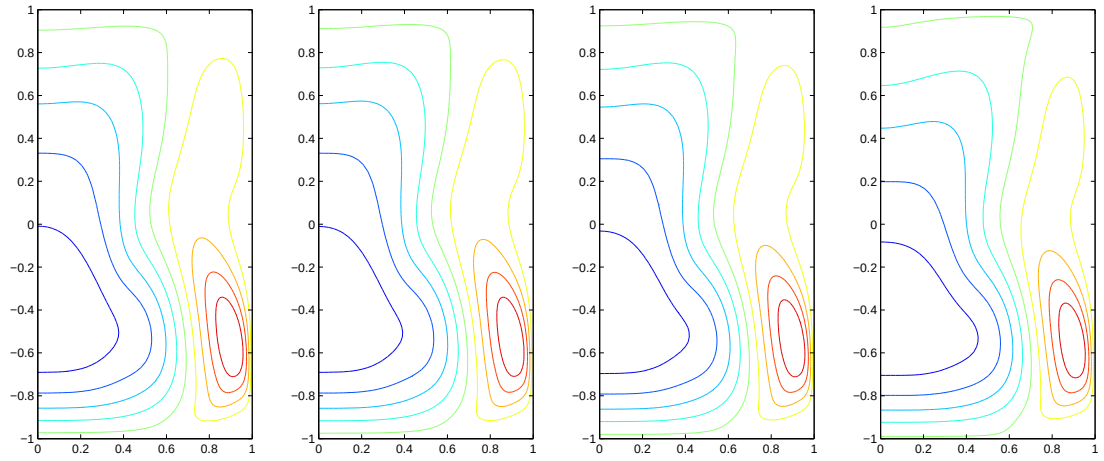

(a) v_z, Analytic (b) v_z, 100 Hz (c) v_z, 1000 Hz (d) v_z, 4000 Hz

Figure 4.16 : The analytic base flow axial velocity contours compared to those found using numerical lab forces at various frequencies for $Ta_{\text{TMF}} = 1.0 \times 10^5$. All fields shown are normalized such that the minimum is zero and the maximum is one. Contour steps are taken in increments of 0.1. The maximum values are a) $v_{z,max} = 2.78 \times 10^2$, b) $v_{z,max} = 2.77 \times 10^2$, c) $v_{z,max} = 2.68 \times 10^2$, and d) $v_{z,max} = 2.14 \times 10^2$.

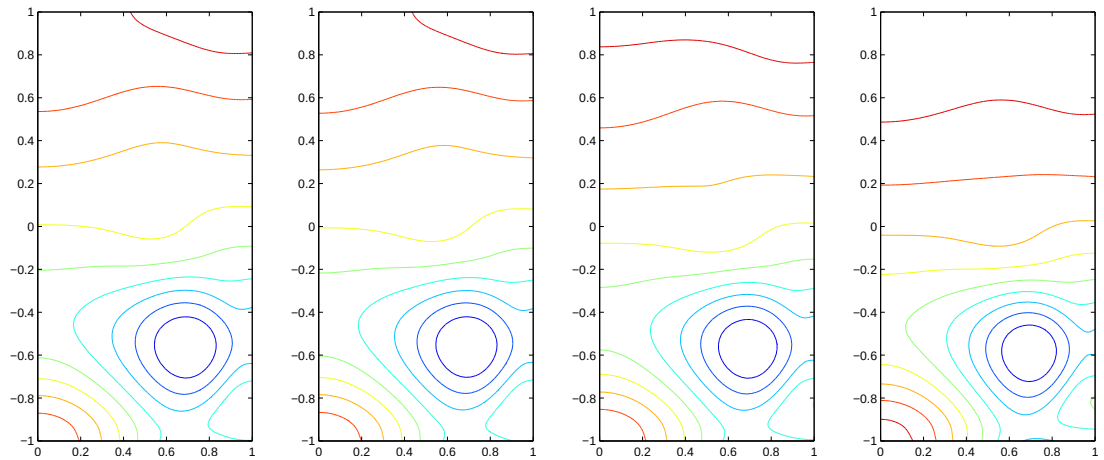

(a) p, Analytic (b) p, 100 Hz (c) p, 1000 Hz (d) p, 4000 Hz

Figure 4.17 : The analytic base flow pressure contours compared to those found using numerical lab forces at various frequencies for $Ta_{\text{TMF}} = 1.0 \times 10^5$. All fields shown are normalized such that the minimum is zero and the maximum is one. Contour steps are taken in increments of 0.1. The maximum values are a) $p_{max} = 7.57 \times 10^4$, b) $p_{max} = 7.65 \times 10^4$, c) $p_{max} = 7.42 \times 10^4$, and d) $p_{max} = 4.95 \times 10^4$.

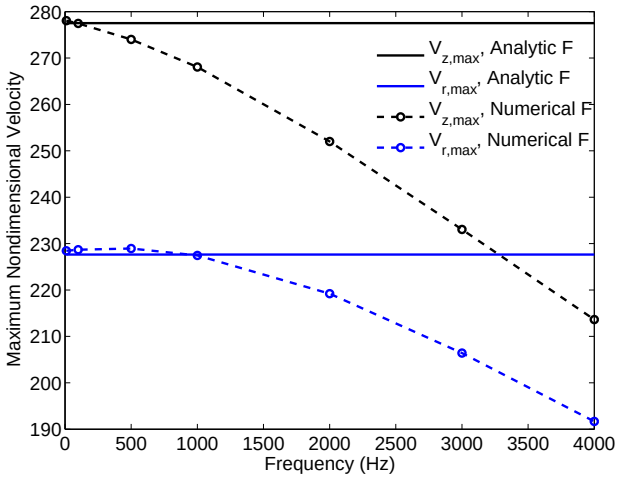

Figure 4.18 : The maximum velocity components as a function of frequency compared to the maximum velocity components of from the solution using the analytic forcing function.

for the axial velocity. At $f^*_{\text{ext}} = 10$ Hz, the radial and axial velocities overshoot by 0.35% and 0.20%, respectively, and at $f^*_{\text{ext}} = 4000$ Hz, the undershoot is as high as 15.81% and 23.02%.

4.4 Instabilities in TMF Driven Flow

Instabilities predicted by time-dependent, three-dimensional simulations are compared to predictions from linear stability theory. First, instabilities are investigated when the analytic forcing is used. Then, lab TMF forcing is applied to determine the impact of these more realistic EM body forces.

4.4.1 Small Wavenumber, Low Frequency Analytic Force

In the case where the wavenumber is small and the low frequency approximation applies, the resulting time-averaged force has only an axial component and can be

expressed as

$$F_z = \frac{1}{2} Ta_{\mathrm{RMF}} r^2. \tag{4.24}$$

This force was derived in Section 4.2.2. This expression was used in linear stability analysis by Grants and Gerbeth [27] and in a study by Gelfgat [31]. As a preliminary check, we also simulate the flow using this forcing function.

The values chosen for simulation hovered around the expected point of instability of $Ta^{cr}_{\mathrm{TMF}} = 1.2044 \times 10^5$ found by Grants and Gerbeth and $Ta^{cr}_{\mathrm{TMF}} = 1.2042 \times 10^5$ found by Gelfgat. The four simulations were for $Ta_{\mathrm{TMF}} \times 10^{-5} = 1.15,\ 1.19,\ 1.21,\ 1.25$. In each case, the flow was computed axisymmetrically with the force ramped linearly between $t = 0$ and $t = 1$, and held constant for $t > 1$. As was done in the RMF case, the axisymmetric flow is first simulated to a steady state and then expanded in the azimuthal direction via Fourier modes. This base flow is then perturbed randomly with a Gaussian distribution with a standard deviation of 0.1% of the axial velocity, which is chosen because it is the dominant velocity component. The flow simulation is restarted from the perturbed base state and the energy is monitored for signs of growth or decay.

Figure 4.19 shows the energy in modes 0 – 3 for the $Ta_{\mathrm{TMF}} = 1.15 \times 10^5$ and $Ta_{\mathrm{TMF}} = 1.25 \times 10^5$ cases. As expected, the $Ta_{\mathrm{TMF}} = 1.15 \times 10^5$ simulation found that all modes decayed in time, with the $m = 3$ mode have the smallest decay rate as might be expected from linear stability theory. The energies at $Ta_{\mathrm{TMF}} = 1.25 \times 10^5$, on the other hand, do indicate the presence of an instability. Initially, all modes decay except for the $m = 3$, which grows exponentially. Unexpectedly, the modes that initially decay do not completely vanish and instead, begin growing as well. All modes saturate at a non-neglible value, but the $m = 3$ mode is the dominant mode. The saturation energies for modes 1 – 3 are 1.0×10^{-2}, 0.51, and 29.1, respectively.

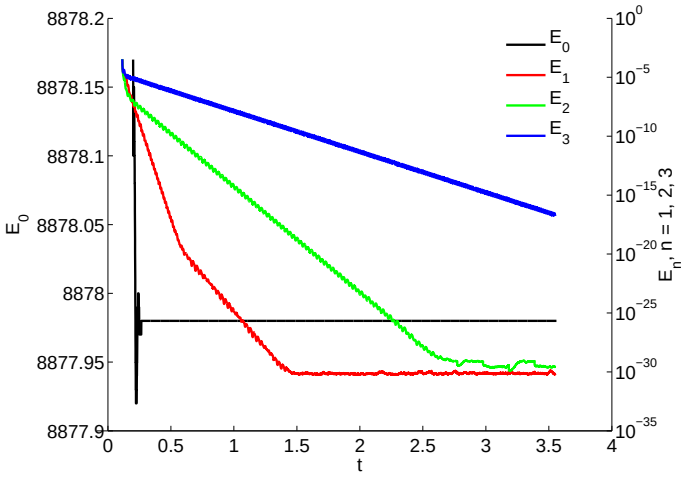

(a) $Ta_{\mathrm{TMF}} = 1.15 \times 10^5$

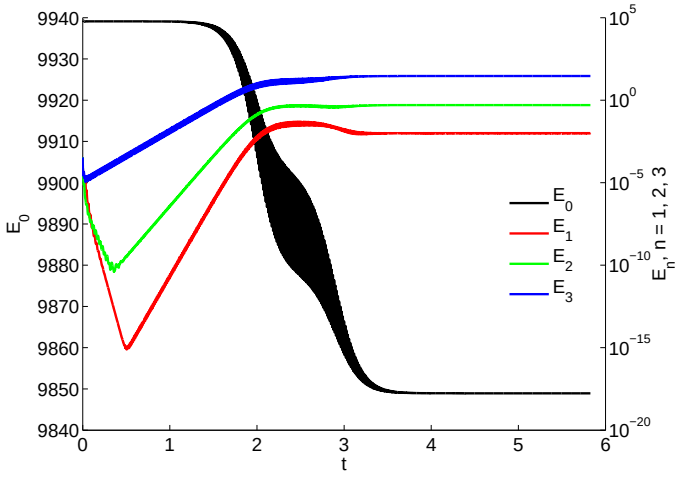

(b) $Ta_{\mathrm{TMF}} = 1.25 \times 10^5$

Figure 4.19 : Energy in modes $0 - 3$ in time for the a) $Ta_{\mathrm{TMF}} = 1.15 \times 10^5$ and b) $Ta_{\mathrm{TMF}} = 1.25 \times 10^5$ simulations with the analytic body force. For (a), all perturbations decay in time, indicating stability. For (b), all modes > 0 eventually grow and saturate with the $m = 3$ mode being most dominant.

Table 4.4 shows the results via the growth and decay rates for the four different simulations as well as the interpolated critical Taylor number. The interpolation was done using the values at $Ta_{\text{TMF}} = 1.19 \times 10^5$ and $Ta_{\text{TMF}} = 1.21 \times 10^5$. The value of $Ta^{cr}_{\text{TMF}} = 1.2042 \times 10^5$ exactly matches the value found by Gelfgat.

$Ta_{\text{TMF}} \times 10^{-5}$	1.15	1.19	1.2042	1.21	1.25
Growth/Decay Rate	-8.14	-2.13	0.0000	0.87	7.04

Table 4.4 : The growth and decay rates for the four cases run with the small wavenumber, low frequency, analytic body force as well as the interpolated Ta_{TMF} at the point of marginal stability. Note that decay rates are negative and growth rates are positive. The interpolated value of $Ta^{cr}_{\text{TMF}} = 1.2042 \times 10^5$ matches up exactly with that found by Gelfgat [31].

4.4.2 Three-dimensional Instabilities with Laboratory EM Body Forces

Next, the focus shifts to finding instabilities using the laboratory forces, which were shown in Subsection 4.2.3. The instabilities are expected to be near the critical TMF Taylor number in the low frequency, small wavenumber approximation case of the last section, $Ta^{cr}_{\text{TMF}} = 1.2042 \times 10^5$. The goal here is to find the instabilities and note the changes in both the value of the critical TMF Taylor number and the flow physics. To find the critical points, we first simulate at $Ta_{\text{TMF}} = 1.20 \times 10^5$ and $Ta_{\text{TMF}} = 1.30 \times 10^5$. Growth and decay rates can be pulled from these simulations and linear interpolation can be used to approximate the point of instability, where further simulations can be run.

The $Ta_{TMF} = 1.20 \times 10^5$ cases are all expected to be stable since they are below the expected point of instability. However, this is not the case. Figure 4.4.2 shows how

the energy in the $m = 3$ mode varies over time for each of the different frequencies. All other modes, while not shown, decay in time and do so much more quickly than the $m = 3$ mode as expected from linear stability results. From the figure, we can see that the decay rate increases as the frequency grows, but at the lower frequencies, the $m = 3$ mode does not decay at all. Figure 4.20(b) shows a similar plot for $Ta_{\mathrm{TMF}} = 1.3 \times 10^5$. At $Ta_{\mathrm{TMF}} = 1.3 \times 10^5$, the $m = 3$ mode is expected to be the dominant mode with non-zero energy. This behavior is seen until $f^*_{\mathrm{ext}} \geq 3000$ Hz, where the $m = 3$ mode decays to zero in time.

Finally, we look at how the unstable mode compares to that of linear stability theory. Figure 4.21 shows contours of the perturbation velocity magnitude in an r-z section and the axial perturbation velocity at $z = -0.454$ for a frequency of $f^*_{\mathrm{ext}} = 10$ Hz and $Ta_{\mathrm{TMF}} = 1.18 \times 10^5$. The perturbation velocity contours in the $r - z$ plane where v'_z is maximum are only a decent match for the contours from linear stability theory, showing that there are some differences between analytic and laboratory results. The axial perturbation velocity contours show the existence of the $m = 3$ mode, which matches decently well with that of linear stability theory.

Using the growth and decay rates, values of the critical TMF Taylor number can be estimated. These estimates are used to predict new upper and lower bounds at which simulations can be run and then the estimate can be updated until the critical point is bounded within a region of size 0.01×10^5. Table 4.5 shows the values of the upper and lower bounds and their corresponding growth and decay rates. Note that unlike in the RMF case, all growth and decay rates can be found because there is no initial stochastic region for the TMF simulations. The table also shows the predicted point of instability using the growth/decay rates from the upper/lower bounds. Figure 4.22 shows a plot of the estimated critical point as the frequency increases. Just as in the

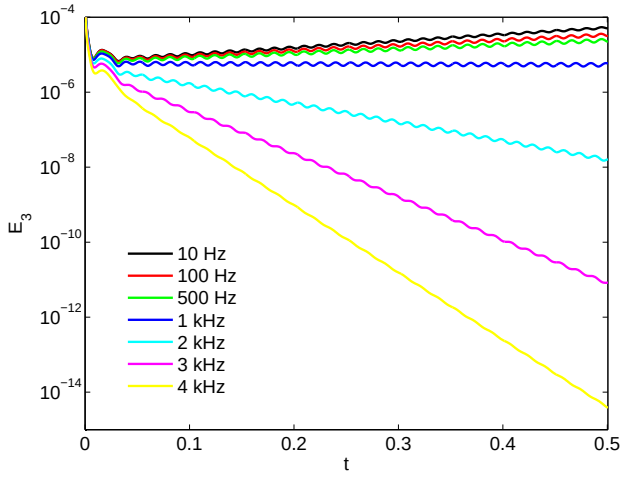

(a)

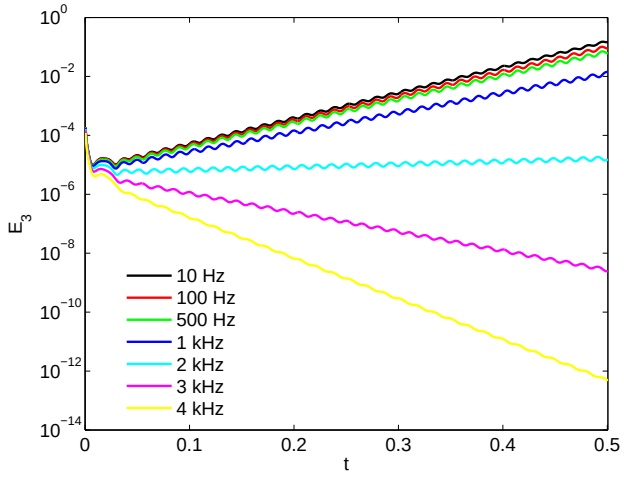

(b)

Figure 4.20 : The energy in the $m = 3$ mode in time for each different frequency at $Ta_{\mathrm{TMF}} = 1.2 \times 10^5$ and $Ta_{\mathrm{TMF}} = 1.3 \times 10^5$. The decay rate increases/growth rate decreases as the frequency increases in each case.

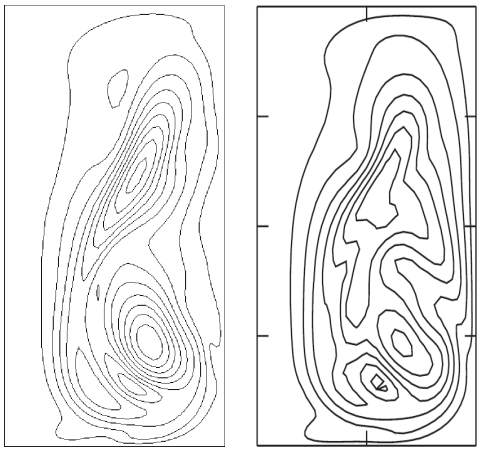

(a) $\|\mathbf{v}'\|$, 3D simulations

(b) $\|\mathbf{v}'\|$, Linear Stability

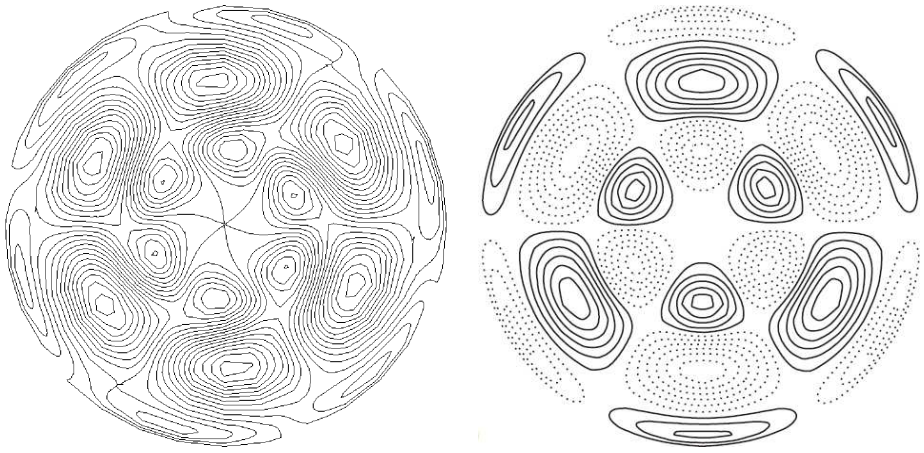

(c) v_z', 3D Simulations

(d) v_z', Linear Stability

Figure 4.21 : The perturbation velocity magnitude contours in the r-z plane comparing 3D simulation results to those from linear stability theory and the axial perturbation velocity contours at $z = -0.454$ for simulations and linear stability theory. The frequency is $f^* = 10$ Hz, and the TMF Taylor number is $Ta_{\mathrm{TMF}} = 1.18 \times 10^5$.

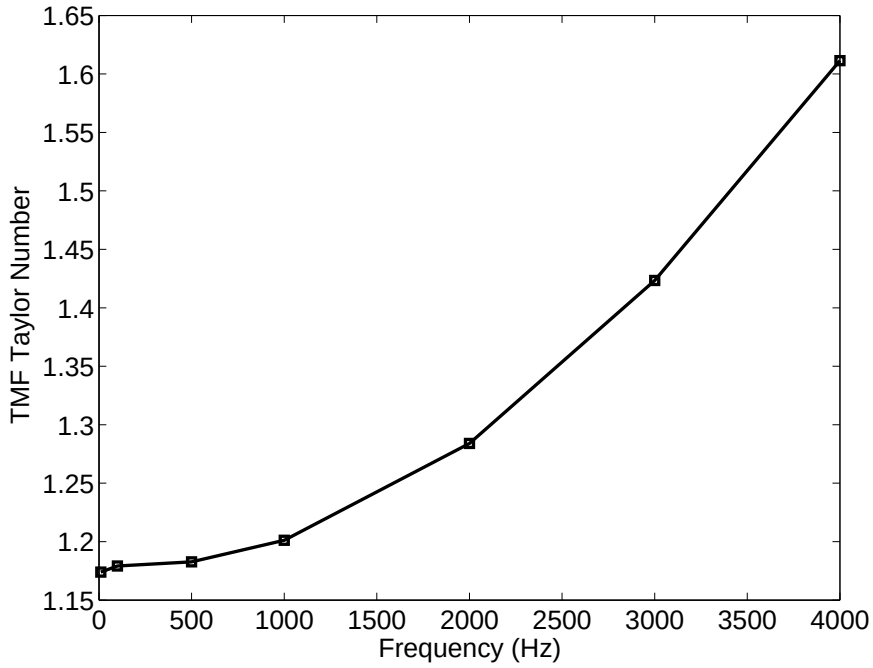

Figure 4.22 : The estimated critical TMF Taylor number for different frequencies.

RMF case, the shielding effect results in decreased forces, which then causes a drop in the velocity. This raises Ta^{cr}_{TMF}.

4.5 TMF Conclusions

The objectives of this chapter were similar to those of the previous except that a traveling magnetic field was used instead of a rotating magnetic field. Comparisons were made between theoretical and laboratory force fields. The effects this had on the base flow and instabilities was explored. The low frequency, low wavenumber solutions were used for comparison as has been done in other studies.

Unlike in the RMF case, the force fields in the TMF case vary greatly with increasing frequency. The time-averaged axial force is theoretically only a function of r^*, which is well-approximated by the low frequency laboratory forces. As the fre-

Frequency (Hz)	$Ta^{l}_{\mathrm{TMF}} \times 10^{-5}$	Decay Rate	$Ta^{u}_{\mathrm{TMF}} \times 10^{-5}$	Growth Rate	$Ta^{cr}_{\mathrm{TMF}} \times 10^{-5}$
10	1.170	0.604	1.180	0.929	1.1739
100	1.175	0.649	1.185	0.915	1.1791
500	1.180	0.415	1.190	1.121	1.1827
1000	1.200	0.169	1.210	1.335	1.2011
2000	1.280	0.555	1.290	0.846	1.2840
3000	1.415	1.143	1.425	0.226	1.4233
4000	1.610	0.141	1.620	0.855	1.6114

Table 4.5 : The upper and lower bounds on the critical TMF Taylor number for frequencies 10 Hz $\leq f^{*} \leq$ 4000 Hz with the corresponding growth and decay rates. The last column is the Ta^{cr}_{TMF} predicted through linear interpolation.

quency increases, the force becomes skewed such that a clear z^* dependence forms. The maximum lab force at the centerline drops markedly while the radial force grows significantly, eventually reaching the same order of magnitude as the axial force.

The drop in forces translates to the base flow as expected, by lowering the maximum velocities. Overall, the contours of the flow field appear to be very qualitatively similar for the analytically-forced flow and the laboratory-forced flow despite the significant differences in the force fields. Quantitative differences result from the change in magnitude of the lab force with frequency.

We then looked at the three-dimensional instabilities, paying close attention to the $m = 3$ mode since it was expected to be the dominant unstable mode as found through linear stability analyses. The $m = 3$ did, in fact, present as the dominant mode for all simulations above Ta^{cr}_{TMF} using both the analytic and laboratory forces. Flow field perturbations compared reasonably well with the eigenfunctions of linear stability theory. No stochastic regions appeared in the TMF simulations so growth and decay rates were easily computed from changes in modal energies. These rates were then used to predict the estimated point of instability through linear interpolation. In the case with analytic forces, the predicted critical TMF Taylor number agreed with that of Gelfgat [31] to 4 decimal places and good agreement was found in the critical frequency as well. For the numerical forces, the relationship of the critical Taylor number versus frequency was similar to that of the RMF case. Good agreement with the expected value is seen at low frequencies, but there is a strong divergence between the analytical and laboratory critical values as the frequency grows.

Chapter 5

Conclusion

The goal of the study was to analyze instabilities in a crystal growth melt paying close attention to the differences in solutions obtained through the use of analytic forces and through numerical lab forces that more closely approximate the laboratory configuration. Overall, linear stability is shown to be a good predictor of mode numbers and qualitative perturbation flow for both the RMF and TMF driven flow. However, the quantitative values of critical magnetic Taylor numbers and perturbation velocities deviate significantly as shielding becomes important.

5.1 RMF

For the RMF case, the difference in analytic and laboratory forces was subtle, but the resulting effect on the flow instabilities was quite significant. For analytic forces, the axisymmetric study confirmed the results of linear stability theory and served as validation of the flow solver's ability to capture such instabilities. The analytic forces applied to three-dimensional simulations also accurately bounded the point of instability and found linear instabilities for a magnetic Taylor number just above the critical point ($Ta_m = 1.24 \times 10^5$). As predicted by linear stability theory, the $m = 2$ symmetric mode grows and saturates in time. For simulations with higher Taylor numbers, the flow was characterized by alternating flow regimes – one stochastic region featuring Taylor-Görtler vortices and one linear region with the

$m = 2$ symmetric mode growing, but transitioning back to the stochastic region before saturating.

Using the laboratory forces resulted in different behavior. Above the critical magnetic Taylor number, the flow first enters a stochastic regime after being perturbed by random noise. It then transitions to the linear flow regime, but instead of returning to the stochastic flow, the linear mode with the lab forces saturates. Tests run to determine the cause of the failure to transition to the nonlinear flow found that the nonzero radial and axial forces were not significant, but instead, the small changes in azimuthal force were responsible for the change in the type of instability that presents.

Additionally, the laboratory forces account for frequency, which is assumed to be very small in the analytic case. The frequency proved to have a measurable stabilizing impact on the flow field. For low frequencies, the critical Taylor number for laboratory-forced flow was close to that of analytically-forced flow. However, as the frequency was increased, the critical Taylor number grew as well. At a frequency of $f^*_{\text{ext}} = 4000$ Hz, the upper bound on the critical value was $Ta^{cr}_m = 1.92 \times 10^5$, a value 55.8% higher than the value predicted by linear stability theory in the low frequency approximation.

Overall, this study for the RMF shows the importance of using forces closer to those found in experiments. While the critical points agreed well for low frequencies as expected, the type of instability that dominated the flow was different between the two cases. For high frequencies where the theory is no longer valid, the laboratory forces must be used as they account for the shielding effect that comes with high external frequencies for the rotating magnetic field.

5.2 TMF

The TMF case is similar to the RMF case in that it highlights the importance of using laboratory forces beyond the low frequency approximation. Unlike the RMF case, the force field computed through simulations was noticeably different from the analytic forces.

Using the analytic forces, the critical TMF Taylor number was bounded, and because the flow does not have any stochastic regions as were present in the RMF case, the growth and decay rates were easily computed from the modal energies. With these rates, an estimated critical TMF Taylor number was found through linear interpolation and the resulting value matched very well with previous linear stability studies for low frequency and small wavenumber. The $m = 3$ mode was the dominant mode, but unexpectedly not the only mode to grow. Once the $m = 3$ mode grew while the others decayed, the flow transitioned to a region where all modes grew and eventually saturated. The $m = 3$ mode saturated at a much higher energy than the other modes so that the final flow field perturbations appear to have predominantly a $m = 3$ shape.

The numerical lab forces found similar results for all cases, but the critical points deviated from the predicted value as the frequency grew. Much like in the RMF case, the critical values at low frequencies matched well with the predictions from linear stability theory in the low frequency approximation, but increases in frequency had a stabilizing effect on the flow. At a frequency of $f^*_{\text{ext}} = 4000$ Hz, the critical TMF Taylor number was estimated to be $Ta_{\text{TMF}} = 1.6114 \times 10^5$, which is 33.8% higher than the value predicted by linear stability theory. Thus, the laboratory forces must be used beyond the low frequency approximation in order to properly account for the growing shielding effect as the frequency is increased.

5.3 Comparison of RMF and TMF

Finally, we look at the difference in forces for the two types of magnetic stirring methods. The selection of the particular alternating magnetic field depends on the type of stirring desired. The RMF creates a strong stirring force in the azimuthal direction while the TMF produces large forces in the axial direction. The analytic solutions certainly suggest this with forces only existing in the intended directions. For $Ta_m = Ta_{\mathrm{TMF}} = 1 \times 10^5$, Table 5.1 shows the maximum analytic and laboratory forces as a function of frequency for both the RMF and TMF. The analytic values are $\langle F_{\theta,\mathrm{analytic}} \rangle_{\bar{\theta},max} = 7.40 \times 10^4$ for the RMF and $\langle F_{z,\mathrm{analytic}} \rangle_{\bar{\theta},max} = 5.00 \times 10^4$ for the TMF and the other components are zero. However, the laboratory forces indicate that nonzero forces do exist in other directions and that they are significant. At a frequency as low as $f^*_{\mathrm{ext}} = 100$ Hz, the RMF has nonzero radial and axial forces, but they are nearly two orders of magnitude less than the azimuthal force. The TMF at this same frequency has a radial component that is only an order of magnitude less than the axial component, while the azimuthal component is two orders of magnitude smaller than the axial component. By a frequency of $f^*_{\mathrm{ext}} = 3000$, the radial and axial forces in the laboratory RMF are on the same order of magnitude as the azimuthal force. Similarly, the radial force in the laboratory TMF case is on the same order of magnitude as the axial force, but the azimuthal force continues to be two orders of magnitude smaller.

Table 5.1 : Comparison of forces at $Ta_m = Ta_{\mathrm{TMF}} = 10^5$.

	RMF			
f^*_{ext} (Hz)	$\langle F_{r,\mathrm{lab}}\rangle_{\overline{\theta},max}$	$\langle F_{\theta,\mathrm{lab}}\rangle_{\overline{\theta},max}$	$\langle F_{z,\mathrm{lab}}\rangle_{\overline{\theta},max}$	$\langle F_{\theta,\mathrm{analytic}}\rangle_{\overline{\theta},max}$
100	1.33×10^3	7.35×10^4	1.77×10^3	7.40×10^4
500	6.45×10^3	7.32×10^4	8.69×10^3	7.40×10^4
1000	1.27×10^4	7.23×10^4	1.71×10^4	7.40×10^4
2000	2.39×10^4	6.83×10^4	3.22×10^4	7.40×10^4
3000	3.16×10^4	6.06×10^4	4.25×10^4	7.40×10^4
4000	3.60×10^4	5.22×10^4	4.82×10^4	7.40×10^4
	TMF			
	$\langle F_{r,\mathrm{lab}}\rangle_{\overline{\theta},max}$	$\langle F_{\theta,\mathrm{lab}}\rangle_{\overline{\theta},max}$	$\langle F_{z,\mathrm{lab}}\rangle_{\overline{\theta},max}$	$\langle F_{z,\mathrm{analytic}}\rangle_{\overline{\theta},max}$
100	2.06×10^3	9.83×10^1	5.11×10^4	5.00×10^4
500	3.81×10^3	9.34×10^1	5.21×10^4	5.00×10^4
1000	1.35×10^4	1.51×10^2	5.62×10^4	5.00×10^4
2000	2.59×10^4	2.35×10^2	6.05×10^4	5.00×10^4
3000	4.75×10^4	4.14×10^2	6.62×10^4	5.00×10^4
4000	6.35×10^4	5.55×10^2	6.87×10^4	5.00×10^4

Appendix A

Grid Studies

A.1 Opera

Here, we cover a quick grid study for the simulations done in Opera. The TMF case is used because of its quick runtimes and because it is used in the fluid grid study as well due to its strong meridional flow. Table A.1 shows the values of the axial force and the radial force, the two dominant forces in the TMF simulations, as the number of nodes is increased. The distribution of nodes was approximately the same in each case because the nodal density was increased proportionally. Figure A.1 shows these same values in a plot so that the convergence is more obvious.

Nodes	$\langle F_{\mathrm{EM,lab},r} \rangle \times 10^{-4}$	$\langle F_{\mathrm{EM,lab},z} \rangle \times 10^{-4}$
28,128	6.050	6.743
66,753	6.345	6.866
93,674	6.356	6.857
123,695	6.352	6.860
168,951	6.351	6.851

Table A.1 : Values of the maximum radial velocity, maximum axial velocity, and the total energy as the interpolation order is increased.

The results suggests that our choice of 123,695 nodes is sufficient for obtaining an

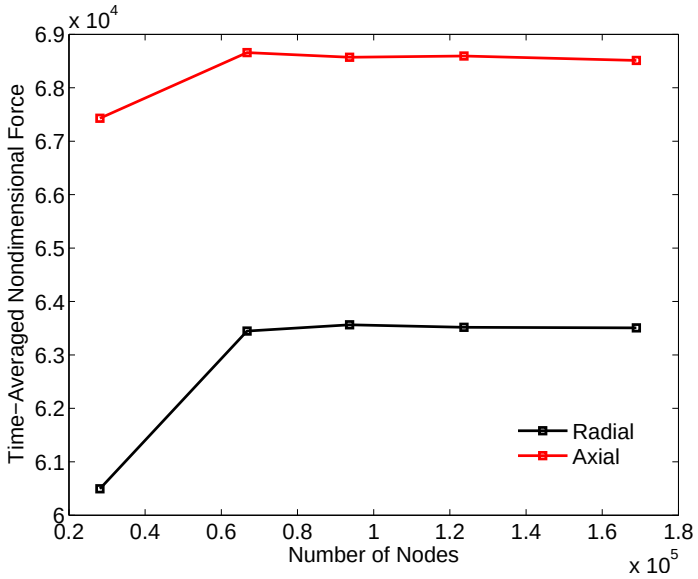

Figure A.1 : Convergence of the radial and axial velocities as the number of nodes in the solution domain is increased.

accurate solution.

A.2 Semtex

A.2.1 Interpolation Order P

We briefly cover convergence studies on the mesh spacing and the time steps used in all simulations. The convergence studies need only be done for an axisymmetric base flow as the third direction, the azimuthal direction, is handled via Fourier modes. The number of Fourier modes to use is determined by linear stability theory (though tests were performed to ensure higher order modes were negligible). For the axisymmetric study, the TMF-driven flow is considered as it is a meridional flow. The magnetic TMF Taylor number is set at $Ta_{\mathrm{TMF}} = 1.75 \times 10^5$, which is higher than any TMF Taylor number used in this work. The grid used for all simulations and this convergent study is shown in Figure A.2.

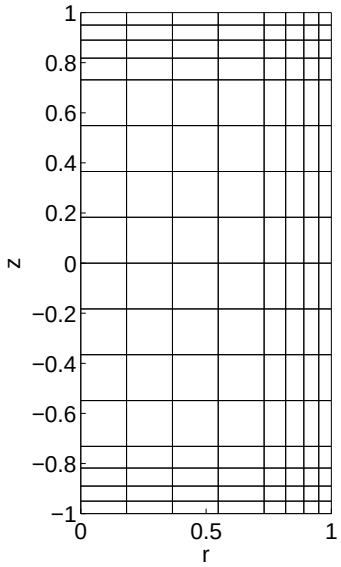

Figure A.2 : The mesh in the r-z plane for the convergence study. It has 8×16 elements, which remain constant through the study.

The elements do not change in this study. Only the order of interpolation, and hence the number of nodes, are increased. All simulations were run by ramping the force from zero between $t = 0$ and $t = 1$, and then run for an additional nondimensional time unit to a steady state. The time step used in each case was $\Delta t = 10^{-5}$. The flow field was then sampled at 20×20 uniformly spaced points within each element and the maximum of those values is reported. Table A.2 shows how the radial and axial components of the velocity as well as the energy vary with polynomial order for $P = 4$ to $P = 10$.

Clearly, the velocities have converged at $P = 7$ to the third decimal place and the energy has also converged so our choice to use $P = 8$ is justified.

P	$v_{r,max}$	$v_{z,max}$	Energy
4	333.653	389.528	15843.6
5	333.707	389.510	15849.3
6	333.702	389.503	15849.0
7	333.703	389.502	15849.0
8	333.703	389.502	15849.0
9	333.703	389.502	15849.0
10	333.703	389.502	15849.0

Table A.2 : Values of the maximum radial velocity, maximum axial velocity, and the total energy as the interpolation order is increased.

A.2.2 Time Step Δt

With our choice of $P = 8$, we then moved on to choosing a suitable time step. The time steps varied from 0.9×10^{-5} to 2×10^{-5} and were run from $t = 0$ to $t = 1.8$. The force is ramped between $t = 0$ and $t = 1$. Velocity values were pulled from $t = 0.9$ while the force was still being ramped so that the simulation was still in its transient stage. All runs reached the same steady state except for the $\Delta t = 2.0 \times 10^{-5}$ case, which eventually becomes unstable.

Table A.2.2 shows the maximum velocities and energies as the time step is decreased. As was done in the last section, the flow field was sampled at 20×20 uniform points on each element and maximum values were taken from that sample. The velocity components appear to be converged to the second decimal place and nearly the third. The energy also appears to be nearly converged to the first decimal place. With these results, we feel confident that our choice of $\Delta t = 1.0 \times 10^{-5}$ for all simulations

is giving accurate temporal results.

$\Delta t \times 10^5$	$v_{r,max}$	$v_{z,max}$	Energy
2.000	309.225	357.669	13529.2
1.500	309.224	357.667	13529.1
1.250	309.224	357.667	13529.1
1.125	309.224	357.666	13529.1
1.000	309.223	357.666	13529.0
0.900	309.223	357.666	13529.0

Table A.3 : Values of the maximum radial velocity, maximum axial velocity, and the total energy as the time step is decreased.

Bibliography

[1] B. C. Houchens, P. Becla, S. E. Tritchler, A. J. Goza, and D. F. Bliss, "Crystal growth of bulk ternary semiconductors," *American Crystal Growth Conference*, 2009.

[2] B. C. Houchens, P. Becla, S. E. Tritchler, A. J. Goza, and D. F. Bliss, "Crystal growth of bulk ternary semiconductors: Comparison of gainsb growth by horizontal bridgman and horizontal traveling heater method," *Journal of Crystal Growth*, vol. 312, no. 8, pp. 1090–1094, 2010.

[3] S. Davis, *Handbook of Crystal Growth*. Elsevier Science Publisher, New York, NY, 1993.

[4] R. Triboulet, "The travelling heater method (thm) for $hg_{1-x}cd_xte$ and related materials," *Progress in crystal growth and characterization of materials*, vol. 28, no. 1, pp. 85–144, 1994.

[5] Y. Huang, *Magnetic Control in Crystal Growth from a Melt*. PhD thesis, Rice University, 2012.

[6] Y. Huang, K. E. Davis, and B. C. Houchens, "Flow control using alternating magnetic fields during crystal growth from a melt," in *Proceedings of the ASME 2012 International Mechanical Engineering Congress & Exposition*, 2012. IMECE2012-88373.

[7] H. Kürth *Stahl und Eisen*, vol. 39, no. 19, p. 512, 1917.

[8] P. Dold and K. Benz, "Rotating magnetic fields: fluid flow and crystal growth applications," *Progress in Crystal Growth and Characterization of Materials*, vol. 38, no. 1, pp. 39–58, 1999.

[9] Y. Huang and B. Houchens, "Magnetic stabilization, transition and energy analysis in the marangoni driven full-zone at low prandtl numbers," *The European Physical Journal Special Topics*, vol. 192, no. 1, pp. 47–61, 2011.

[10] K. E. Davis, Y. Huang, and B. C. Houchens, "Three-dimensional simulations of instabilities in a marangoni-driven, low prandtl number liquid bridge with magnetic stabilization to verify linear stability theory," *The European Physical Journal Special Topics*, vol. 219, no. 1, pp. 13–23, 2013.

[11] M. Volz, J. Walker, M. Schweizer, S. Cobb, and F. Szofran, "Bridgman growth of germanium crystals in a rotating magnetic field," *Journal of Crystal Growth*, vol. 282, no. 3, pp. 305–312, 2005.

[12] A. Senchenkov, I. Barmin, A. Tomson, and V. Krapukhin, "Seedless thm growth of $Cd_xHg_{1-x}Te(x \approx 0.2)$ single crystals within rotating magnetic field," *Journal of Crystal Growth*, vol. 197, no. 3, pp. 552–556, 1999.

[13] C. K. Ghaddar, C. K. Lee, S. Motakef, and D. C. Gillies, "Numerical simulation of thm growth of cdte in presence of rotating magnetic fields (rmf)," *Journal of Crystal Growth*, vol. 205, no. 1, pp. 97–111, 1999.

[14] J. Walker, L. M. Witkowski, and B. Houchens, "Effects of a rotating magnetic field on the thermocapillary instability in the floating zone process," *Journal of Crystal Growth*, vol. 252, no. 1, pp. 413–423, 2003.

[15] P. Dold, A. Cröll, M. Lichtensteiger, T. Kaiser, and K. Benz, "Floating zone growth of silicon in magnetic fields: Iv. rotating magnetic fields," *Journal of Crystal Growth*, vol. 231, no. 1-2, pp. 95–106, 2001.

[16] A. Richardson, "On the stability of a magnetically driven rotating fluid flow," *J. Fluid Mech*, vol. 63, no. Part 3, pp. 593–605, 1974.

[17] Y. M. Gelfgat, L. Gorbunov, and V. Kolevzon, "Liquid metal flow in a finite-length cylinder with a rotating magnetic field," *Experiments in fluids*, vol. 15, no. 6, pp. 411–416, 1993.

[18] P. Marty, W. L. Martin, P. Trombetta, T. Tomasino, and J. Garandet, "On the stability of rotating mhd flows," in *Transfer Phenomena in Magnetohydrodynamic and Electroconducting Flows*, pp. 327–343, Springer, 1999.

[19] T. Kaiser and K. Benz, "Taylor vortex instabilities induced by a rotating magnetic field: A numerical approach," *Physics of fluids*, vol. 10, p. 1104, 1998.

[20] I. Grants and G. Gerbeth, "Stability of axially symmetric flow driven by a rotating magnetic field in a cylindrical cavity," *Journal of Fluid Mechanics*, vol. 431, pp. 407–426, 2001.

[21] I. Grants and G. Gerbeth, "Linear three-dimensional instability of a magnetically driven rotating flow," *Journal of Fluid Mechanics*, vol. 463, pp. 229–239, 2002.

[22] K. Koal, J. Stiller, and R. Grundmann, "Linear and nonlinear instability in a cylindrical enclosure caused by a rotating magnetic field," *Physics of Fluids*, vol. 19, p. 088107, 2007.

[23] H. Blackburn and S. Sherwin, "Formulation of a Galerkin spectral element-Fourier method for three-dimensional incompressible flows in cylindrical geometries," *Journal of Computational Physics*, vol. 197, no. 2, pp. 759–778, 2004.

[24] K. Mazuruk, "Control of melt convection using traveling magnetic fields," *Advances in Space Research*, vol. 29, no. 4, pp. 541–548, 2002.

[25] N. Dropka, C. Frank-Rotsch, W. Miller, and P. Rudolph, "Influence of travelling magnetic fields on s–l interface shapes of materials with different electrical conductivities," *Journal of Crystal Growth*, vol. 338, no. 1, pp. 208–213, 2012.

[26] T. P. Lyubimova, A. Croell, P. Dold, O. A. Khlybov, and I. S. Fayzrakhmanova, "Time-dependent magnetic field influence on gaas crystal growth by vertical bridgman method," *Journal of crystal growth*, vol. 266, no. 1, pp. 404–410, 2004.

[27] I. Grants and G. Gerbeth, "Stability of melt flow due to a traveling magnetic field in a closed ampoule," *Journal of Crystal Growth*, vol. 269, no. 2, pp. 630–638, 2004.

[28] R. Lantzsch, V. Galindo, I. Grants, C. Zhang, O. Pätzold, G. Gerbeth, and M. Stelter, "Experimental and numerical results on the fluid flow driven by a traveling magnetic field," *Journal of Crystal Growth*, vol. 305, no. 1, pp. 249–256, 2007.

[29] V. Galindo, I. Grants, R. Lantzsch, O. Pätzold, and G. Gerbeth, "Numerical and experimental modeling of the melt flow in a traveling magnetic field for vertical gradient freeze crystal growth," *Journal of Crystal Growth*, vol. 303, no. 1, pp. 258–261, 2007.

[30] A. Y. Gelfgat and E. Kit, "Skin-effect influence on three-dimensional instability of a traveling magnetic field driven flow in a cylindrical container," in *The 15th RIGA and 6th PAMIR Conference on Fundamental And Applied MHD*, pp. 133–136, 2005.

[31] A. Y. Gelfgat, "On three-dimensional instability of a traveling magnetic field driven flow in a cylindrical container," *Journal of Crystal Growth*, vol. 279, no. 3, pp. 276–288, 2005.

[32] A. Cramer, J. Pal, and G. Gerbeth, "Experimental investigation of a flow driven by a combination of a rotating and a traveling magnetic field," *Physics of Fluids*, vol. 19, p. 118109, 2007.

[33] J. Stiller and K. Koal, "A numerical study of the turbulent flow driven by rotating and travelling magnetic fields in a cylindrical cavity," *Journal of Turbulence*, no. 10, 2009.

[34] J. Stiller, K. Koal, W. Nagel, J. Pal, and A. Cramer, "Liquid metal flows driven by rotating and traveling magnetic fields," *The European Physical Journal Special Topics*, vol. 220, no. 1, pp. 111–122, 2013.

[35] P. A. Davidson, *An Introduction to Magnetohydrodynamics*. Cambridge University Press, 2001.

[36] P. Davidson, "Swirling flow in an axisymmetric cavity of arbitrary profile, driven by a rotating magnetic field," *Journal of Fluid Mechanics*, vol. 245, pp. 669–669, 1992.

[37] Vector Fields Limited, "Vector Fields Opera 3D Reference Manual." http://www.vectorfields.com, Aug. 2007.

[38] V. M. Glazov, S. N. Chizhevskaya, N. G. Natal'ya, and A. Tybulewicz, *Liquid semiconductors*, vol. 2. Plenum Press New York, 1969.

[39] MATLAB, *version 8.0.0 (R2012b)*. Natick, Massachusetts: The MathWorks Inc., 2012.

[40] K. Mazuruk, N. Ramachandran, M. P. Volz, and D. C. Gillies, "Study of frequency effects of a rotating magnetic field on fluid flow in vertical cylinders," in *Proceedings of SPIE*, vol. 3123 of *1*, pp. 262–271, 1997.

[41] L. M. Witkowski, J. Walker, and P. Marty, "Nonaxisymmetric flow in a finite-length cylinder with a rotating magnetic field," *Physics of Fluids*, vol. 11, p. 1821, 1999.

[42] A. Patera, "A spectral element method for fluid dynamics: laminar flow in a channel expansion," *Journal of Computational Physics*, vol. 54, no. 3, pp. 468–488, 1984.

[43] A. Henderson, *The ParaView guide: a parallel visualization application*. Kitware, 2007.

[44] L. Tuckerman, "Practical Bifurcation Techniques and Nonlinear Tourism." http://www.pmmh.espci.fr/ laurette/class/Practical.pdf.

[45] J. Krumins, "Fundamentals of theory and calculation for devices with a traveling magnetic field," *Riga*, 1983.